Florida State University Libraries

2016

Circulation and Stirring by Ocean Turbulence

Dhruv Balwada

FLORIDA STATE UNIVERSITY

COLLEGE OF ARTS AND SCIENCES

CIRCULATION AND STIRRING BY OCEAN TURBULENCE

By

DHRUV BALWADA

A Dissertation submitted to the
Geophysical Fluid Dynamics Institute
in partial fulfillment of the
requirements for the degree of
Doctor of Philosophy

2016

Dhruv Balwada defended this dissertation on November 10, 2016.
The members of the supervisory committee were:

Kevin Speer

Professor Directing Dissertation

William Landing

University Representative

William Dewar

Committee Member

Phillip Sura

Committee Member

The Graduate School has verified and approved the above-named committee members, and certifies
that the dissertation has been approved in accordance with university requirements.

To my parents, Suman and Sushil Balwada.

ACKNOWLEDGMENTS

TABLE OF CONTENTS

LIST OF FIGURES

viii

ABSTRACT

Ocean turbulence is responsible for stirring and spreading ocean tracers, and contributes to the mean circulation as eddy bolus fluxes. The influence of the eddies on the mean circulation becomes particularly important in regions where mean geostrophic flows are weak, such as the meridional flow across the Antarctic Circumpolar Current. However, high resolution observations of eddies and their influence on the circulation are generally lacking, particularly in the deep ocean that cannot be observed via satellites. The Diapycnal and Isopycnal Mixing Experiment in the Southern Ocean (DIMES) was designed to observe the transport and stirring associated with the eddies in the Southern Ocean, using RAFOS floats and a passive tracer. In the first half of the thesis, the imprint of the eddies on the large scale circulation (> 100 km) is assumed to be diffusive, and the corresponding eddy diffusivities are quantified using the long term behavior of the RAFOS floats. The eddy diffusivities are found to be suppressed in the presence of mean flows. These eddy diffusivity estimates from DIMES, along with estimates from a couple of other diffusivity studies, are then used to quantify the eddy bolus fluxes in the Southern Ocean, which were found to vary in response to the bottom bathymetry.

The second part of this work, addresses the flow at the length scales of the submesoscale and mesoscale (< 100 km). Here, in addition to the DIMES RAFOS floats, we also used surface drifter observations from an experiment, Grand Lagrangian Deployment (GLAD), conducted in the Gulf of Mexico. The goal was to observe the kinematic stirring properties at these smaller scales, and also to characterize the dynamics of the turbulence that is active by investigating the energy spectrum. At the surface ocean in the Gulf of Mexico, we characterized the scale dependent energy distribution over 5 orders of length scales (10 m - 1000 km) using second order velocity structure functions. Divergent motions were found to be dominant, over non-divergent motions, at length scales smaller than 5km, where the Rossby number was greater than one and the third order velocity structure functions indicated the presence of a forward energy cascade. These methods were also used to explain subsurface turbulence in the Southern Ocean with DIMES RAFOS floats. The RAFOS floats showed that divergent flows are also present in the deep ocean at length scales smaller than 30 km, and become comparable in magnitude to the non-divergent flows near 5 km. The observed dispersion of the floats was used to address the question - is the mixing at small scales due mainly

to large scale shear (non-local) or small scale eddies (local)? The associated stirring was found to be local at depth.

CHAPTER 1

INTRODUCTION

The is a dissertation in physical oceanography, which is a subject that falls under the broad purview of geophysical fluid dynamics (GFD). One of the most basic objectives of physical oceanography is to understand the patterns and dynamics of the circulation that is observed in the ocean. This circulation varies over a range of times scales, the waves at the beach and tides vary on the order of minutes to hours, the seasonal deepening and restratification of mixed layers, meanders of the Gulf Stream and the El-Nino in the Pacific Ocean vary on the order of months to years, and the meridional overturning circulation (MOC) has associated time scales of decades to centuries. These processes more often than not influence each other in complex chaotic ways, and understanding these interactions is the challenge.

The work presented here is a small effort at undertaking part of this challenge from primarily an observational perspective. The central focus is to observe, characterize and quantify the variability that dominates at the length scales of O (10-100 km), often referred to as the mesoscale in the ocean and defined as a range of scales where the scales of motion are order deformation radius, L_d, $(L_d = \sqrt{g'H}/f$, where g' is the reduced gravity in a stratified fluid, H is a characteristic depth scale and and f is the Coriolis frequency) and the Rossby number, Ro, $(Ro = U/fL$, U is a characteristic velocity scales and L is a characteristic length scale) is much smaller than one, and to derive the implications this variability has on the MOC. The hope is that this work will help in guiding and constraining parameterizations in the global ocean circulation models that simulate the long term ocean climate, but are unable to resolve the mesoscales due to computational limitations.

1.1 Meridional Overturning Circulation

The MOC is a planetary scale flow, ranging from the north pole to the coast of Antarctica and from the surface to the deepest trenches, that is responsible for renewing the deepest ocean with new water, which has recently been in contact with the atmosphere at the surface. In doing so the MOC is able to sequester, or release, large amounts of carbon and heat from the atmosphere, and in
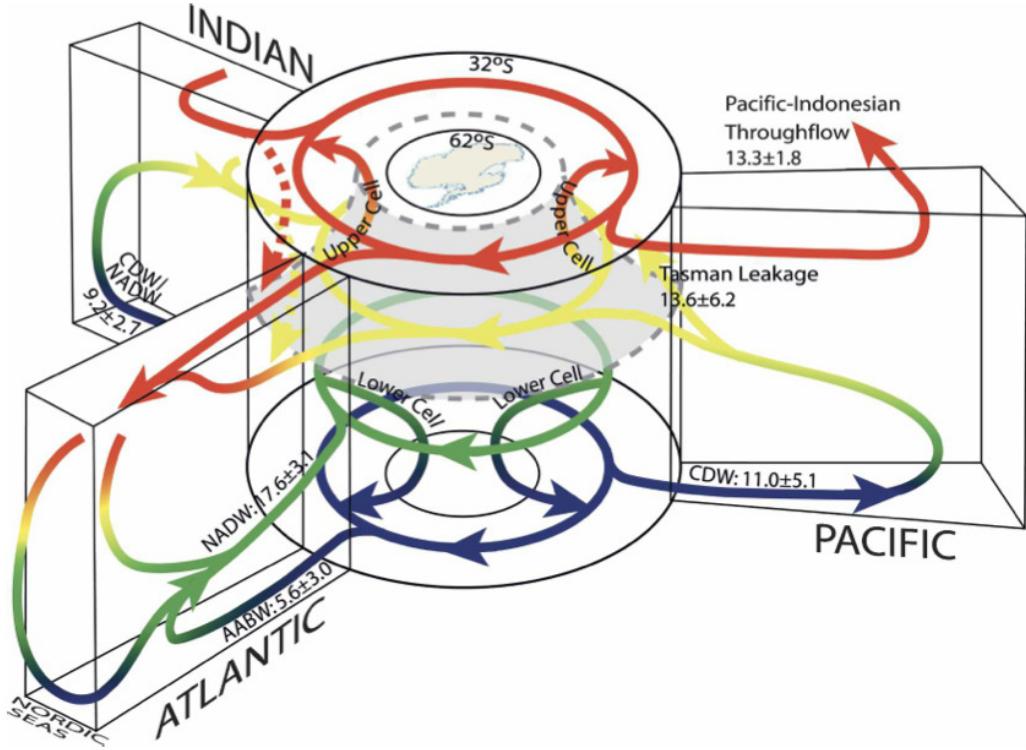
Figure 1.1: Schematic of global overturning circulation taken from Lumpkin and Speer (2007). Color indicates approximate density ranges. Red: upper, $\gamma \sim 27.0$; yellow: intermediate, $\gamma \sim 27.0\text{-}27.6$; green: deep, $\gamma \sim 27.6\text{-}28.15$; blue: bottom, $\gamma > 28.15$. Gray surface with dashed edges is $\gamma = 27.6$ at 32S, separating upper and lower cell transformation in the Southern Ocean.

the process effect the rate of global climate change. It is estimated that over the large century the ocean has been responsible for storing about a quarter of the excess carbon, and about 90% of the excess heat, that has been introduced in the atmosphere due to anthropogenic causes (IPCC AR5 report). Thus, it goes without saying that understanding the dynamics of the MOC are extremely important for understanding global climate.

The traditional schematic of the MOC is one of a filling box model, a convenient conceptual starting point to understand the dynamics of the MOC. Sinking of water, due to deep convection near the poles and dense water formation at the high latitude continental margins, supplies dense water to the deepest parts of the ocean. To maintain the steady interior stratification, which is observed to be the case in the ocean at least over the last century, the deep dense water needs to be transformed back to lighter density water. In the filling box model this transformation must take

place in the interior, and would require turbulent diapycnal mixing rate of $10^{-4}m^2/s$ to maintain the observed stratification by a balance between upwelling and vertical diffusion (Munk (1966)). However, observations of the interior mixing rate indicate values that are smaller by an order of magnitude ($10^{-5}m^2/s$), and put the validity of the filling box model into question (Ledwell et al. (1993)). This implies that processes that are ignored in this conceptual model must be important in the dynamics of the MOC. Presumably these processes are closely linked to the ocean boundaries, where density transformation can happen very efficiently; turbulent diapycnal mixing rates are usually enhanced near the bottom boundaries (Ledwell et al. (2000)), and air-sea-ice interaction and enhanced wind driven mixing at the surface are very efficient at transforming densities (Speer et al. (2000)). For these boundary processes to significantly affect the density transformation, the appropriate density classes need to be brought in contact with the boundaries. Over the years a more consistent picture of the MOC has emerged (see review in Marshall and Speer (2012)), and it has been established that the Southern Ocean is central in closing the density budget of the MOC (Figure 1.1 highlights the importance of the Southern Ocean, and also illustrates the 3 dimensionality of the MOC).

The Southern Ocean plays an important role in ventilating the deep ocean, bringing deep ocean water in contact with the atmosphere, and allowing surface buoyancy fluxes to directly transform density. As the Antarctic Circumpolar Current (ACC) homogenizes properties zonally, 2D zonally averaged models are useful in describing the relevant dynamical processes (Figure 1.2, Nikurashin and Vallis (2012)). In the latitude bands where the ACC flows, the isopycnals rise to the surface to the south in accordance with thermal wind balance (zone 1 in Figure 1.2). These sloping isopycnals provide an adiabatic pathway for deep water masses to reach the surface. The flow of water, along isopycnals, towards the surface requires the appropriate Ekman suction by the wind, and a corresponding buoyancy flux to transform the dense water and maintain the equilibrium horizontal stratification at the surface, which implies a buoyancy gain (loss) on the north (south) of the ACC. Simultaneously sufficient volume of water needs to be formed, by buoyancy loss at the high latitudes or interior diapycnal transformation, and transported from the interior of the basins towards the ACC (from zone 2 and 3 towards zone1 in Figure 1.2). This transport in the interior of the basins is achieved, at least in part, by the deep western boundary currents and gyres. Also, in the Southern Ocean, this interior supply of water needs to cross the Drake Passage latitude band
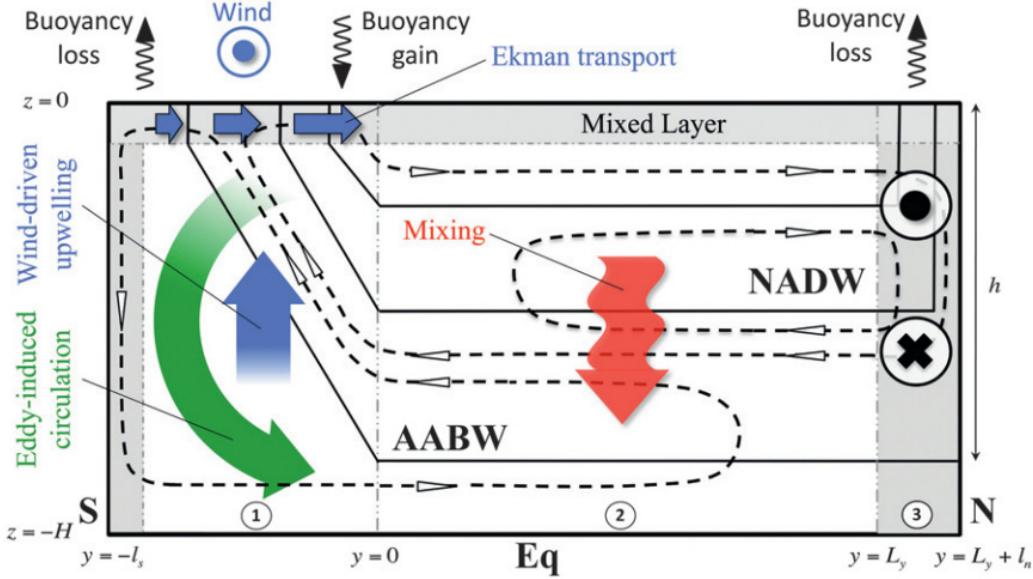
Figure 1.2: Schematic of the MOC taken from Nikurashin and Vallis (2012). Solid black lines are the isopycnals, thicker dashed black lines with arrows are the overturning streamlines of the residual circulation, dashed vertical lines are the boundaries between adjacent regions, shaded gray areas are the convective regions at high latitudes and the surface mixed layer, and the red arrow represents downward diffusive flux due to mixing uniform throughout the ocean. Labels 1, 2, and 3 (in circles) correspond to the circumpolar channel, ocean basin, and isopycnal outcrop regions considered in the theory

to reach the surface. However, due to the presence of an open channel, above the sill depth of the shallowest topography in the zonally unblocked latitude bands of the Drake Passage, this transport cannot cross in mean geostrophic boundary currents and has to rely on the eddy driven fluxes. An alternative way of thinking about the role of eddies is that they counteract the steepening of isopycnals due to the wind driven circulation, by slumping isopycnals and extracting potential energy, and help in maintaining the equilibrium slope of the isopycnals. Thus, understanding the controlling mechanisms and quantifying the strength of the eddy driven circulation is essential. This is commonly done in the framework of eddy diffusivities, discussed next.

1.2 Eddy Diffusivity and Eddy Bolus Velocity

A convenient starting point, when addressing the effects of eddies on a mean field, is the mean tracer equation, where Reynold's averaging ($c = C + c'$, c is the concentration field that is

decomposed into a mean, C, and a variability, c') has been applied,

$$\frac{\partial C}{\partial t} + \bar{U}.\nabla C = -\nabla.\overline{u'c'} + \kappa\nabla^2 C. \tag{1.1}$$

Taylor (1921) noted that the correlation of tracer and velocity fluctuation could be simplified as $\overline{u'c'} \sim -\overline{u'x'}\nabla C$, using a Taylor expansion and retaining the first term. The velocity-displacement correlation can be written as $\overline{u'x'} = v^2 \int_0^t R(\tau)d\tau$, where $R(\tau)$ is the normalized velocity auto-correlation and v^2 is the velocity variance, provided that the velocity fluctuations are stationary. This change to an integral form essentially shows the relationship of an Eulerian quantity at a fixed location to the Lagrangian history of the particles that cross through the location. It can be assumed that in a turbulent flow the velocity auto-correlation asymptotes to zero, and its integral to a constant, at long time. This constant is often referred to as the Lagrangian integral time scale (T_L), and the eddy diffusivity is defined as $K_e = v^2 T_L$. This long term decorrelation happens when the fluid parcels have moved far enough from their initial flow feature (or the flow feature has moved away from the particle), and lost memory of the flow that was advecting them. The behavior of the diffusivity at the intermediate time scale, when the velocity autocorrelation is non-zero and the particle velocities are correlated is discussed in the next section.

In principle the Lagrangian integral time scale and the corresponding eddy diffusivity can be measured directly in the ocean. However, developing a dynamical theory that predicts T_L and relates it to background variables is useful. Some recent work (Ferrari and Nikurashin (2010); Srinivasan and Young (2014)) has focussed specifically on the effect of zonal flows, and associated large scale PV gradients, on the eddy diffusivity. It is shown that the presence of a mean flow, such as the ACC, can suppress the eddy diffusivity that would otherwise be expected if the eddies were present without the mean flow.

The large scale influence of eddies is to mix tracers, such as oxygen, carbon or potential vorticity (PV), as illuminated by the above discussion. When PV is mixed downgradient, it has an associated bolus velocity that is directed up the PV gradient (Vallis (2006)). This eddy driven bolus velocity is an essential component of transport that contributes to the MOC in the Southern Ocean.

1.3 Non-Diffusive Dispersion and Ocean Turbulence

A diffusive process is characterized by uncorrelated velocities, either the velocity autocorrelation of an individual particle or the velocity correlation of a pair of particles approaches zero. This is

usually the case when the separation between a pair of particles is greater than the dominant eddy length scales. However, at separations smaller than the size of the eddies the particle trajectories execute correlated motions, the spreading is usually super-diffusive, and the dispersion grows faster than a linear function of time. Understanding and quantifying the stirring at this correlated range of motions is important for being able to describe the spreading of tracers at length scales of the mesoscale and smaller, and also for developing improved parameterizations of sub-grid processes in eddy-permitting ocean simulations.

The analysis usually starts, as one would expect, by measuring the relative separation, $\mathbf{r}(t)$, of a pair of particles,

$$\mathbf{r}(t) = \mathbf{r}(0) + \int_0^t \delta\mathbf{v}(t')dt'. \tag{1.2}$$

Here $\delta\mathbf{v} = \mathbf{v_1} - \mathbf{v_2}$ is the relative separation velocity, where subscripts indicate the individual members of the pair. The relative dispersion is an ensemble average of the square of the relative separations of individual particle pairs ($\overline{r^2}(t)$, where the bar signifies an ensemble average, and $r = |\mathbf{r}|$), and the rate of change of relative dispersion, $\frac{1}{2}\frac{d}{dt}\overline{r^2}(t)$, is the relative diffusivity. The relative diffusivity (K_2) can be expressed as

$$
\begin{aligned}
K_2(t) &= \frac{1}{2}\frac{d}{dt}\overline{r^2}(t) \\
&= \overline{\mathbf{r}\delta\mathbf{v}} \\
&= 2\nu^2 \int_0^t R(t')dt' - 2\int_0^t \overline{\mathbf{v_1}\mathbf{v_2}}dt' + \overline{\mathbf{r}(0)\delta\mathbf{v}},
\end{aligned}
\tag{1.3}
$$

where ν^2 is the individual particle's velocity variance, assumed to be stationary in time, and $R(t')$ is the velocity autocorrelation of the individual particles, same as previous section. The last term on the RHS ($\overline{\mathbf{r}(0)\delta\mathbf{v}}$) is negligible for a homogeneous flow field with randomly distributed initial particle pairs. Thus the relative diffusivity is different from twice the absolute diffusivity only due to the pair velocity correlation ($\overline{\mathbf{v_1}\mathbf{v_2}}$).

In the above expressions the dependence of the variables on $\mathbf{r}$ has been suppressed, the relative diffusivity, velocity correlation are functions of both time and relative separation, as the averages are taken irrespective of the separation. However, the functional dependence of the diffusivity and velocity correlation on separation is important, but there is no simple way to explore this

dependence directly. Velocity structure functions are a metric that describe the nature of the flow as a function of separation, rather than time. Velocity structure functions at order p are defined as $Sp(r) = \overline{\delta \mathbf{v}^p}(r))$, where $\delta \mathbf{v}(r)$ is the velocity difference between two points separated by distance r. Different scaling laws exist for $Sp(r)$ in different turbulent cascades, as will be discussed later in the subsequent chapters. Here we only introduce the second order velocity structure function (S2). S2 is related to the velocity correlation as $S2 = \overline{\delta \mathbf{v}^2} = 2\nu^2 - 2v_1 v_2$, which proposes that a connection between S2 and relative dispersion might exist. S2 is also related to the energy spectrum as

$$S2(r) = 2 \int_o^\infty E(k)(1 - J_o(kr))dk, \tag{1.4}$$

where $E(k)$ is the energy spectrum, J_o is the zeroth order Bessel function, and k is the wave number.

Traditional theoretical models of fluid turbulence provide exact scaling relationships for the wavenumber energy spectrum in the respective inertial ranges. For example the interior QG turbulence (Charney (1971)), which might be most applicable to mesoscale turbulence, has two inertial ranges. The k^{-3} enstrophy cascade, and $k^{-5/3}$ inverse energy cascade. Observational estimates of the energy spectrum can corroborate a particular set of dynamics at particular length scales. This will allow the appropriate choice of a theoretical model when modeling and describing the flow, and also has more broader implications for understanding the ocean's energy budgets (Ferrari and Wunsch (2008, 2010)).

It can also be argued based on scaling principles, and has been shown to be true in numerous numerical studies (Babiano et al. (1985); LaCasce (2008)), that the separation dependence of the relative dispersion scales according to the behavior of the S2,

$$K_2(r) = \overline{\mathbf{r}\delta \mathbf{v}} \sim r.\sqrt{S2}. \tag{1.5}$$

The above stated connection between the energy spectrum, structure functions and relative diffusivity is a convenient one, which can be used to get important clues about the flow dynamics using observations.

1.4 Overview of the Dissertation

The majority of the work presented here is the result of a RAFOS float experiment that was conducted as part of the Diapycnal and Isopycnal Mixing Experiment in the Southern Ocean (DIMES). DIMES was a process study designed with the goal to provide observational estimates of both the diapycnal and isopycnal diffusivities in the southeast Pacific Ocean and Scotia Sea sectors of the ACC. RAFOS floats, which are Lagrangian instruments designed to measure sub-surface flows, were deployed at multiple depth levels during DIMES to quantify the lateral (isopycnal) eddy stirring, and to understand its vertical structure and relationship to the mean flow.

In Chapter 2, results pertaining to the mean flow and eddy stirring, as observed by the DIMES RAFOS floats, are presented. The key goal was to estimate the eddy diffusivities in the DIMES region. In Chapter 3 the over arching goal of DIMES, quantifying the eddy driven volume flux across the ACC, is addressed. This is done by using a variety of eddy diffusivity estimates, from DIMES and otherwise, in conjunction with the large scale PV structure calculated from hydrographic measurements by Argo floats.

In Chapter 4 the RAFOS float data from the DIMES experiment is used to investigate the turbulent dynamics of the deep ocean using relative dispersion and structure functions. Chapter 5 focuses specifically on structure functions using data from a drifter experiment (Grand Lagrangian Deployment, GLAD) to learn about the surface ocean dynamics in the Gulf of Mexico. The GLAD drifters allows us to apply our methods over a large range of length scales (10m - 1000km), and helped provide an interesting contrast to our DIMES results pertaining to the deep ocean.

CHAPTER 2

CIRCULATION AND STIRRING IN THE SOUTHEAST PACIFIC OCEAN AND THE SCOTIA SEA SECTORS OF THE ANTARCTIC CIRCUMPOLAR CURRENT

The large-scale mid-depth circulation and eddy diffusivities in the Southeast Pacific Ocean and Scotia Sea sectors between 110^oW and 45^oW of the Antarctic Circumpolar Current (ACC) are described based on a subsurface quasi-isobaric RAFOS float based Lagrangian dataset. This RAFOS float data was collected during the Diapycnal and Isopycnal Mixing Experiment in the Southern Ocean (DIMES). The mean flow, adjusted to a common 1400m depth, shows the presence of jets in the time-averaged sense with speeds of 6cm/s in the Southeast Pacific Ocean and upwards of 13cm/s in the Scotia Sea. These jets appear to be locked to topography in the Scotia Sea but, aside from negotiating a seamount chain, are mostly free of local topographic constraints in the Southeast Pacific Ocean. The EKE is higher than the MKE everywhere in the sampled domain by about 50%. The magnitude of the EKE increases drastically (by a factor of 2 or more) as the current crosses over the Hero Fracture Zone and Shackleton Fracture Zone into the Scotia Sea. The meridional isopycnal stirring shows lateral and vertical variations with local eddy diffusivities as high as $2800 \pm 600 m^2/s$ at 700m decreasing to $990 \pm 200 m^2/s$ at 1800m in the Southeast Pacific Ocean. However, the cross-ACC diffusivity in the Southeast Pacific Ocean is significantly lower, with values of $690 \pm 150 m^2/s$ and $1000 \pm 200 m^2/s$ at shallow and deep levels respectively due to the action of jets. The cross-ACC diffusivity in the Scotia Sea is about $1200 \pm 500 m^2/s$

2.1 Introduction

The global ocean circulation is often divided into a nearly horizontal, or approximately isopycnal, component, and an overturning component that is more tightly linked to diabatic processes

in the interior or at the polar extremes. The polar extremes of dense water formation create water masses that spread and fill the global ocean, but this spreading depends on the topography of ocean basins. The cold deep water formed in the northern polar regions of the Atlantic Ocean, North Atlantic Deep Water (NADW), flows south in a deep western boundary current and eventually spreads along the northern flank of the ACC on its course to the Indian and Pacific Ocean basins. A fraction of NADW is injected into the ACC in layers below the Drake Passage sill depth and can be transported across the ACC in deep geostrophic boundary currents to upwell into regions of surface buoyancy loss and be transformed into Antarctic Bottom Water (AABW). This AABW and the other part of the NADW that moves into the Indian and Pacific basins is transformed to Indian Ocean Deep Water (IDW) and Pacific Ocean Deep Water (PDW) via diapycnal processes (e.g. Talley (2013)).

The shallower portions of these deep water masses of the Indian and Pacific Oceans, referred to as Upper Circumpolar Deep Waters (UCDW), form layers in the Drake Passage latitude band that are above the sill depth, sill depth being a somewhat complicated construct primarily due to the Scotia Arc and the Kerguelen Plateau. In these layers, simple theory suggests that there is no mean geostrophic flow across the 500km band of the ACC (Warren (1990)). It is often argued that the dynamics in these layers is like that of the atmosphere, where the action of eddies can produce a mean residual flux that on large scales in the Southern Ocean is towards the south (Thompson (2008)). To quantify the transport of this residual flux, in the absence of accurate deep velocity measurements, one needs to quantify the amplitude of the isopycnal eddy stirring (eddy diffusivity) and the large scale gradient of thickness or potential vorticity (PV). Indirect estimates with box model inversions suggest a southward flux of order 10 Sv in deep layers (Lumpkin and Speer (2007), Sloyan and Rintoul (2001), Garabato et al. (2014)).

One view of the ACC (Meredith et al. (2011)) is that of a large-scale, latitudinally broad mean eastward flow, with a transport of about $140Sv$. However, there are large meridional excursions in the regions where it goes over mid-ocean ridges and approaches continents. On this broad, baroclinically unstable mean flow lies a convoluted structure of jets and eddies (Sokolov and Rintoul (2009)). The merging and splitting can at any instance be acting as a barrier to mixing and at another instance strongly mix fluid parcels (Thompson (2010)). This is in marked contrast to the Gulf Stream, for example, where a single primary jet exists. The ACC jets can be locked to

topography, and nearly stationary, or more freely evolving typically in regions with less topographic control (Sallée et al. (2008a)).

Although the importance of the Antarctic Circumpolar Current (ACC) to the adiabatic closure of the meridional overturning circulation has been inferred for some time, direct measurements of the strength and nature of this process have been lacking (Marshall and Speer (2012)). Here we analyze results from an observational campaign, Diapycnal and Isopycnal Mixing Experiment in the Southern Ocean (DIMES), which was undertaken in 2009-2014 to quantify the magnitude of isopycnal eddy diffusivities and diapycnal mixing. We present results from the deployment of RAFOS floats (subsurface drifters tracked by a moored acoustic network) in the Southeast Pacific Ocean and Scotia Sea sectors of the ACC. We focus here on velocity statistics (section 3) and isopycnal mixing (section 4) derived from the RAFOS float observations.

2.2 Overview of the DIMES RAFOS Float Experiment

RAFOS floats were deployed as part of the DIMES experiment, primarily between the synoptically observed positions of the Sub-Antarctic Front (SAF) and Polar Front (PF) at $105^{o}W$. Additional floats were deployed downstream of this deployment site to supplement the dataset. The total number of floats deployed was 210. However, after failures, 140 float tracks comprising 183 years of float data (66795 float-days) were retrieved. Figure 2.1 shows a summary of the experimental design and regional geography, together with the mean SSH contour lines that envelope the extent of the initial float deployment relative to the ACC and the climatological position of the SAF and PF according to Orsi et al. (1995). These SSH and frontal positions provide a general sense of the large scale ACC flow in the region that was sampled.

The duration of the experiment was from 2009 to 2011 with the highest number of float-days sampled in 2010 (Figure 2.3). The floats were originally ballasted to stay near two isopycnal surfaces of neutral density 27.6 and 27.9 σ. However due to technical failures the behavior was closer to that of isobaric floats. For this reason the analysis in this manuscript treats the floats as quasi-isobaric floats. Some floats showed a slow sinking of about 100m/year, which does not affect any results presented here. The distribution of float days in depth shows a bimodal structure with peaks at 800m and 1400m corresponding to the mean positions of the ballasting isopycnals. As the floats did not maintain their target density, the float-days distribution in temperature is wider showing

only a single peak. A distribution of float days over topographic depth following the float shows a peak at 4500m corresponding to the mean depth of the Southeast Pacific Ocean. This distribution also has a long tail towards shallower depths corresponding to the passage through the Scotia Sea, where topographic variability is greater and topographic features often reach within a few hundred meters of the surface.

The float trajectories clearly show a great deal of complexity, both at shallow and deep depth ranges, created by the meso-scale eddies and presence of vertical shear, the latter apparent from the longer displacements of the shallower floats (Figure 2.2). Even though many floats were deployed north of the historical position of the SAF, all floats proceeded east and exited the Southeast Pacific Ocean; remarkably, none moved northward sufficiently to be trapped and subsequently circulate in the subtropical gyre of the Pacific Ocean. This behavior is in agreement with the circulation found by Faure and Speer (2012), who show the presence of a mean flow toward the ACC in the mid-depth layers between 1000-3000 m. In contrast, on the southern side of the ACC, a number of floats did appear to be continuing to move south, away from the core of the ACC.

The concentration of floats, or density in float-days, is highest near and just downstream of the deployment site at 105^oW; a secondary peak is seen near the downstream deployment at 75^oW (Figure 2.4, top). This float density figure is akin to a coarse resolution map of tracer spreading from a permanent tracer source located at float deployment location (Ollitrault and Colin de Verdière (2002)), but more importantly provides a sense of the statistical accuracy that can be expected for the results presented here. A second representation of the float density is provided (Figure 2.4, bottom), showing the number of floats passing through each longitudinal section is summed in meridional bins and then normalized by the total number of floats that pass through that longitudinal section. This effectively renormalizes the concentration as the float cluster evolves downstream.

A qualitative sense of the ACC flow, the transport pathways and its prominent features during the experiment emerges from the tracks (Figure 2.2) and the geographically binned (Eulerian) displays (Figure 2.4, bottom and those discussed in section 3). One of these is a large meander at $100^oW, 59^oS$, which was experienced by the floats in both the 2009 and 2010 deployments. This meander splits into two jets at 95^oW presumably upon interacting with the San Martin Seamounts. We speculate that one of these jets is associated with the PF and the other with the SAF. The

jets merge as they approach Drake Passage, cross barotropic PV (f/H) contours, move northward and make their way over the northern ends of the Hero Fracture Zone and the Shackleton Fracture Zone through deep troughs, into the Yaghan Basin. Once in the Yaghan Basin, the floats are again divided into two groups following topographic contours of of the continental slope on the northern side and the West Scotia Ridge on the southern side of the Yaghan Basin. They exit the Scotia Sea through the openings in the North Scotia Ridge beyond which tracking becomes problematic as the topography blocks most of the sound source signals.

Along with the float data, sea-surface height (SSH) estimates were also used in this study for an approximate streamfunction and for surface geostrophic velocities. These data were obtained as absolute dynamic topography (ADT) data, an altimeter product produced by Ssalto/Duacs and distributed by AVISO, with support from CNES (http:/www.aviso.altimetry.fr/duacs/).

2.3   Eulerian Mean Flow

2.3.1   Vertical Structure of Flow

In this section first we present a comparison of float velocities to SSH derived velocities and later present vertical profiles of velocities averaged over large basin scales (Southeast Pacific Ocean and Scotia Sea). It is important to note that the comparison of float velocities to SSH velocities should not be expected to be highly accurate due to resolution limitations of the AVISO altimeter. The SSH fields are available in 7 day averaged fields, which are then used to calculate the surface geostrophic velocities from the geostrophic stream function $\psi = g\eta/f$, where g is the gravitational acceleration, f is the Coriollis frequency and η is the SSH. The float velocities, resolved daily, are smoothed using a running mean with averaging window of 7 days for comparison against the SSH derived fields. However, the results of this section were found to not be sensitive to the size of the smoothing window (not shown).

We calculate the ratio of the float speed to the SSH derived speed and the angle (θ) between the two velocities. These are then binned in depth bins for each of the basins (Southeast Pacific Ocean and Scotia Sea) and plotted in Figure 2.5. The modal depth structure is similar to a decaying exponential, which agrees with the expectations based on previous studies describing the equivalent barotropic (EB) nature of the ACC (Killworth (1992), Hughes and Killworth (1995), LaCasce and Isachsen (2010)).

The e-folding scale of the mode of the ratio is approximately 1650m in the Southeast Pacific Ocean and 1300m in the Scotia Sea. Chereskin et al. (2010) suggest an e-folding scale of 1900m Southeast Pacific Ocean. Firing et al. (2011) showed that the e-folding scale varies between 1100 and 1700m in the Drake Passage as calculated from SOSE. However the results from their SADCP measurements, which sampled from the surface to 1000m, were less clear and could not distinguish between the profile being linear or exponential. Lack of a perfect match to previous estimates is a result of both the time variability of the current and also the shoaling of the thermocline to the south leading to spatial variability and time variability of the e-folding scale (Karsten and Marshall (2002)). The probability distribution function (PDF) of angle between surface and float velocities vs depth has a mean of zero and a standard deviation around $50^o - 55^o$ for almost all bins.

The EB nature of the ACC was discussed in a dynamical setting by Hughes and Killworth (1995). They showed that for a linear geostrophic flow in the interior (away from influence of wind stress) the turning of the velocity vector with depth took the form

$$\phi_z = -\frac{N^2 w}{f|u|^2} \tag{2.1}$$

where N^2 is the usual Brunt-Vaisala frequency, w is the vertical velocity, f is the Coriolis force, $|u|$ is the flow speed and ϕ_z is the variation of angle with depth. This formula holds on scales that are large enough for the Rossby number to be small. It shows that for regions of weak vertical flow (slowly varying topography), weak stratification and strong horizontal flows the turning with depth will be small. We reiterate that the ACC also has a weaker stratification and stronger horizontal flows compared to other strong currents, which are probably the primary contributors to the EB nature in the ACC. Previous observational studies in the ACC (Phillips and Bindoff (2014), Ferrari et al. (2012)) have shown some broad consistency with the relation (1), showing vertical coherence and small turning of velocity vectors with depth, the turning increasing in regions of strong cross-topographic flows, where large vertical velocities would be expected.

Ratios and angles between the float and SSH derived velocities are binned as a function of surface speed (Figure 2.6). Both the ratios and the angles ($\theta \approx \phi_z.h$, where h is the depth) are more variable for slower surface speeds than faster surface speeds. The increased turning of the floats with slower speeds is in agreement with the relation discussed above (equation 2.1). One might also expect there to be more turning in the Scotia Sea relative to the Southeast Pacific due to

14

stronger vertical velocities being generated by rougher topography (Hughes (2005), Thompson and Naveira Garabato (2014), note the topographic features in Figure 2.1) and there is some evidence for this difference (Figure 2.6c, d). However it is important to point out that the slower surface speeds (specially below 0.1m/s) are associated to a greater mean velocity ratio and more variability of the ratio and angle between float speed to surface speed can be a result of errors associated with the altimeter SSH measurement. To resolve flows with surface speed of $0.1m/s$ the SSH changes need to be resolved with an accuracy of $2.5cm$ over a length scale of 25km (using the relation $\psi = g\eta/f$). This is below the accuracy limit on most altimeters, example OSTM/Jason-2 sensors have an accuracy of about 3.3cm. We conclude that there is an indication of more turning with depth and non-EB behavior in the Scotia Sea versus the South East Pacific, but due to large errors this result is not entirely conclusive.

Vertical structure of basin averaged velocities and their associated EKE (Figure 2.7) were computed using the raw velocities with no filtering, in contrast to what was done previously to compare to SSH. The mean zonal velocity decreases from a value of 6cm/s at 600m to close to 1cm/s at 2400m in the Southeast Pacific Ocean. The mean meridional velocity is close to zero ($< 1cm/s$) but with a slight southward flow component, associated with the southeastward ACC flow in this region. The EKE in the Southeast Pacific Ocean shows a decrease with depth, dropping from a value of $80cm^2/s^2$ to $20cm^2/s^2$. The zonal and meridional EKE have a similar structure in the vertical, with a slightly higher meridional EKE. The Scotia Sea has a velocity profile that shows higher magnitudes of mean speed and velocity variance than the Southeast Pacific Ocean sector and also decreases with depth. The mean zonal velocity decreases from 10cm/s at 400m to 5cm/s at 1800m. The mean meridional velocity is positive as the ACC flows north with speeds of 6cm/s near 400m decreasing to 1cm/s at 1800m. The EKE are similar, with slightly higher zonal EKE, in the zonal and meridional directions, from $250cm^2/s^2$ at 400m to $60cm^2/s^2$ at 1800m. The EKE in both the Southeast Pacific Ocean and Scotia Sea decrease rapidly up to about 1300m and then the decrease becomes more gradual. Also, in both the regions the energy of the mean flow is smaller than the eddy kinetic energy. A comparison of these results to those of fixed current meter estimates is provided at the end of this section.

2.3.2 Horizontal Structure of Flow

The mean flow was estimated by binning the float velocities into 2.0^o zonal by 0.5^o meridional bins. This choice was made based on the knowledge that the structures present in the mean flow, such as jets, have greater meridional spatial variability. The size of the bins was chosen such that the bins were large enough to encompass sufficient number of data samples but also small enough to resolve the flow structures that are present in the mean flow. It is important to recognize that the variability or EKE estimates in each bin reflect not only the time variable component but also the mean horizontal shear that might be present in the region covered by the bin. As the floats were spread unevenly in the vertical in each bin, an adjustment/rescaling was done to the horizontal velocities to approximate the corresponding velocity at the $1400m$ depth level (this is the level where the highest number of float days were sampled). This adjustment was done assuming an EB structure and using the mean speed vertical profile in each of the basins, calculated using all the float velocities (separately for the Southeast Pacific Ocean and Scotia Sea). Adopting this rescaling approach ensured more statistical reliability based on the results shown in the previous subsection.

To emphasize the relation between the averaged data and the underlying trajectories we also present selected trajectory segments, chosen as follows. The float tracks were subdivided into 120 day segments and then for each segment the ratio (ϵ) of float displacement to the total distance was calculated as

$$\epsilon = \frac{\int_0^{120} \vec{u} dt}{\int_0^{120} |\vec{u}| dt} \tag{2.2}$$

where $\vec{u}$ is the velocity of the float and $|.|$ represents the absolute value. This ratio is always less than or equal to 1; for a straight line the ratio is 1 and for a full circle it is zero. This ratio was used to group the tracks into looping and other, non-looping segments.

In the Southeast Pacific Ocean there are three primary regions where looping is found (Figure 2.8, top). The first one is a single large eddy near the deployment line (105^oW) in which many floats were deployed. The second location is both upstream and downstream of the San Martin Sea Mounts. The upstream location is associated with the crest of the large meander where the flow appears to split into smaller eddies and the downstream location is associated with larger loops. The third region of looping is found around 85^oW and 60^oS. The straighter float tracks lie in regions of time mean jets, as seen in Eulerian means discussed below, which are located on the northern and southern sides of the looping regions. In the Scotia Sea the strong recirculation of the

Yaghan Basin stands out (Figure 2.9, top). There is another looping area where the EKE increases for the second time downstream of the Yaghan Basin. The straighter trajectories appear to trace out the continental slope and West Scotia Ridge, similar to the strong mean flows discussed below.

The binned mean velocity field in the Southeast Pacific Ocean (Figure 2.8, bottom) shows primarily an eastward zonal flow in two principal jets spaced approximately 200km apart, with a small southward component. The maximum bin averaged speeds at 1400m are approximately 6-8cm/s in the core of the jets. We identified these jets as the SAF and PF based on the hydrographic properties associated with strong flows that were observed during the deployment cruises (not shown). The PF shows a meander in the binned mean flow upstream of the San-Martin seamounts at 95^oW, 59^oS, which seems to be associated with the barotropic PV (f/H). This is probably the reason for the repeated appearance of the large meander at this location, as may be seen in Hovmoeller plots of SSH (not shown) and by the two float deployments. The San Martin seamounts at 95^oW, 59^oS are associated with a weaker mean flow, extending downstream of the seamounts.

The meandering of the jets upstream of the San Martin seamounts is associated with a slightly higher EKE. The northern jet flows along f/H contours near 57^oS and 90^oW, and weakens downstream where the f/H contours diverge. This divergence of f/H contours is collocated with a tongue of high EKE - the highest in the Southeast Pacific Ocean - that is also one of the regions where large looping is seen. The standard deviation ellipses in this region are primarily isotropic, with a slightly greater zonal component associated with the region where the highest EKE is observed in the region.

In the Scotia Sea (Figure 2.9, bottom), the strongest average speeds near the 1400m level are 14-16cm/s, twice that of the Southeast Pacific Ocean. The mean velocity vectors in this region have a northward component associated with the ACC turning north and crossing over the North Scotia Ridge. The velocity shows the ACC approaching the Shackleton Fracture Zone as a single broad jet, with the strongest flows located near the northern side of the Drake Passage. This jet splits into two branches as it crosses the Shackleton Fracture Zone. The northern branch closely hugs the continental slope of South America, like a boundary current, and the southern branch goes south of the Yaghan Basin over the West Scotia Ridge. A strong cyclonic recirculation associated with the topographic depression in the Yaghan Basin, as the mean velocity vectors turn westwards

in the center of the basin. The segments of the trajectories shown in Figure 2.9 also showed the presence of a recirculation in this region.

High EKE is evident downstream of the Hero Fracture zone and Shackleton Fracture zone, in the Yaghan Basin (Fig. 12). This increase in EKE is probably associated with instabilities related to the crossing of two fracture zones and the time variability of the Yaghan Basin topographic recirculation. The highest EKE signal in the Scotia Sea is found near 56^oS and 51^oW. This is downstream of the region where the two topographic jets merge and possibly interact with a topographic bump located at 54^oW and 55^oS. This region also shows significant looping in the trajectories. The standard deviation ellipses, similar to the Pacific Ocean sector, do not have a strong preferred orientation except in some bins near the boundaries, where they are oriented zonally along the topography.

2.3.3   Comparison to Previous Flow Estimates

Previous flow measurements in the region sampled here can be divided into three broad categories: current meter mooring experiments (Sciremammano et al. (1980), Ferrari et al. (2012), Ferrari et al. (2013)), synoptic sampling of flow by ADCP measurements from ships (Lenn et al. (2007), Chereskin et al. (2010), Firing et al. (2011)) and analysis of SSH derived flow fields (Barré et al. (2011)). Each method of flow measurement, including the Lagrangian analysis provided in this study, has advantages and disadvantages. The Lagrangian analysis provided here has the advantage that it can provide a wealth of information about the spatial structure of the flow over a large region, thus providing a representation of the spatial structure and a sense of the connections by the mean flow between different regions. It is important to realize that a direct comparison of Lagrangian data averaged over a large region (basin average), to that of a current meter collecting data at a specific location will not necessarily provide an exact match. This is because in a large area average the Lagrangian instruments average over different flow features and, accounting for flow reversals and recirculation, the mean flow is expected to be slower than the estimate that would be observed by a fixed current meter. Also the estimate of EKE in this large area average would be a measure of both the temporal variability and spatial structure of the flow.

In a qualitative sense our vertical profiles of velocity and EKE are nevertheless comparable to the current meters at Drake Passage (Sciremammano et al. (1980), Ferrari et al. (2012), Ferrari et al. (2013)). The current meters show mean velocities on the order of 5-40cm/s at 500m decreasing

to 2-10cm/s at 2000m, where the variation evidently is due to the range of features associated with spatial locations sampled by the current meters. Also, the vertical structure of EKE compares well with the estimates of the variability from current meters. The slight preference for zonal variability over meridional as seen on a large scale in the Scotia Sea (Figure 2.7 bottom) and in the velocity ellipses, especially near topography (Figure 2.9), has also been seen in current meters that were situated near topographic features. For example, the large cyclonic circulation resident in the Yaghan basin was previously observed in current meter and SSH fields (Ferrari et al. (2012)). Lenn et al. (2007) and Firing et al. (2011) noted the permanence of a jet like feature, associated with the SAF, near the continental slope of South America and a slightly more variable jet associated with the PF passing over the West Scotia Ridge. Chereskin et al. (2010), using estimates of the quasi-synoptic flow field in the Southeast Pacific Ocean from two observational campaigns in 2005 and 2006, indicated the presence of a jet similar to our northern jet in the Southeast Pacific sector.

2.4   Length Scales, Time Scales and Isopycnal Stirring

For the analysis that follows we divided the region into six groups, unless otherwise noted, as follows: three divisions in the zonal direction ($110^oW - 90^oW$, $90^oW - 70^oW$ and $70^oW - 40^oW$) and two divisions in depth (500 - 1400 m and 1400 - 2500 m). For each division, the mean ($U_i =< u_i >= 1/N \sum u$), where the sum is over all available observations and N is the number of observations, and residual ($u_i' = u_i - U_i$) velocities were calculated. Subscripts i represent the direction and can take on values of u (zonal) or v (meridional); for example u_u would imply the zonal component of the velocity. In the following we do not follow the Einstein notation; repeated index does not imply summation. The means and the corresponding variances are presented in Table 2.1. The errors were calculated using standard error calculation methods as described by Ollitrault and Colin de Verdière (2002). The Reynold's fluxes (not shown) were calculated and are negligible for such large area averages.

Spatial correlations are calculated as

$$C_{ii}^e(r) = \frac{< u_i'(x)u_i'(\vec{x} + r) >}{< u_i'(\vec{x})u_i'(\vec{x}) >} \qquad (2.3)$$

where r is the separation between the floats and the averaging is done in 50 km r bins using samples from float pairs. C_{ii}^e has a structure that is commonly seen in eddying flows, decreasing

exponentially followed by a negative lobe (Figure 2.10). These spatial correlations are well resolved in the Southeast Pacific and the shallow Scotia Sea, but the deep Scotia Sea has large errorbars due to the scarcity of data. We interpret the negative lobe as a signature a dipole like pattern of cyclonic and anticyclonic eddies that are present in an alternating patterns (Chereskin et al. (2010), Barré et al. (2011)).

This correlation function was then used to calculate the quasi-Eulerian integral length scale.

$$L_{ii}^e = \int_0^\infty C_{ii}^e(r)dr \tag{2.4}$$

This calculation is done using two methods as described below because we cannot integrate observational correlations to infinity, which would also not be effective due to large scale inhomogeneities in the ocean. A Monte-Carlo like error estimation method is used to calculate errors, which is similar to the ones used before (Sallée et al. (2008b), Garraffo et al. (2001)). In this method, 1000 noisy correlation curves are generated using the mean correlation curve and adding the standard error multiplied by a random number between -2 and 2 for each distance bin from a uniform distribution. Note that because the standard errors are small (as can be seen by error bars in Figure 2.10), this procedure did not produce correlation coefficients that are very different from the mean. For the first estimate of the integral length scale these noisy correlation curves are integrated out to the first zero crossing. In the second method an exponentially decaying cosine function is fit to the noisy correlation curves and the integral length scale is given by the analytical integral of the functional form. Both methods produce 1000 estimates, corresponding to each noisy correlation curve that was generated. The average of these estimates is taken to be the integral length scale and the error is represented as one standard deviation of these estimates. The results are shown in Table 2.1.

The integral length scale provides an estimate of the spatial length scale over which velocities decorrelate. The integral length scales calculated by integrating to the first zero crossing are on the order of 60km for most the region. However, the integral length scales calculated by fitting an decaying cosine function vary from 60km in the western Southeast Pacific Ocean to about 10km in the deep Scotia Sea. This difference is due to the presence of a stronger negative lobe (Figure 2.10), probably due to paired dipoles, in the strongly eddying flow of the Scotia Sea. We also present the distance at which the first and second zero crossing occur for the correlation function. This gives a sense of the distance at which the velocities broadly reverse, or the diameter of the

eddies. This scale is approximately 120 km for the Southeast Pacific Ocean and decreases in the Scotia Sea (Table 2.1), similar to the integral length scales. This estimate of eddy size is in broad agreement with the eddy sizes calculated for this region using SSH fields (Chelton et al. (2011)). Chereskin et al. (2010) estimated wavelength of meanders to be between 250-300km, which is in good agreement with our eddy sizes (with a wavelength the size of a dipole). Broadly speaking, the spatial correlations and length scales of the residual velocity are approximately isotropic, without any clear preference for any direction.

To inspect the properties in frequency domain we divided the trajectories into 120 day segments. Each segment was assigned its corresponding spatial bin based on its mean position and mean depth, which was then used to calculate a time series of residual velocities. The binned time series are then used to calculate the normalized Lagrangian frequency spectra $S(\omega)$, normalized by the velocity variance, of the residual velocity. The normalized Lagrangian spectra are also generally isotropic similar to the spatial correlations. We checked the rotary spectra (not shown) to look for preference of anticyclonic vs cyclonic motions and did not find any such preference.

The variance preserving form $(\omega.S(\omega))$ of the normalized Lagrangian frequency spectra (Figure 2.11) generally shows a broad peak. Strikingly, the peak migrates from periods of approximately 60 days in the deep western part of the Southeast Pacific Ocean to periods of 20 days in the shallow Scotia Sea. Also, the peak in the deeper bin is located at relatively lower frequencies than the shallower bin. This shift of peak in frequency can be explained simply as a consequence of Doppler shifting in the presence of mean flow. In this region of the ACC, the eddies persist for times on the order of few weeks to months and have propagation speeds less than 1cm/s (Chelton et al. (2011)). This (fixed flow regime) implies that as the floats move through the eddies (at 5 -10cm/s) they experience a nearly stationary eddy field and the time variability in the time series of the floats is generated mostly by the floats meandering through the stationary eddies. In this setting, a slower moving float as in the Southeast Pacific Ocean will experience the variability at a lower frequencies, while a faster moving float, as in the Scotia Sea, will experience the variability at higher frequencies. Chen et al. (2015) formally showed that the Lagrangian and Eulerian frequency spectra can be related as $S_{Eulerian}(k,l,\omega) = S_{Lagrangian}(k,l,\omega+|U|k)$, where $|U|$ is the zonal mean flow, k is the zonal wavenumber and l is the meridional wavenumber.

Our data set, similar to previous float studies (Rupolo et al. (1996)), shows a commonly observed spectral shape (Figure 2.12). The spectra plateau at lower frequencies is required for the Lagrangian time scale and diffusivity to be well defined as $S(0) = 2(2\pi)T_l$ where T_l is the Lagrangian integral time scale, $S(0)$ is the normalized Lagrangian frequency spectra at zero frequency that was normalized by the velocity variance and the 2π appears due to way the spectra was defined. The spectra at the highest frequencies (periods smaller than 7 days) have a spectral slope that is steeper than -3, which is required for the Lagrangian micro-scale or the acceleration time scale to be well defined (Hua et al. (1998), Rupolo et al. (1996)). There is also a range in-between with spectral slopes of approximately -2, as would be expected from a simple first order stochastic model of the variability (LaCasce (2008)).

The binned time series, 120 day segments defined above were also used to calculate the velocity autocorrelation.

$$R_{ii}^l(\tau) = \frac{< u_i'(t)u_i'(t+\tau) >}{(< u_i'(t)u_i'(t) >)} \tag{2.5}$$

The angular brackets represent averaging over the trajectories that are present in the bin. This correlation is then used to find the Lagrangian integral time scale.

$$T_{ii}^l = \int_0^\infty R_{ii}^l(\tau)d\tau \tag{2.6}$$

Structurally, R_{ii}^l looks similar to C_{ii}^e: there is a decay and oscillations, usually with a prominent negative lobe. This structure would be expected based on a turbulent field in which the flow decorrelates in time but also has the presence of significant looping and meandering. This can be approximated as a function of the form:

$$R_{ii}^l(t) = e^{-t/T_{eii}}cos(2\pi t/4T_{dii}) \tag{2.7}$$

where T_{eii} is a decay scale, T_{dii} is the time of first zero crossing or the meander time scale and the subscripts i, j represent the directionality. This form is fit to the mean autocorrelation functions; the parameters and error in fits is calculated using bootstrapping. This is done using the Monte-Carlo like method of producing noisy correlation functions as described above, used for spatial correlation integration. Previous observational studies using Lagrangian measurements (Sallée et al. (2008b), Garraffo et al. (2001)) have fit a functional form of the type shown above or similar forms. It should be remembered that this fitting exercise primarily captures the decay and the first negative lobe of

22

the autocorrelation function, which produces a "local" estimate of of the time scale. The analytical integral of this chosen autocorrelation function gives an effective Lagrangian integral time scale

$$T_{ii}^l = \frac{4T_{eii}T_{dii}^2}{\pi^2 T_{eii}^2 + 4T_{dii}^2} \tag{2.8}$$

Klocker et al. (2012) applied the mixing suppression theory (Ferrari and Nikurashin (2010)) to particles instead of tracers and derived an autocorrelation function of the same form as equation (7). This links physical processes to the presence of the two scales using dynamical arguments. Their theory was derived for a randomly forced Rossby wave solution to a quasi-geostrophic system. The non-linear terms, used as forcing for the Rossby waves, were parameterized as a sum of a white noise process and linear damping. The decay time scale (T_{eii}) was associated with the the linear damping time scale. The oscillation time scale (T_{dii}) was based on the dominant wave number multiplied by the difference of mean speed and observed phase speed. This difference is associated with the mean PV gradient based on the dispersion relation for linear Rossby waves. Their expression for the autocorrelation is (their equation 18)

$$R_{vv}(t') = \frac{2k^2 EKE}{K^2} e^{-\gamma t'} cos[k(c_w - U)t'] \tag{2.9}$$

where k is the zonal wave number, K is the amplitude of the total wave number, γ is the linear damping constant, c_w is the observed phase speed and U is the mean zonal speed. Based on this model, a stronger PV gradient (larger $|c_w - U|$), holding the damping time scale constant, would call for the the oscillation time scale to be relatively smaller. This would, in turn, imply a more prominent negative lobe in the autocorrelation function. A larger negative lobe implies a smaller Lagrangian integral time scale and smaller eddy diffusivities.

Based on eqn (2.9) and using the same form as equation 2.7 we can calculate a theoretical meander time scale using the binned mean flow, observed feature propagation speeds (c_{wi}) from Fu (2009) and observed length scales.

$$2T_{dii}^{theory} = \pi/(k_j.(c_{wj} - U_j)) \tag{2.10}$$

Where the repeated index does not imply summation (as we are not following the Einstein notation in this section).

These time scales are presented in Table 2.1. The integral time scale (T_{ii}^l) approaches the decay time scale (T_{eii}) as the meander time scale (T_{dii}) gets relatively longer. This happens when the

meander time scale is long since the amplitude of the autocorrelation function will decay to a very small value before the negative lobe can significantly affect the integral. This leads to the fitted zonal meander time scale (T_{duu}^{theory}) being very large (> 500days) for most of the bins and those results are not shown in the Table.

The decay time scale is about 10 days in the Southeast Pacific Ocean and 6 days in the Scotia Sea, and generally increases with depth. This is to be expected if simple scaling arguments like $T_{eii}^2 \frac{1}{|k|^2 u_{ii}'^2}$ roughly hold and the length scales do not vary much with depth. This result is different than the result in Lumpkin et al. (2002); they found that the time scale remained roughly constant with depth as the length scale and EKE decayed with depth in the North Atlantic Ocean. The Eulerian time scale calculated using current meters in different parts of the ACC are close to 20 days (Phillips and Rintoul (2000)). It is not surprising that the Eulerian timescales are larger than the Lagrangian time scale, as in the ACC the floats propagate through Eulerian features faster than the Eulerian features pass through a region (Middleton (1985)).

We then use these time scales and EKE to calculate the eddy diffusivities ($\kappa_{ii} = EKE.T_{ii}^l$). These diffusivity estimates are also "local" diffusivity estimates, similar to the time scales, due to the nature of the fitting procedure to an early time autocorrelation function. The meridional diffusivities are similar in the two Southeast Pacific Ocean bins ($110^oW - 90^oW$ and $90^oW - 70^oW$); approximately $2500 \pm 500 m^2/s$ in the shallower bins and $1400 \pm 250 m^2/s$ in the deeper bins. The meridional diffusivity is approximately $3200 \pm 1000 m^2/s$ in the Scotia Sea. The zonal diffusivities are generally greater, and this is to be expected because they are enhanced by both the mean horizontal shear and mean vertical shear, which cannot be completely removed by removing a bin averaged mean to find the residual velocities. In the Scotia Sea both the zonal and meridional diffusivities seem to be affected by these shears.

Using the result from the above analysis, that the time scales and the diffusivities are similar across the Southeast Pacific Ocean, we use all the tracks between $110^oW - 70^oW$ and increase the number of vertical bins to resolve better the vertical structure of diffusivity. The time scales and diffusivity are calculated the same way as above by fitting equation 2.7 to the autocorrelation function and calculating the time scales. The fitting procedure provides the decay time scale (T_{eii}) and the meander or zero crossing time scale (T_{dii}). The Lagrangian time scale is then calculated using equation 2.8. The decay time scale shows a peak at 1100m, the meander time scale shows a

24

peak at 1500m corresponding to the critical level and the Lagrangian integral time scale shows a peak at 1500m (Figure 2.13b).

The diffusivity calculated using only the decay time scale ($K_o = EKE.T_{eii}$), the diffusivity calculated using the Lagrangian integral time scale (called the suppressed or expected diffusivity, $K = EKE.T_{ii}^l$) and the theoretical estimate of diffusivity ($K^{theory} = \frac{4EKET_{eii}T_{dii}^{theory2}}{\pi^2 T_{eii}^2 + 4T_{dii}^{theory2}}$) from Klocker et al. (2012) are shown together (Figure 2.13a). The eddy diffusivity (K) decreases from around $2800 \pm 600 m^2/s$ at 700m to around $990 \pm 200 m^2/s$ at 1900m. In the calculation of K^{theory} the observed decay time scale is used along with a length scale of 100 km, approximately the eddy size, as this length scale provided a better fit against the observed diffusivity than using the calculated integral length scale from spatial autocorrelations. Thus, the theoretical value should be regarded as a fitted form rather than an absolute prediction. The presence of mean flow or the presence of a negative lobe in the autocorrelation function suppresses diffusivity, which is evident as K_o is greater than K and the Lagrangian integral time scale is smaller than the decay time scale everywhere. Even though the Lagrangian integral time scale shows evidence of a mid-depth (approx 1500m) maxima, no such maxima is seen in the diffusivities. This suggests that the structure of the diffusivities in the ACC is more strongly controlled by the EKE, rather than the Lagrangian time scale. This is to be expected as the EKE varies by a factor of 3-4 in the vertical (Figure 2.7), whereas the Lagrangian integral time scale variations are less than 20%.

Geographically binned eddy diffusivities, as for horizontal velocities in previous sections, were not calculated for two main reasons. Firstly, it has been pointed out that diffusivities calculated as $< X^2 > /2T$ or some similar measure (LaCasce (2008)) can take 6 months or longer to asymptote to a constant value. Hence, calculating binned diffusivities is problematic, as the floats spend only a fraction of 6 months in a given bin. Secondly, the floats are spread in the vertical; for the mean flow calculations we could use the EB assumption to rescale the float velocities to a common depth level but no similar procedure can be applied to rescale the float trajectory to a common depth level. What we have presented in this section are average diffusivities, but with the choice of the averaging over very large area ($30^o lon \times 10^o lat$), much larger than the bins for the mean flow. Previous float and drifter studies have presented diffusivities in geographic bins of the same size as those used for mapping the mean flow (e.g. Ollitrault and Colin de Verdière (2002), Swenson and

Niiler (1996)), but using data that were primarily limited to a certain depth level or the sea-surface; even so, attributing error estimates to geographic bins may be problematic in regions of strong flow.

Thus far only zonal and meridional diffusivities have been estimated. As the aim of the DIMES experiment was to quantify cross-stream diffusivities, we continue the analysis in cross-SSH coordinates with dispersion calculated for the Southeast Pacific Ocean and the Scotia Sea float tracks divided into two depth bins (Figure 2.14). The diffusivity is estimated as $< X^2 > /2T$, where X is the cross-stream distance. This calculation differs from the ones presented in Lacasce et al. (2014) in three ways. Firstly, their study did not separate the data into depth bins to tease out a vertical structure of eddy diffusivity, which is our main goal here. Secondly, we produce error estimates using boot-strapping, which was not done previously. Finally, we also attempt to produce estimates for the Scotia Sea.

The diffusivity estimates, using the relation above ($< X^2 > /2T$), are approximately $690 \pm 150m^2/s$ and $1000 \pm 200m^2/s$ for the shallow (500-1400m) and deep (1400-2500m) Southeast Pacific Ocean floats. Note that the deeper level estimates of diffusivity in the Southeast Pacific Ocean are similar to the meridional diffusivities calculated above using the autocorrelation fitting procedure. In the Scotia Sea the diffusivities are approximately $1200 \pm 500m^2/s$ for both shallow (500-1000m) and deep floats (1000-2000m) but with larger error bars. These depth ranges are different in the two basins and were chosen to allow for an almost equal data distribution in both depth bins. The division between Southeast Pacific Ocean and Scotia Sea was chosen to be 70^oW. The error bars on the dispersion are calculated as one standard deviation of all bootstrapping samples where the trajectories are resampled allowing for repeats and the dispersion curves calculated 1000 times. For the diffusivity curve, the error is the range of slopes that fit between the errorbars of the dispersion curves. In the Southeast Pacific Ocean there are about 55 floats for each depth bin on the first day and this number only marginally decreases to about 45 by day 250. However in the Scotia Sea on the first day, there are about 40 floats but within 150 days this number decreases to around 15.

The estimate of diffusivity at the shallower level in the Southeast Pacific Ocean is significantly smaller than estimates provided earlier by the fitting procedure, almost by a factor of 4. This is because the diffusivities and Lagrangian time scale estimates do not asymptote to a fixed value for very long times, whereas the fitting procedure only produces early time results. A similar long term decay, beyond the first negative lobe, was also noted in Griesel et al. (2015). Lacasce

et al. (2014) had also shown that the diffusivities estimates take a long time to settle and after 6 months the shallower level diffusivities are smaller than the deeper level diffusivities. This can be understood by looking at the dispersion (Figure 2.14a); the dispersion for the shallow floats in the Southeast Pacific Ocean does not grow linearly but instead saturates after some initial (approx 70 days) increase, whereas the dispersion from the deeper floats in the Southeast Pacific Ocean increases almost linearly as would be expected for a diffusive process. This almost linear increase for the deeper floats is the reason that the estimates using the autocorrelation fitting and dispersion produce similar results. To confirm this, the model particle calculations of Lacasce et al. (2014) were revisited (not shown). Calculations of dispersion at shallower levels showed saturation after an initial growth period of about 50-100 days, similar to the saturation seen in Figure 2.14.

Saturation of dispersion at long times, as seen at the shallower level, can be expected if the diffusivity is inhomogeneous in the cross-stream direction with regions of high diffusivity being flanked by regions of low diffusivities. Considering the mean flow field calculated in the previous section, we infer that these inhomogeneities are a result of time mean jets acting as barriers to mixing at shallower levels. The long term effects of barriers on mixing would not be captured by the fitting of autocorrelation by equation 2.7 as done previously in this section, nor would this behavior be predicted by the form of diffusivity derived by Klocker et al. (2012) or Ferrari and Nikurashin (2010). We also note that the discrepancy between cross stream and meridional diffusivities is not due to the choice of coordinates, as in the Southeast Pacific Ocean the SSH contours are almost zonal (Tulloch et al. (2014)).

In the Scotia Sea the use of the across SSH dispersion allows the quantification of cross-streamline diffusivity, which cannot be done by calculating zonal and meridional diffusivities (Table 2.1). It can be asked if the spreading in the Scotia Sea is indeed Gaussian and diffusive or, on the contrary, anomalous, hence a non-diffusive parametrization is needed to represent it. With our limited data set we are not able to answer this question conclusively.

Overall, our results properly interpreted appear to be consistent with previous notions and results, discussed in detail in the next section. Jets are faster at shallower levels and act as stronger barriers to mixing, while at deeper levels the jets slow down and the barrier effect becomes weaker. Also, the regions between the jets at shallow levels are more strongly mixed than at deeper levels simply because of the higher EKE at shallower levels.

2.5 Discussion

The DIMES floats provide a striking set of trajectories that quite clearly show both the large-scale circulation and the macroturbulent nature of the flow in the ACC. The floats sampled depths between 500 and 2500 m from 105^oW to 40^oW, primarily between the SAF and PF. At a depth level of approximately 1400m in the Southeast Pacific Ocean the mean speeds ranged from 6 cm/s in the jets to 1cm/s between the jets, whereas in the Scotia Sea the typical speeds were almost doubled. The EKE in the two regions also differed substantially, $10 - 60cm^2/s^s$ in the Southeast Pacific Ocean, and $20 - 140cm^2/s^2$ in the Scotia Sea, at similar depths. The EKE and the mean speeds increase dramatically as the flow crosses over the Hero Fracture Zone and Shackleton Fracture Zone, from the relatively calm Southeast Pacific Ocean to the vigorously unstable Scotia Sea. Our results (below 500m depth) show congruence with the SSH derived velocities but little change with depth, we do not see any evidence of greater turning in deeper versus shallower bins. This good semblance to the flow at the surface observed by satellites and leads us to believe that the flow is EB to first order. Our results show excellent qualitative comparisons and good quantitative comparisons to previous studies in limited regions, discussed as the end of section 3, and extend our current maps of the mid-depth flow over a larger, region of the Southeast Pacific Ocean and Scotia Sea.

The integral length scales generally varied between 20-60km and the length scale of the first zero crossing, which we believe is the dominant eddy length scale, varied between 50-120km, generally decreasing from the Southeast Pacific to the Scotia Sea and with depth. This decrease with depth bears some resemblance to the quasi-geostrophic simulations of Smith and Vallis (2001) with the case of non-uniform stratification. The mean jets, seen in the maps of the mean fields, meander at length scales similar to the eddy length scales in the Southeast Pacific Ocean and scales set by the scale of the topography in the Scotia Sea. These meandering structures of the Southeast Pacific Ocean are probably transient, as there is no topography that can maintain them, but persist over time scales that are longer than time scale of passage for the particles through the region, which is the reason they appear in the mean field, and could be significantly affecting the spreading of tracers.

The spacing between the jets in Southeast Pacific Ocean basin, which does not have extreme topographic features like the Scotia Sea, is initially set upstream by the spacing between the fracture zones in the Pacific-Antarctic Ridge (upstream of the experiment site). Subsequently, the

approximately 200km spacing seen in this region is probably set by a combination of the weak non-uniformities in barotropic PV (f/H) gradients, upstream effect of the seamounts and turbulent mechanisms operating on the Rhines' scale (approximately 200kms). The topographic features will play a role in setting the circulation at mid-depth if the velocities along the bottom are non-trivial, which (for depths greater than 2500m) is a criteria that cannot be tested by these data. However, previous studies have shown the presence of strong bottom flows in a few locations in the ACC. The visual correspondence between the f/H field and mean flow features seen here leads us to believe that even in this relatively smooth and deep region of the ACC, the bottom exerts some influence on the flow.

Quantifying the isopycnal stirring was one of the main motivations behind the DIMES float experiment. The floats provide the first ground truth of the stirring processes at work in the ACC. They clearly show the presence of jets in the flow and strongly suggest that these jets form transport barriers, whose effect decreases with depth. Although the long-time limit of diffusivity in the Southeast Pacific ocean shows stronger mixing at depth, with cross stream diffusivities of $690 \pm 150 m^2/s$ between 500-1400m and $1000 \pm m^2/s$ between 1400-2500m, a more local estimate of diffusivity, produced by fitting a functional form to the autocorrelation function, shows a decrease with depth that follows the general structure of the EKE as the variation of the Lagrangian time scale with depth is small. The Lagrangian time scales, which do show a mid-depth maxima near the critical level, seem to be suppressed in accordance with mixing length suppression arguments of Ferrari and Nikurashin (2010).

The vertical structure of the integral time scale and relation to mixing has previously been discussed by Lumpkin et al. (2002), who observed that deep Lagrangian time scales from float measurements in the North Atlantic Ocean show only modest increase with depth, whereas eddy energy decreases with depth much more rapidly. This was shown to be consistent with a field of rapidly evolving nonlinear eddies and relatively slow wave speeds. Similarly, but from an analysis of numerical simulations of the ACC, Griesel et al. (2015) concluded that the vertical structure of mixing is dominated by that of the EKE.

In the last few years a number of studies have addressed the eddy diffusivity and its vertical structure in the ACC. Using the data from the DIMES experiment Lacasce et al. (2014) presented a single vertically averaged isopycnal diffusivity from a subset of the float data as here and Tulloch

et al. (2014) provided a measure of diffusivity at the deeper isopycnal level based on tracer measurements. These studies also presented a vertical structure of diffusivity that was calculated by releasing particles and tracers in a model and advecting them using the model velocity field. Their modeling results showed that the vertical structure of diffusivity had a mid-depth maxima of about $1000m^2/s$ at approximately 2000m and it was reasoned that this was a result of mixing length suppression at shallower depths in the presence of stronger large-scale mean flow. However, it took longer than 6 months to asymptote to this value using the particles, and a long term (100-500 days) linear fitting was done to the second moment of the tracer concentrations.

In contrast, Bates et al. (2014) presented an area averaged diffusivity by fitting a form of the result from Ferrari and Nikurashin (2010) to SSH observations and ECCO output and did not obtain a mid-depth maxima in diffusivity. Bates et al. (2014) results were based on using a length scale that was calculated from SSH fields (Chelton et al. (2011)), assuming it to be the dominant length scale. We showed that this choice of length seems to be crudely correct for estimation of local diffusivities. Recently, Chen et al. (2015) provided diffusivities in the DIMES region using an approach that accounts for contributions of multiple length scales by integrating over the wavenumber-frequency spectra in the region. Interestingly, their spatial maps of eddy diffusivities show a significant degree of inhomogeneity. To calculate a single vertical profile of eddy diffusivity over the region they do a simple area averaging, similar to Bates et al. (2014). They obtain some hints of a mid-depth maxima in their results but generally the trend of eddy diffusivity is to decrease with depth. Griesel et al. (2015) also used a numerical model and particle trajectories, which were 130 days long, and did not observe a mid-depth maxima of diffusivity in the Southeast Pacific Ocean. Naveira Garabato et al. (2011) calculated mixing lengths in the ACC using hydrographic data and showed the presence of suppressed mixing lengths in frontal regions of the ACC, at least in regions of smooth topography and essentially zonal jets. Naveira Garabato et al. (2011) applied the mixing suppression ideas in a more local sense, by calculating the mixing length as the RMS temperature fluctuation divided by the large scale temperature gradient on neutral surfaces.

In summary, the recent results described above can be divided into three categories: localized synoptic estimates (Naveira Garabato et al. (2011)), spatially averaged Eulerian estimates (Bates et al. (2014), Chen et al. (2015),Griesel et al. (2015)) and long term (6 months of longer) estimates

from Lagrangian passive tracers (Lacasce et al. (2014), Tulloch et al. (2014)). The discrepancy between the spatially averaged Eulerian estimates, which are similar and compare well to our estimates using a functional fit to the Lagrangian autocorrelation function (Figure 2.13a), and long-term Lagrangian passive tracer estimates, which are similar and compare well to our second estimate using long term cross-stream dispersion calculations (Figure 2.14), arises because of the nature of the averaging used to estimate a mean diffusivity over a large region. The correct way to average diffusivities in a cross stream direction was shown in Nakamura (2008) for the atmospheric case. Using a 1D, zonally averaged model the correct predictor of eddy diffusivities was shown to be the harmonic average ($K_{average} = (\int 1/K(y)dy)^{-1}$), where regions of low mixing dominate the average. This model holds if the region has barriers that are invariant in time; a zonally uniform flow (along stream) might be a good assumption for the Southeast Pacific Ocean as discussed earlier. Hence, a Lagrangian passive tracer spreads through a region and converges to the harmonic mean rather than an area average, as was made in the Eulerian estimates.

The regions within the ACC where the EKE is high and the mean flow is weaker, such as between localized jets, have large diffusivities and are well-mixed regions, while the regions of strong jets act as barriers to cross-stream mixing. However, if the jets merge and split they might not always be barriers to mixing. Probably because the Southeast Pacific Ocean is a relatively simple region, the jets persist for long durations without much splitting and merging and act as barriers. This nature of the Southeast Pacific Ocean was previously noticed by Thompson et al. (2010), who showed in a numerical model that the region between the Udintsev Fracture Zone and the Drake Passage had the greatest number of distinct PV pools or regions of homogenized PV, compared to any other region of the Southern Ocean, suggesting that strongly mixed regions exist in the Southeast Pacific Ocean but there is little mixing between each of them.

The potentially important role of the Scotia Sea to cross-stream mixing makes estimates for this region of great interest. There are fewer data in the Scotia Sea, however, and this lack of data produces noisier estimates, with average cross stream diffusivity of approximately $1200 \pm 500 m^2/s$ both in the shallow and deep bins. The results for the Scotia Sea are plagued not only by the scarcity of data but also by the presence of an extremely complex mean flow pattern. The complexity of topography in this region can create flow structure in the deeper layers significantly different from that in the flow above, leading to strong vertical motion and currents that (locally) cross

the core of the ACC. One example of this is the generation of mid-depth vortices from the flow along the northern boundary of the Scotia Sea which move southward, across the major fronts (Brearley et al. (2014)). Another example is seen in the floats that continued east in the Scotia Sea, instead of crossing over the North Scotia Ridge into the Argentine Basin (Fig. 11). These deep, topographically-linked currents can transport water across the major fronts of the ACC in a non-diffusive fashion, and indeed may be a crucial component of overturning.

The ACC is not zonally homogeneous and in most regions the jets are transient features of flow that do indeed merge and split. In such a complex system, it is not clear that a simple measure of mixing is appropriate. Several approaches to estimating the diffusivity lead to the conclusion that strong inhomogeneities exist in this quantity, related to jets and thin barriers to mixing within the broader ACC system. This may have lead to disparate previous results, based on the chosen averaging method. Using Lagrangian observational methods, however, we are able to reveal some of this complexity and point to dynamical structure in the flow that controls mixing.

Table 2.1: Statistics for DIMES RAFOS floats in six longitudinal and depth bins

Longitude bins	$110^oW - 90^oW$		$90^oW - 70^oW$		$70^oW - 40^oW$	
Depth bins	500 - 1400m	1400 - 3000m	500 - 1400m	1400 - 3000m	500 - 1400m	1400 - 3000m
$L_{uu}^e(km)$	75.09 ± 1.17	57.81 ± 0.79	73.45 ± 6.1	77.90 ± 6.64	57.47 ± 3.16	56.60 ± 9.62
$L_{vv}^e(km)$	92.03 ± 1.53	60.97 ± 0.99	65.59 ± 2.35	77.11 ± 8.12	68.49 ± 5.12	62.22 ± 16.06
$L_{uu}^e(fit)(km)$	63.88 ± 2.03	36.06 ± 1.11	56.56 ± 5.19	14.78 ± 3.91	28.34 ± 5.29	14.11 ± 7.91
$L_{vv}^e(fit)(km)$	44.40 ± 2.18	29.96 ± 0.99	37.63 ± 5.25	31.80 ± 4.35	22.33 ± 3.83	13.8 ± 5.71
1st zero crossing C_{uu}^e(km)	123.17	104.09	121.18	97.1	87.20	49.2
1st zero crossing C_{vv}^e(km)	138.75	100.94	97.56	104.88	90.35	46.92
2nd zero crossing C_{uu}^e(km)	194.93	184.59	125.44	207.28	170.81	132.0
2nd zero crossing C_{vv}^e(km)	281.58	329.54	158.38	203.05	218.76	202.22
U(cm/s)	3.4 ± 0.33	2.25 ± 0.23	5.77 ± 0.65	3.83 ± 0.42	7.97 ± 1.38	6.68 ± 1.74
V(cm/s)	-0.6 ± 0.4	-0.51 ± 0.24	0.63 ± 0.64	0.01 ± 0.34	3.46 ± 1.43	2.4 ± 1.53
$c_{zonal}(cm/s)$	0.46 ± 0.98	0.46 ± 0.98	0.72 ± 0.86	0.72 ± 0.86	2.05 ± 1.73	2.05 ± 1.73
$c_{meridional}(cm/s)$	-0.18 ± 0.45	-0.18 ± 0.45	-0.07 ± 0.39	-0.07 ± 0.39	1.14 ± 1.41	1.14 ± 1.41
$u'u'(cm^2/s^2)$	35.45 ± 2.77	19.26 ± 1.4	80.14 ± 8.28	28.75 ± 3.16	215.5 ± 28.74	122.31 ± 27.14
$v'v'(cm^2/s^2)$	52.52 ± 4.1	21.94 ± 1.6	75.93 ± 7.84	26.27 ± 2.89	230.05 ± 30.68	94.57 ± 20.99
$T_{uu}^l(days)$	11.62 ± 1.58	10.98 ± 1.6	9.67 ± 1.68	12.72 ± 1.39	4.07 ± 0.82	5.89 ± 0.54
$T_{vv}^l(days)$	5.63 ± 0.74	7.77 ± 0.84	4.66 ± 0.64	6.29 ± 0.75	1.98 ± 0.44	3.35 ± 0.51
$T_{euu}(days)$	11.72 ± 1.59	13.14 ± 1.58	9.74 ± 1.63	12.95 ± 1.25	4.1 ± 0.68	9.35 ± 2.32
$T_{evv}(days)$	14.43 ± 2.42	15.52 ± 2.45	7.65 ± 1.31	11.7 ± 1.43	4.14 ± 0.69	7.96 ± 0.95
$T_{duu}(days)$	-	-	-	-	-	22 ± 28.7
$T_{dvv}(days)$	18.92 ± 14.94	26.47 ± 29.96	19.55 ± 50.99	26.39 ± 96.76	6.95 ± 15.12	10.86 ± 1.56
$T_{duu}^{theory}(days)$	126.81 ± 182.19	105.17 ± 162.85	47.61 ± 51.18	557.80 ± 3607.9	17.08 ± 14.89	28.58 ± 47.27
$T_{dvv}^{theory}(days)$	14.78 ± 5.32	18.69 ± 10.61	7.00 ± 1.59	14.50 ± 4.59	5.62 ± 2.14	7.07 ± 3.79
$K_{xx}^o(m^2/s)$	4425.3 ± 751.11	2350.2 ± 376.99	5858.7 ± 1293.6	3104.6 ± 563.3	7487.8 ± 1876.7	8563.2 ± 3406.3
$K_{yy}^o(m^2/s)$	5463.2 ± 1236.4	2773.4 ± 559.9	5027.3 ± 1099.3	2818.2 ± 560.8	7617.6 ± 1907.2	7416.6 ± 2510.1
$K_{xx}(m^2/s)$	4402.4 ± 768.4	1962.4 ± 345.1	5858.6 ± 1293.6	3049.1 ± 572.5	7092.7 ± 2118.9	5433.2 ± 1790
$K_{yy}(m^2/s)$	2132.2 ± 366.9	1391.1 ± 208.2	2821.1 ± 566.3	1496.8 ± 296.7	3475.8 ± 1072.8	3087.9 ± 1085.2
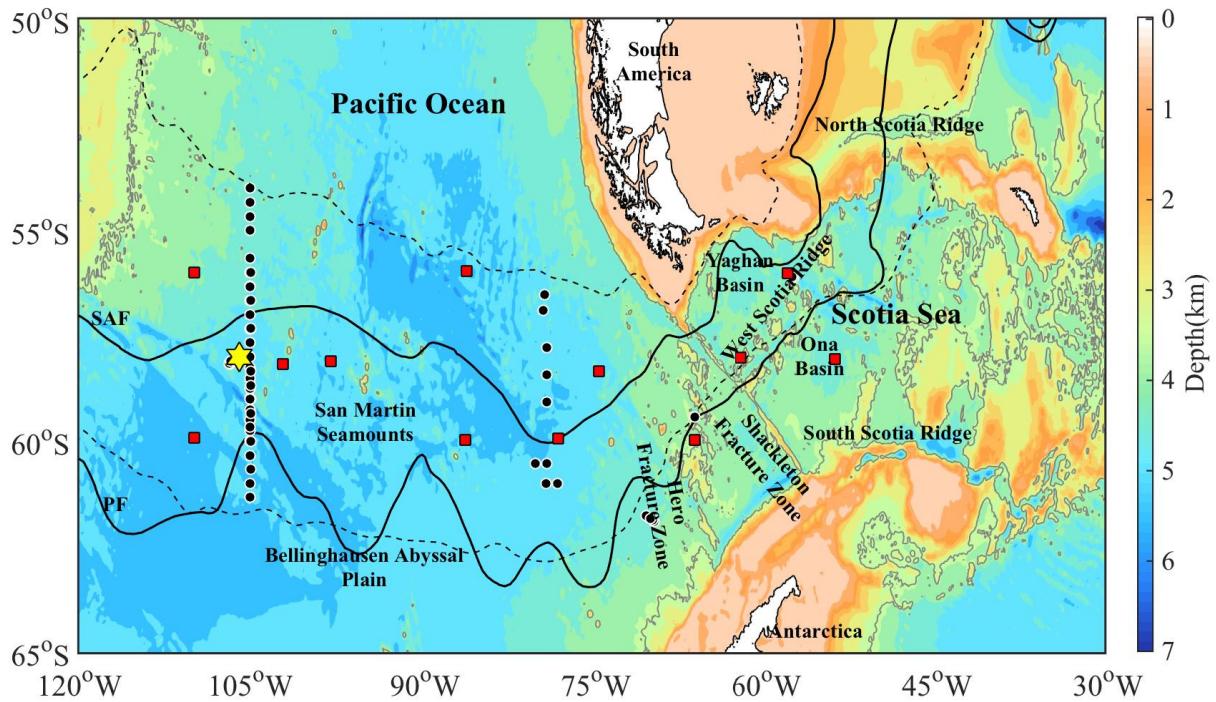
Figure 2.1: Regional geography with the major topographic features (bathymetry colored with contour spacing of 500 m), and experimental components. The 0 m and 3300 m depth contours are displayed in black and gray respectively to highlight the major topographic features. The yellow star is the tracer deployment location, the black dots are the float deployment locations and the red squares are the positions of the sound sources. SSH contours (-60cm and 20cm, dashed), which engulf the initial float deployment locations highlight the position of the ACC through the region. SAF and PF (solid black) from Orsi et al. (1995)
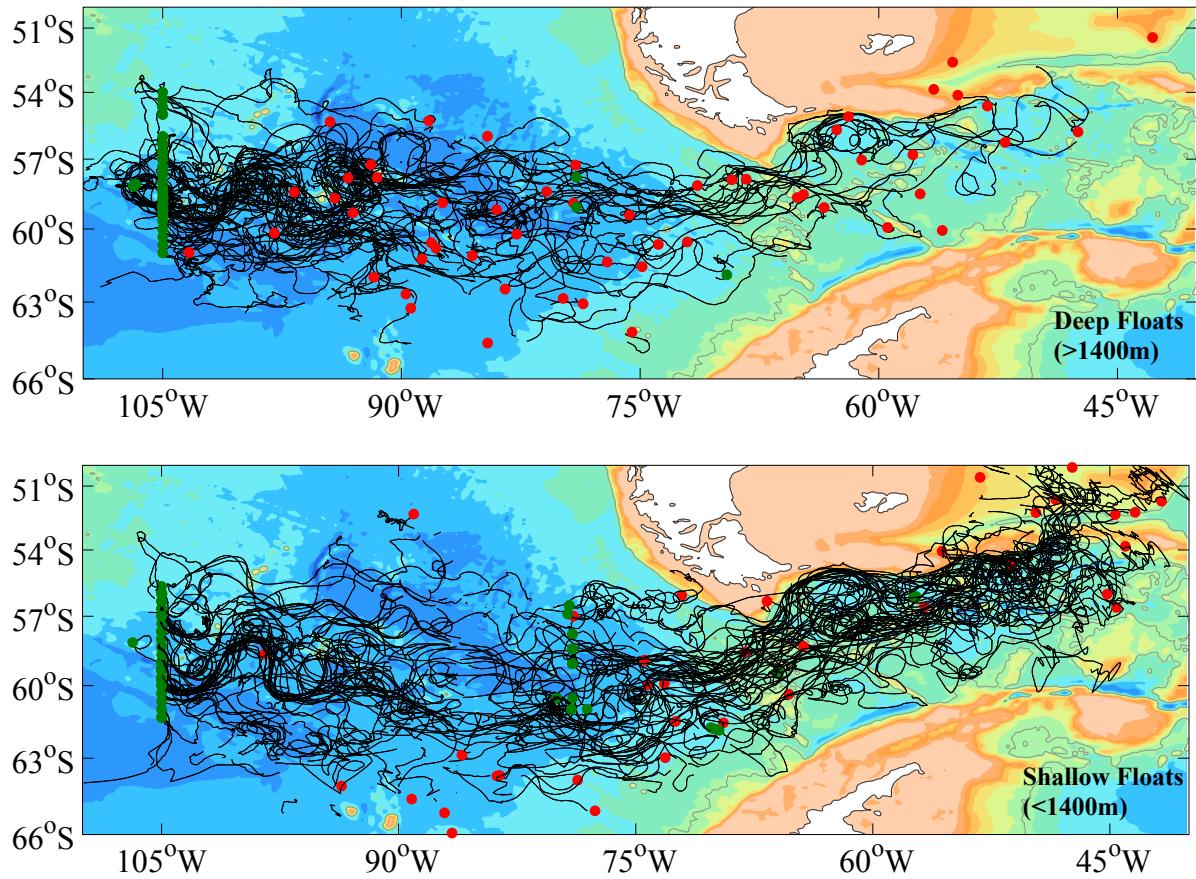
Figure 2.2: Trajectories of the floats with mean depth greater than 1400m (top, 60 tracks) and shallower than 1400m (bottom, 80 tracks). The green dots represent the launch location and the red dots represent the surfacing location.
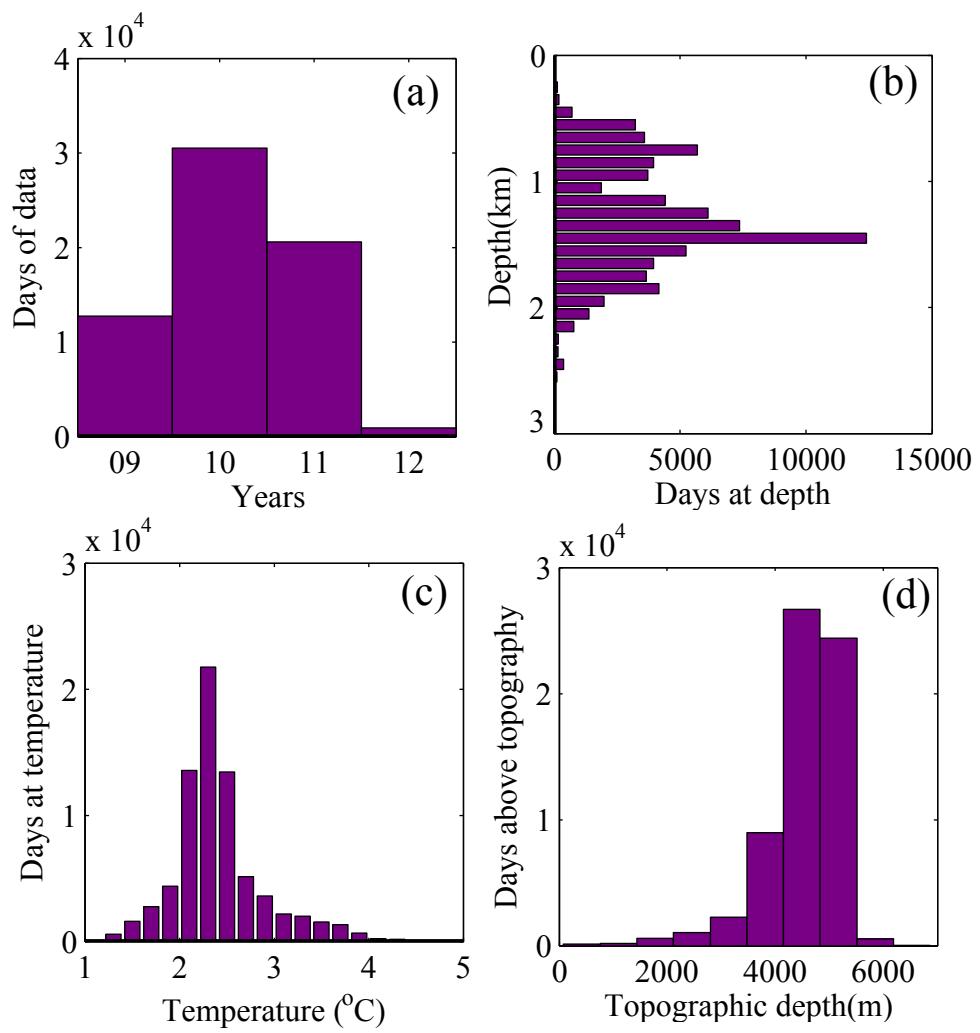
Figure 2.3: Distribution of the total float days as a function of (a) calendar year, (b) pressure, (c) temperature and (d) height above topography.
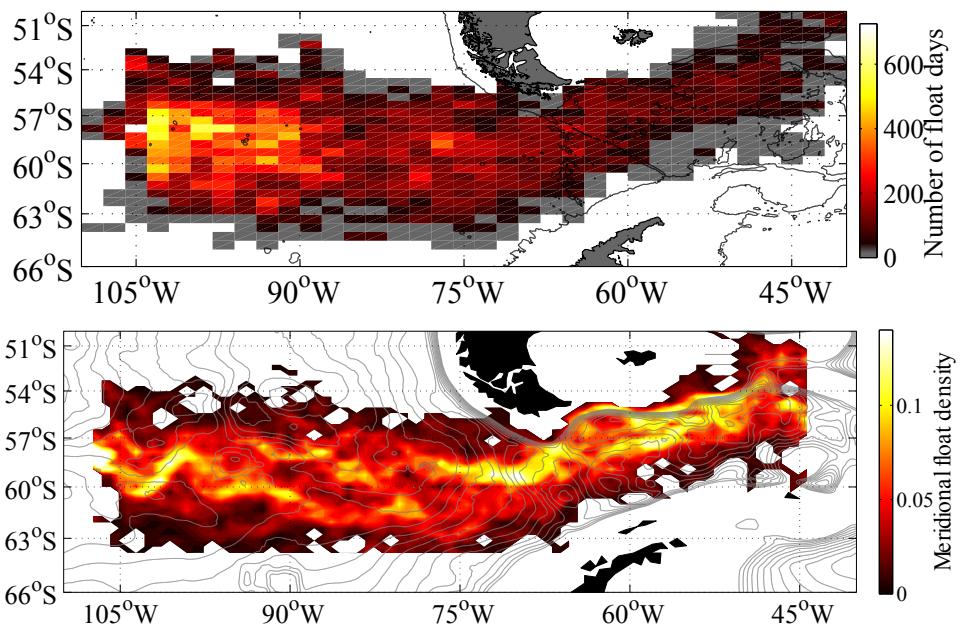
Figure 2.4: Top - Number of float days in $2.0^o X 0.5^o$ bins, chosen to be the same as the bin size used for calculating horizontal structure of mean flow. Bottom - A contour map of number of floats that cross through a meridional bin normalized by the total number of floats that cross through the corresponding meridian. Barotropic PV (f/H) contours are overlaid (gray) with f the Coriolis parameter and H the bathymetric depth
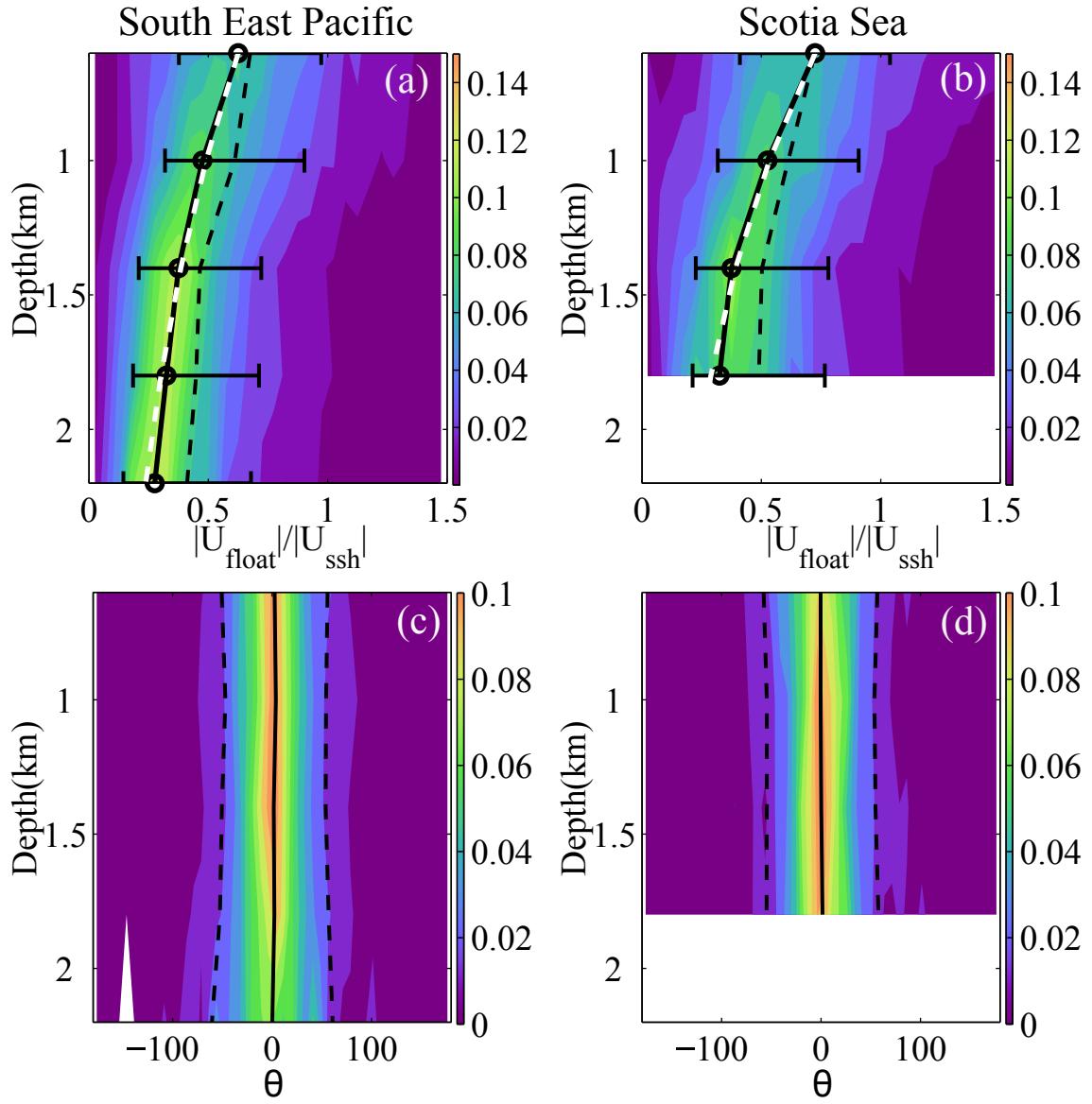
Figure 2.5: Geostrophic velocities, calculated using SSH, compared with velocities from the floats. Probability distribution functions of ratio of float speed versus SSH derived speed plotted versus depth for (a) Southeast Pacific Ocean and (b) Scotia Sea respectively. Mode (solid lines), and mean (dashed lines) are given, error-bars represent one standard deviation; exponential fits (white lines) with depth scale of 1300m in the Scotia Sea and 1650m in the Southeast Pacific Ocean. Probability distribution function of the angle between SSH derived velocity and float velocity as a function of depth for (c) the Southeast Pacific Ocean and (d) Scotia Sea respectively; mean (solid) and one standard deviation (dashed).
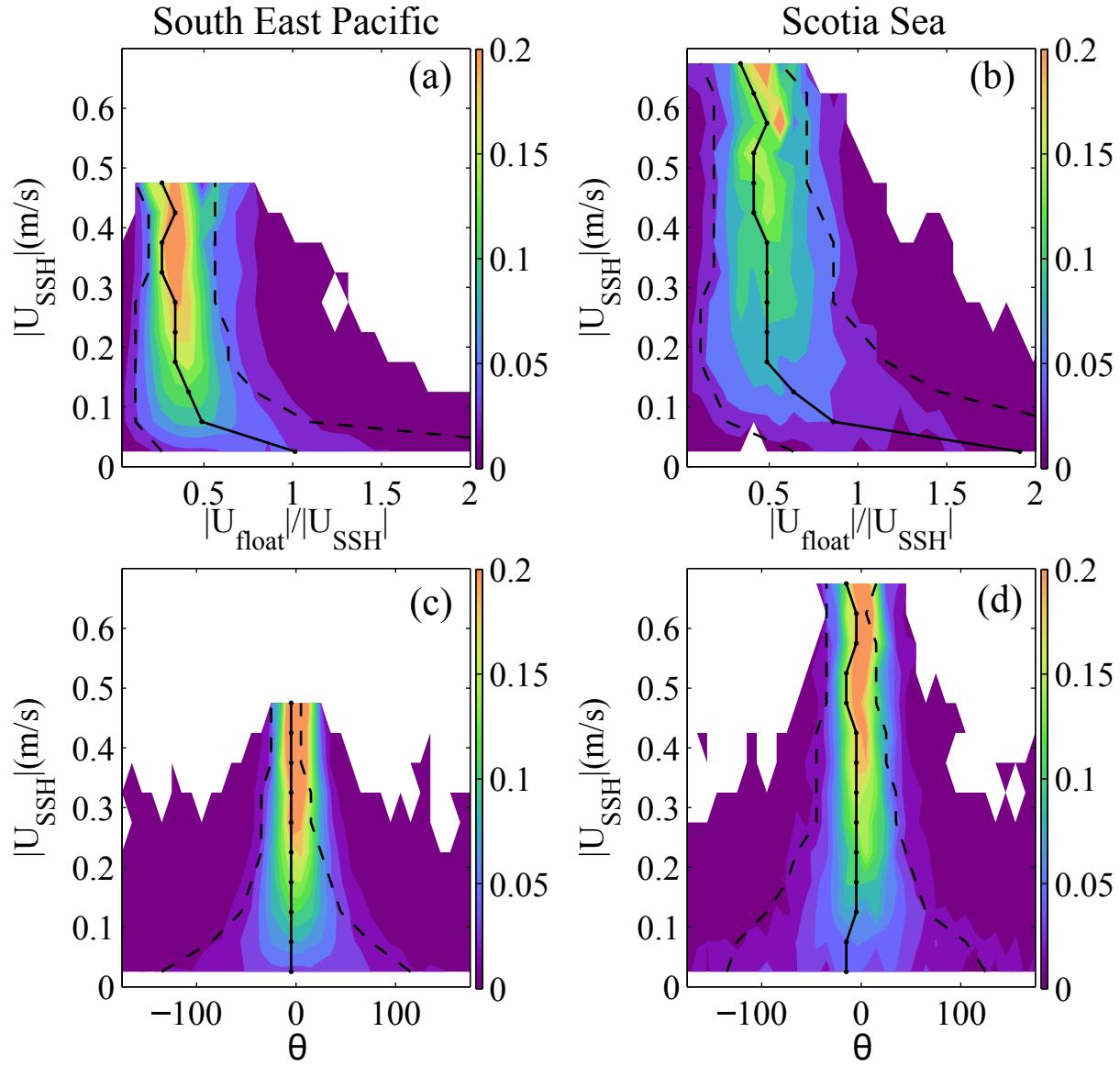
Figure 2.6: Probability distribution function of the ratio of float speed to SSH derived geostrophic speed binned in surface speed bins for (a) the Southeast Pacific Ocean and (b) Scotia Sea respectively. Probability distribution function of angle between SSH derived velocity and float velocity binned in surface speed bins for (c) Southeast Pacific Ocean and (d) Scotia Sea respectively; mean (solid) and one standard deviation (dashed).
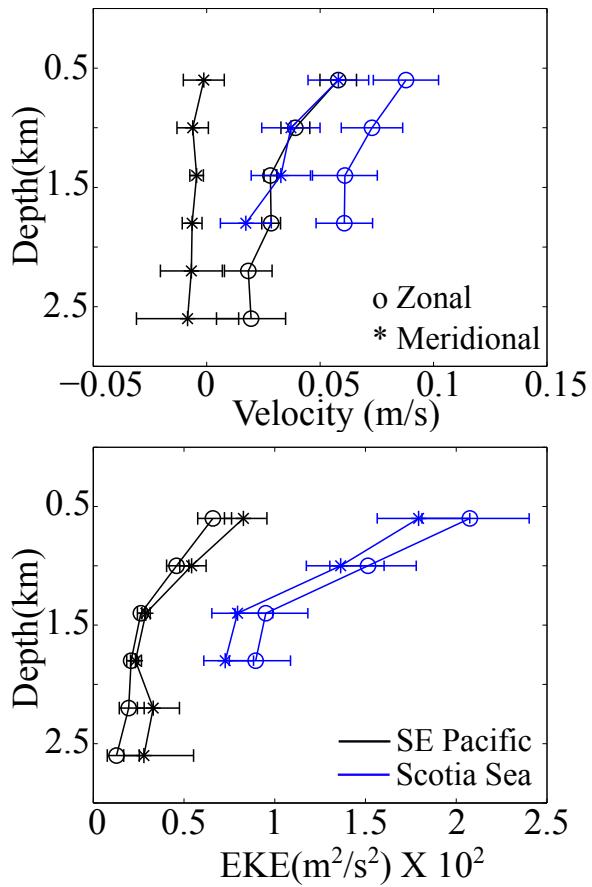
Figure 2.7: Top - Vertical structure of mean velocity in the Southeast Pacific Ocean (black) and Scotia Sea (blue). Bottom - EKE in the Southeast Pacific Ocean (black) and Scotia Sea (blue) binned in depth level bins. 'o' and '*' represent the zonal and meridional components respectively.
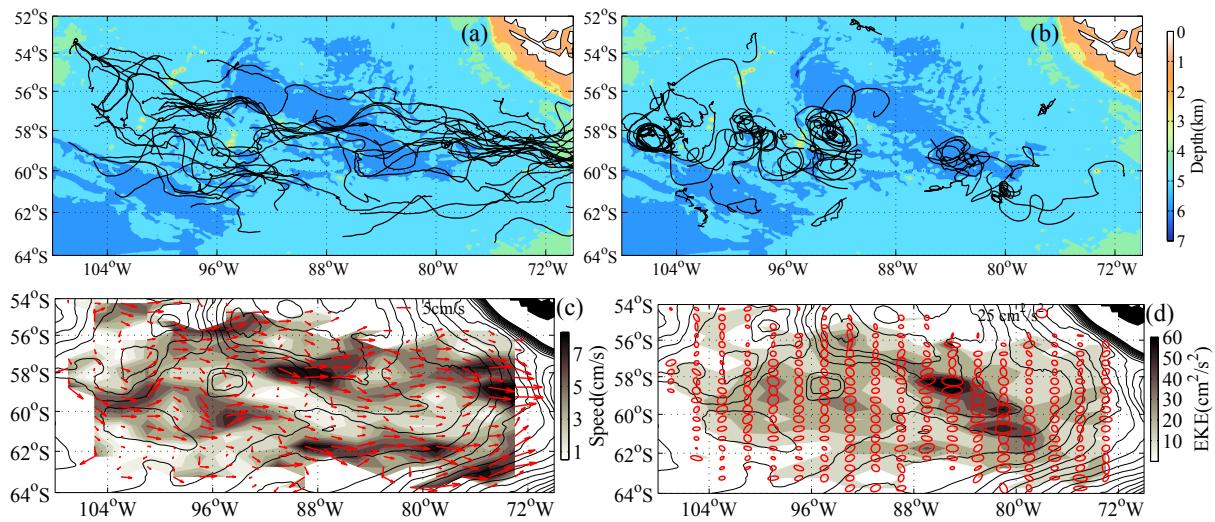
Figure 2.8: Top - Float tracks in the Southeast Pacific Ocean, showing straight (a) and looping (b) tracks. Depth is contoured in color. Bottom - binned Eulerian fields for the Southeast Pacific Ocean. (c) Arrows indicate direction, mean speed is shaded. (d) EKE along with standard deviation ellipses. Barotropic PV (f/H) contours are shown (solid lines).
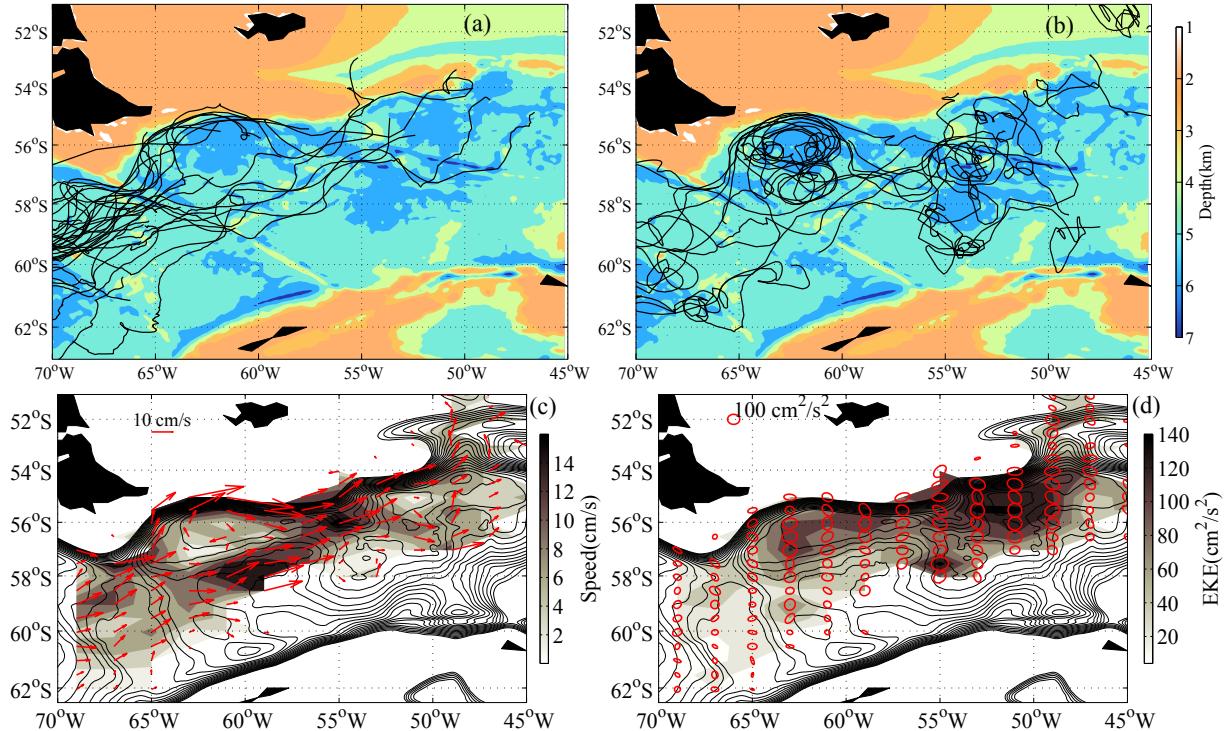
Figure 2.9: Top - Floats tracks in the Scotia Sea, showing straight (a) and looping (b) tracks. Depth is contoured in color. Bottom - binned Eulerian fields for the Scotia Sea. (c) Arrows indicate direction, mean speed is shaded. (d) EKE along with standard deviation ellipses. Barotropic PV (f/H) contours are shown (solid lines).
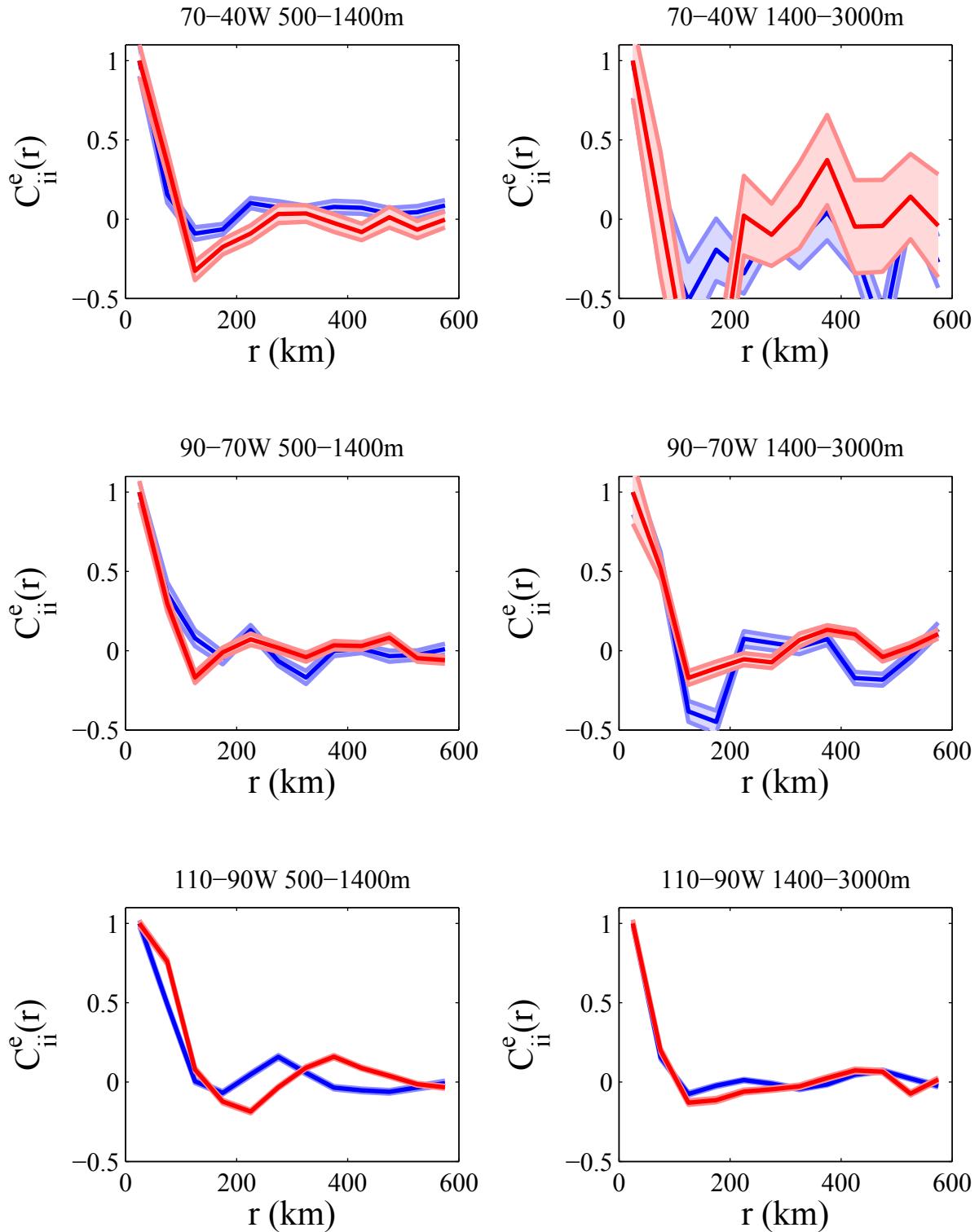
Figure 2.10: Quasi-Eulerian spatial correlation functions calculated from floats. Zonal - C_{uu}^e are in blue and Meridional - C_{vv}^e are in red. Errorbars are standard errors in each distance bin.
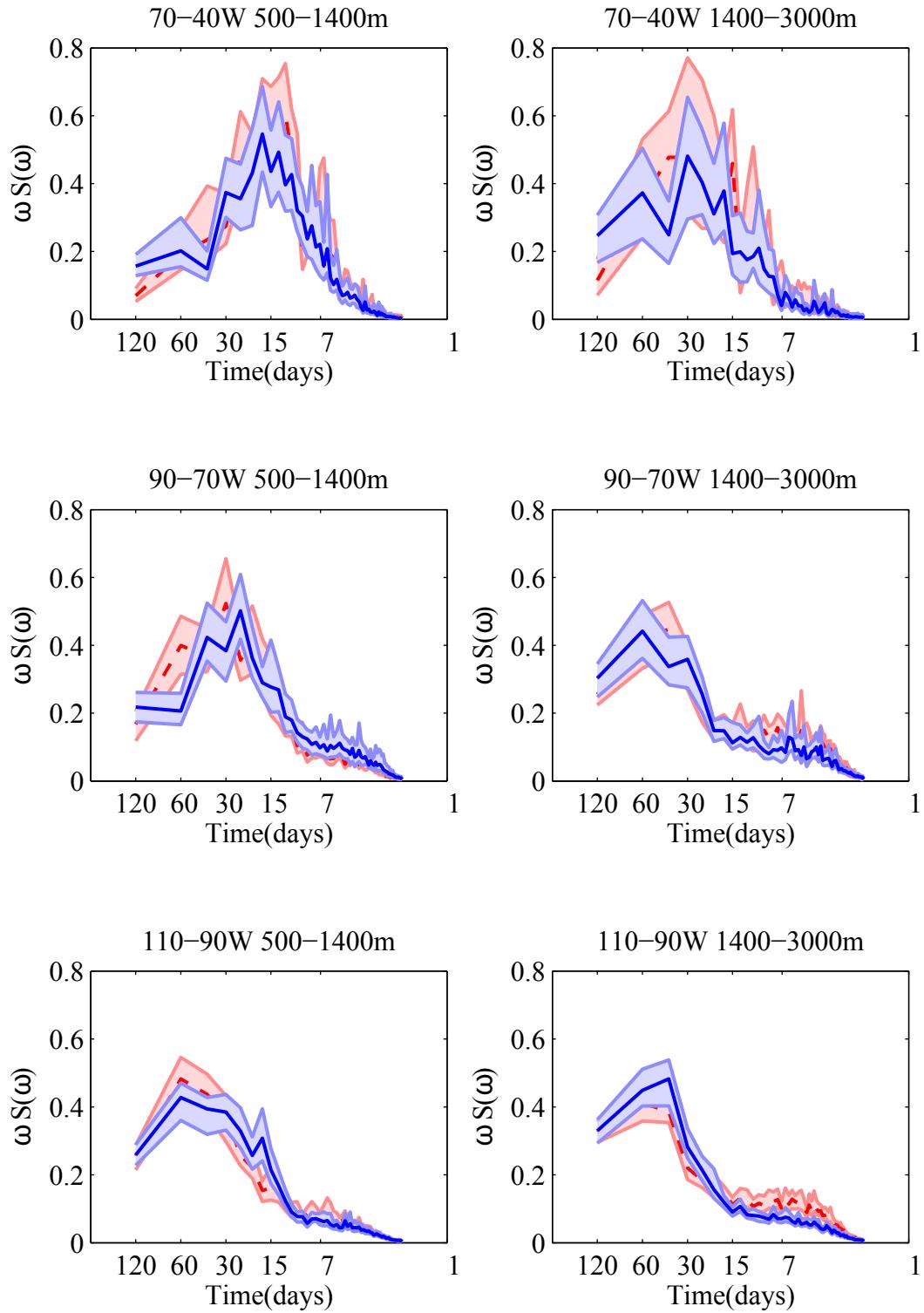
Figure 2.11: Variance preserving normalized Lagrangian spectra from float velocity. Zonal velocity (blue) and meridional velocity (red). Errorbars are obtained by bootstrapping and shown as lighter color shading.
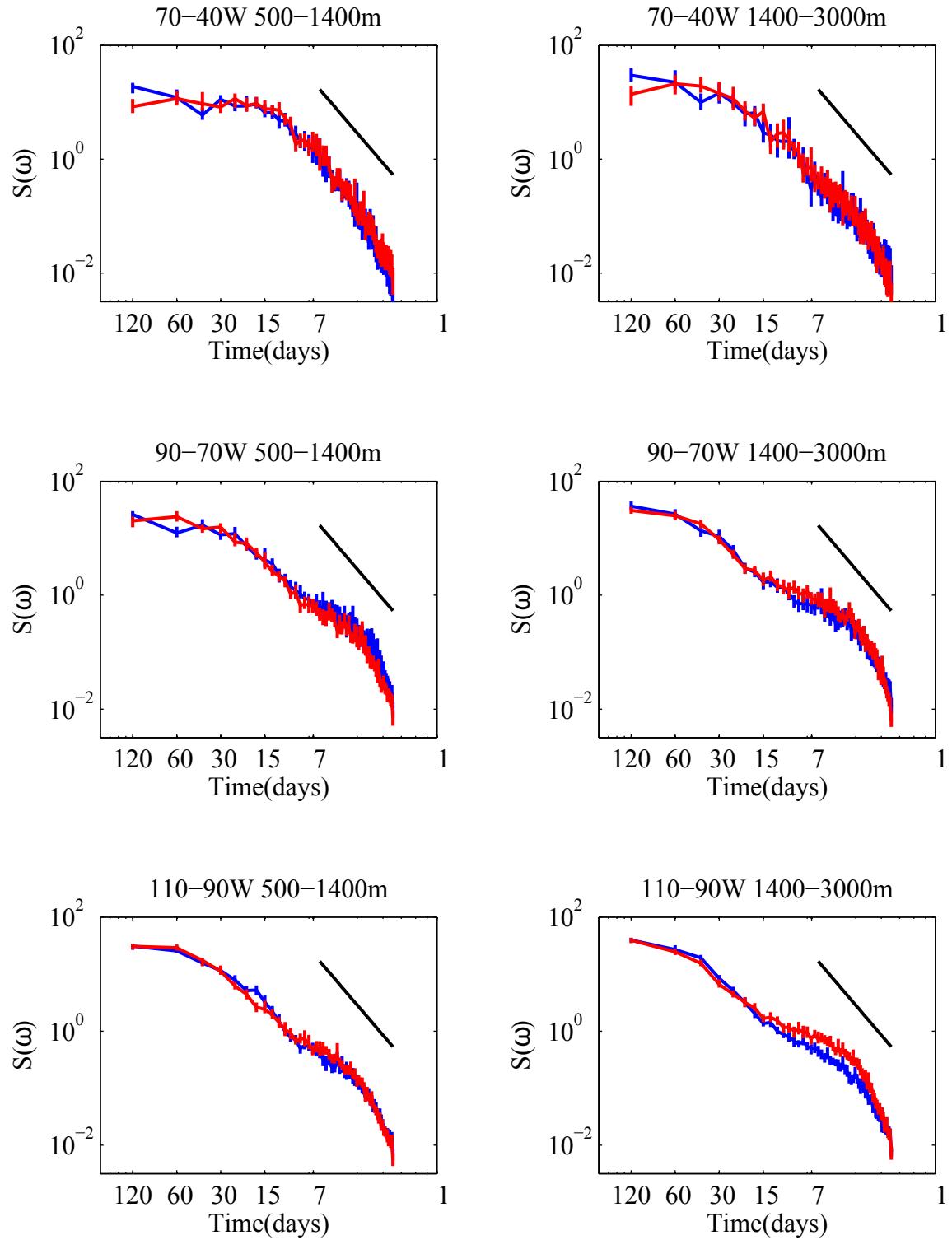
Figure 2.12: Lagrangian spectra on a log-log plot. Zonal velocity (blue) and meridional velocity (red). The black line represents a slope of -3. Errorbars are obtained by bootstrapping and are shown as small lines extending over the limits of the errors.

44
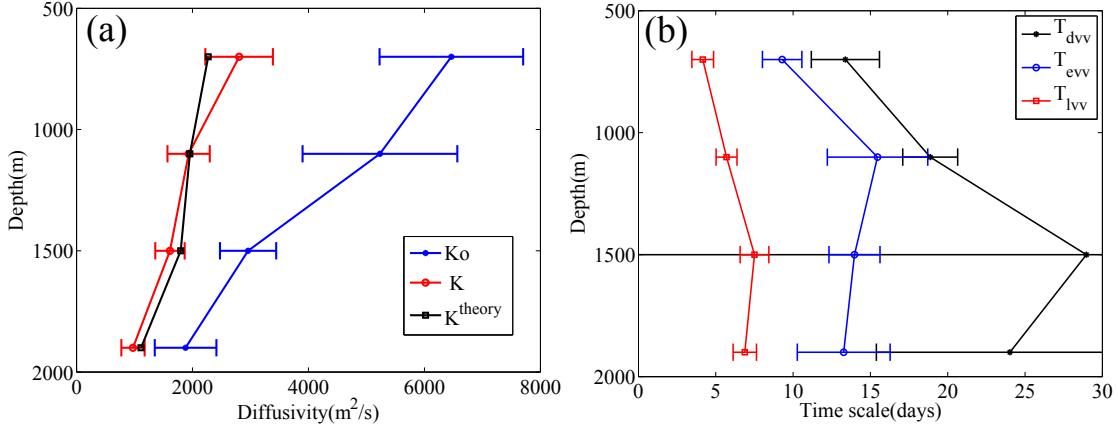
Figure 2.13: (a) Vertical structure of meridional diffusivity in the Southeast Pacific Ocean. The diffusivity scale $Ko = EKE.T_{evv}$ (blue) is calculated using only the decay time scale from the floats, the estimated value $K = EKE.T_{vv}^{l}$ (red) is calculated using the full Lagrangian time scale from the floats and the value $K^{theory} = \frac{4EKET_{eii}T_{dii}^{theory2}}{\pi^2 T_{eii}^2 + 4T_{dii}^{theory2}}$ (black) is calculated using the decay time scale from the floats and meander time scale from theory, which assumed a length scale of 100km. (b) Vertical structure of time scales in the Southeast Pacific Ocean, calculated by the fitting the velocity autocorrelation to equation 2.7; T_{dvv} is the first zero crossing and T_{evv} is the decay scale in the meridional direction. T_{lvv} is the Lagrangian time scale using equation 2.8 in the meridional direction. T_{dvv} has very large error bars at 1500m because the autocorrelation decays quickly without a prominent negative lobe.
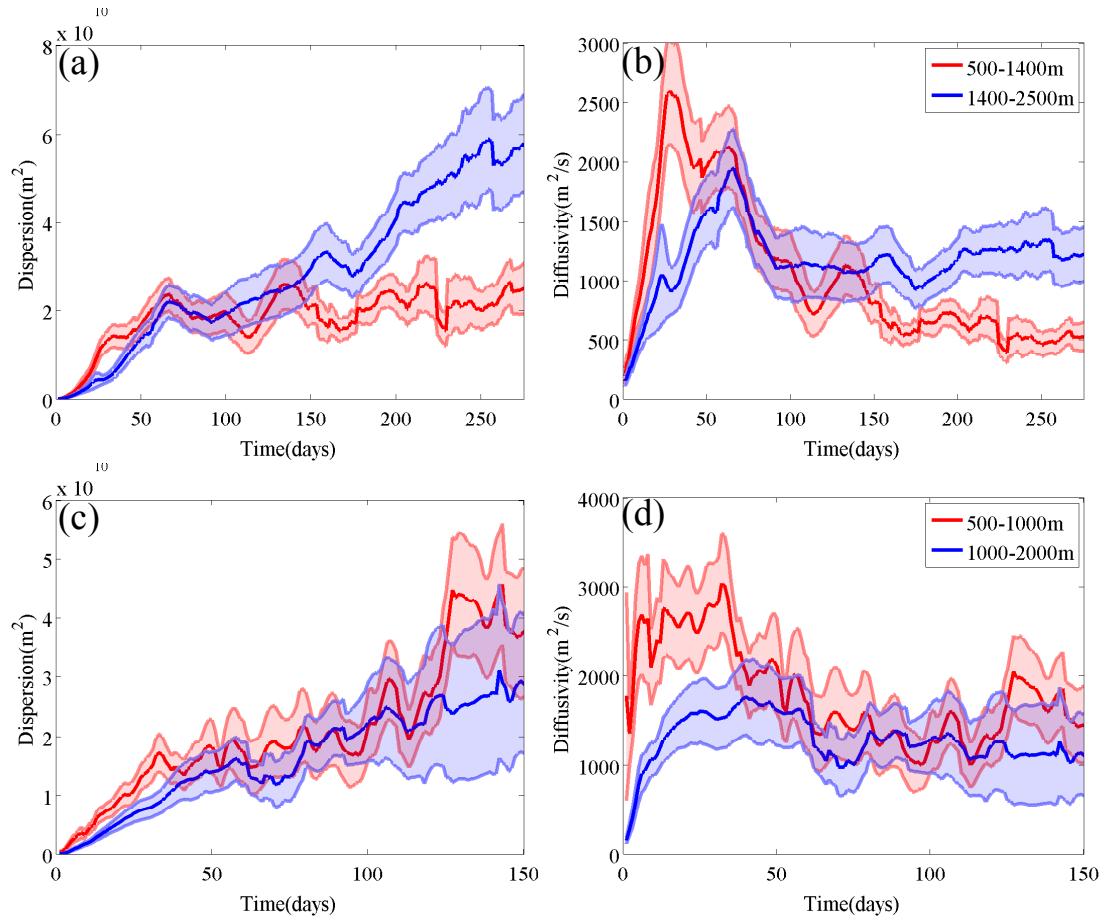
Figure 2.14: Dispersion (a) and diffusivity (b) for the floats launched west of 100^oW in the Southeast Pacific Ocean divided into vertical bins encompassing 500-1400m and 1400-2500m. Dispersion (c) and diffusivity (d) for the floats that crossed 70^oW into the Scotia Sea and divided into vertical bins encompassing 500-1000 m and 1000-2500 m.

CHAPTER 3

EDDY-DRIVEN MERIDIONAL TRANSPORT ACROSS THE ANTARCTIC CIRCUMPOLAR CURRENT

3.1   Introduction

The Southern Ocean plays a key role in closing the global circuit of the Meridional Overturning Circulation (MOC) by connecting the different ocean basins, and by providing an adiabatic pathway for the deep water to return to the surface. Both these roles are facilitated by the presence of the Antarctic Circumpolar Current (ACC). The ACC transports and exchanges approximately 140 Sv water between ocean basins, advectively mixing water masses between ocean basins. Additionally, its presence causes the isopycnals to rise approximately 1000 m across the width of the current, providing the adiabatic return path for deep water to return back to the surface. The density of this deep water, which returned to the surface adiabatically, can be transformed by the action of winds and surface buoyancy fluxes, without having to rely on the small diapycnal diffusivities in the interior (Ledwell et al. (1998), recent reviews can be found in Marshall and Speer (2012); Rintoul and Garabato (2013)).

The zonally unblocked latitude bands, open channel, in the Drake Passage ($\sim 55 - 62^o$S) has a unique effect on the dynamics of the flow in the Southern Ocean. Firstly, under the action of appropriate wind and bouyancy forcing a zonal flow, the ACC, can form and be sustained, which as discussed above plays a key role in the MOC. Secondly, due to the lack of zonal barriers, no zonal pressure gradients or mean geostrophic meridional flows across the zonal channel are possible. Thus, all the meridional flow across the zonal channel, atleast at depths above the shallowest submarine topography, can only be a result of eddies. At depths greater than the sill depth of 2000m, resulting primarily from the presence of the Kerguelan Plateau and Shackleton Fracture Zone, zonal pressure gradients and mean geostrophic meridional flows, in the form of gyres and deep western boundary currents, can be sustained (Nadeau and Ferrari (2015))

The role of the eddies and wind driven mean flows in the zonal channel, and their influence and connection to the global MOC, can be understood using the perspective of a zonal averaging (Nikurashin and Vallis (2012)). The zonally averaged overturning stream function ($\psi_{ov}(y,z)$, where (y,z) implies dependence in the latitude - depth plane) in the channel is a sum of a wind driven overturning stream function ($\bar{\psi} = -\tau/(\rho_o f)$, where $\tau(y)$ is the wind stress, ρ_o is a reference density, and $f(y)$ is the Coriollis frequency.) and an eddy driven overturning stream function ($\psi^* = -K_e \frac{\partial_y b}{\partial_z b}$, where K_e is the eddy diffusivity and b is the buoyancy), considering the dynamics in the channel to adiabatic. At the surface the northward volume transport ($v_e h_e$, where $v_e = -\partial \bar{\psi}/\partial z$ is the velocity in the Ekman layer and h_e is the Ekman layer depth) corresponding to the wind stress (Ekman flow), is partially cancelled by the eddy driven flow to to the south. The net volume flux crossing mean isopycnal outcrops has to be balanced by appropriate surface buoyancy fluxes in a steady state (Marshall and Radko (2003)). This net cross isopycnal flow of water masses at the surface has to be supported by upwelling or downwelling of water from the interior (away from the surface), which can only be sustained by meridional eddy driven transport ($v^* h$, $v^* = -\partial \psi^*/\partial z$ is eddy driven velocity and h is the isopycnal thickness) in the zonal channel. In a steady state the overturning stream function in the channel ($\psi_{ov} = \bar{\psi} + \psi^*$) has to equal the overturning stream function in the ocean basins to the north (ψ_I), closing the circuit of the MOC. ψ_I is a net result of the volume flux resulting from the dense water formation at the northern high latitudes and the additional volume fluxes to individual isopycnals by diapycnal processes.

An interesting ideal scenario, considered by Henning and Vallis (2005), helps in illustrating the role of the eddy driven flows as more than merely a component of a volume budget .If the eddy driven flow in the channel is small, imagine an ideal ocean that lacks baroclinic instability and eddies, then the wind driven contribution must balance the volume flux from the ocean basins ($\psi_{ov} = \bar{\psi} = \psi_I$). As no eddies are present to generate a southward flow in the interior, to balance the northward Ekman transport at the surface, all the southward transport below the surface happens in a bottom boundary layer or below the sill depth. The isopycnals and overturning streamlines become vertical in the unblocked channel, and water transported southward at depth is sucked to the surface via Ekman suction. This scenario is not realized in the real ocean due to the ubiquitous presence of eddies in the ACC, but helps to reveal the importance of eddies in influencing the observed stratification.

It is challenging to quantify the eddy transport, for both observations and models, due to the small spatial scales ($<$ 100 km), inhomogeneity and intermittency of eddies. Previous studies investigating eddy process, using observations(Sallée et al. (2011); Naveira Garabato et al. (2011)) or models (Lu and Speer (2010); Abernathey et al. (2010)), have generally focussed on quantifying the eddy stirring, usually in terms of an eddy diffusivity. Their results have revealed eddy stirring hot-spots downstream of topographic features in the ACC, but have not quantified the associated transport. Also, most of the observational estimates have been representative of the surface ocean, as they are derived from surface drifters or altimetry fields (Sallée et al. (2011); Shuckburgh et al. (2009). To overcome this observational gap, the Diapycnal and Isopycnal Mixing Experiment in the Southern Ocean (DIMES) was designed to provide direct in situ observations of eddy stirring in the mid-depth Southeast Pacific Ocean with the help of passive tracer and Lagrangian float releases.

The aim of this study is to address one of main aims of the DIMES experiment and provide estimates of cross ACC eddy transport in the Southern Ocean. To make progress towards this goal we assume that the large scale effect of eddies is to diffuse potential vorticity (PV) down gradient. This leads to a diffusive parameterization of eddy transport that requires estimates of eddy diffusivity and large scale gradients of PV. To calculate the eddy bolus velocity, under the purview of this parameterization, we estimate the PV gradients from a variety of hydrographic observations and use estimates of eddy diffusivity that resulted from the DIMES experiment and two later analysis studies that used the Argo array.

3.2   Methods and Data

3.2.1   Transport Framework

First we provide a more rigorous and detailed explanation of the transport framework, which was briefly introduced earlier. We start with the zonal momentum equation in an isopycnal coordinate system for a Boussinesq and hydrostatic fluid,

$$u_t - v(\zeta + f) = -\frac{1}{\rho_o}B_x + F^x. \tag{3.1}$$

Here u, v are the zonal and meridional velocities, $\zeta = v_x - u_y$ is the relative vorticity, F^x represents the zonal forcing (wind, friction, diabatic effects) and $B = p + \rho g z + \frac{u^2 + v^2}{2}$ is the

Bernoulli function. p is the dynamic pressure and ρ is the density perturbation in the definition of the Bernoulli function.

Time averaging equation 1, for a statistically steady steady flow ($\overline{u}_t = 0$) and at length scales where planetary geostrophy holds ($f > \zeta$ and $B/\rho_o \approx M$, where M is the Montgomery potential), leads to an equation for the mean transport,

$$\overline{vh} = \bar{v}\bar{h} + \overline{v'h'} = \frac{1}{\overline{q}^*}(\overline{M}_x - \overline{F^x} - \overline{h}.\widehat{\hat{v}\hat{q}}^*). \tag{3.2}$$

Here $h = \partial z/\partial \rho$ is the layer thickness, z is the layer depth, $\overline{(.)}^* = \frac{\overline{(.h)}}{\overline{h}}$ is the thickness weighted mean, and $\hat{(.)}$ is the deviation from this mean. $\overline{(.)}$ implies a time average and $\overline{q}^* = \overline{q} = f/\overline{h}$.

The mean flow ($f\overline{v} = \overline{M}_x - \overline{F^x}$) is driven by gradients of the Montgomery function, which plays the role of pressure in isopycnal coordinate, and the forcing (Ekman flows at boudaries and diabatic processes in the interior). The mean transport has contributions from not only from the mean flow, but also due to the eddy bolus velocity ($v^*\overline{h} = \overline{v'h'} = -\frac{1}{\overline{q}^*}\overline{h\hat{v}\hat{q}}^*$).

Before we proceed to a discussion of how to observationally estimate the eddy bolus velocity, a discussion of two important integral results for the mean flow is warranted. The integral of the mean velocity ($\oint \bar{v}ds$) is zero on any closed contour along which the net forcing term is negligible, such as along a zonally unblocked latitude circle in the interior of the ocean. However, the integral of the transport driven by the mean flow ($\oint \bar{v}\bar{h}ds$) is zero only when the closed integrating path is a constant PV contour (Zika et al. (2009)). The subtle implication of this integral statement is that the circumpolarly integrated transport driven by the mean geostrophic flow across the ACC is only zero in the layers that have circumpolarly closed PV contours. Thus a transport driven by the mean geostrophic flow can be sustained in isopycnal layers that are shallower than the sill depth. This geostrophic transport was neglected while discussing the zonally averaged 2D framework, primarily to maintain simplicity and also because depth was chosen as the vertical coordinate rather than isopycnals. Mazloff et al. (2013) showed that this mean geostrophic flow was not negligible, and had the same pattern but opposite sign to the eddy driven flow. Thus, the 2D stream function framework, when considered in isopycnal coordinates, can be corrected by noting that $\bar{\psi}(y, \gamma)$ is a combination of mean geostrophic flow, due to PV contours not necessarily being closed in all isopycnals present above the sill depth, and the wind driven Ekman flow.

The eddy bolus velocity is driven by the eddy PV fluxes ($v^*\bar{h} = \overline{v'h'} = -\frac{1}{\bar{q}^*}\overline{h\hat{v}\hat{q}}^*$), and suggests that a paramaterization of the eddy PV flux will be the appropriate parameterization of the eddy bolus velocity. As PV satisfies a tracer transport equation, it is reasonable to parameterize the eddy PV fluxes as down gradient diffusion (Vallis (2006)). This can be written as,

$$v^* = \kappa_{PV}\frac{\bar{h}}{f}\frac{\partial\bar{q}}{\partial y} = \kappa_{PV}(\frac{\beta}{f} - \frac{1}{\bar{h}}\frac{\partial\bar{h}}{\partial y}), \quad (3.3)$$

where κ_{PV} is the PV diffusivity and β is the planetary vorticity gradient. Thus the bolus velocity has contributions from the thickness gradients and the planetary vorticity gradients.

An alternate parameterization of the bolus velocity can be derived based on the energy cycle of baroclinic instability (Gent and Mcwilliams (1990)) and leads to the expression,

$$v^* = -\frac{1}{\bar{h}}\frac{\partial}{\partial\rho}\kappa_{GM}\frac{\partial\bar{z}}{\partial y}, \quad (3.4)$$

where κ_{GM} is the GM diffusivity and $\bar{z}$ is the mean isopycnal depth. The two diffusivities would be the same only if the planetary vorticity gradient is negligible and $\partial\kappa_{GM}/\partial\rho = 0$, which is not necessarily true.

Both these parameterizations of v^* require knowledge of the large scale mean structure of the isopycnals and the eddy diffusivities. The mean isopycnal structure in the ocean can be obtained from a hydrographic climatology. The PV diffusivity is similar to the tracer diffusivity that is measured by a passive tracer or floats in the interior (Abernathey et al. (2013)). Thus, diffusivity estimates from observations will be assumed to be the same as the PV diffusivity.

As GM diffusivity is the most commonly used parameterization in numerical models we will invert equation 4 for κ_{GM}, using the v^* estimates from the PV diffusivity parameterization. Observational estimates of κ_{GM} are not the same as tracer diffusivity estimates in the interior, but are instead related to diffusivity of buoyancy. To get observational estimations the κ_{GM} one needs to know the eddy fluxes of buoyancy, which can only be measured by current meters and are available only at a few locations.

As the eddy activity varies zonally, regions of high and low eddy energy exist along the path of the ACC, a 3D extension of streamfunction framework introduced in the introduction is useful. In a 3D extension ($\psi_{ov}(x,y,\gamma)$, where (x,y,γ) implies dependence in the longitude-latitude-isopycnal space), the zonal convergence or divergence additionally effects the local overturning budgets ($\psi_{ov} =$

$\psi_I = \bar{\psi} + \psi^* + \psi_z$, where ψ_z is the zonal convergence, Thompson et al. (2016)). The zonal variations of the wind driven component are small, as the wind stress is zonally uniform to first order. Thus the variability of eddy energy, and thus the eddy driven transport, must either produce a corresponding convergence of divergence of the mean zonal flow, or lead to variations in the local overturning streamfunction.

3.2.2 Observations

Eddy Diffusivities. Eddy diffusivity in a tracer equation can be defined in a variety of complementary ways. Such as,

$$
\begin{aligned}
\kappa &= \frac{1}{2}\frac{d\overline{X^2}}{dt} \\
&= \frac{1}{2}\frac{d\sigma^2}{dt} \\
&= \Gamma_1 u L_{mix} \\
&= \Gamma_2 u^2 T_{mix},
\end{aligned}
\tag{3.5}
$$

where X is the particle displacement, u is the eddy velocity, σ is the second moment of tracer concentration, Γ_1, Γ_2 are proportionality coefficients, L_{mix} is the mixing length scale and T_{mix} is the mixing time scale. These four definitions can be termed as the Lagrangian particle diffusivity, passive tracer diffusivity, mixing length diffusivity estimate and mixing time scale diffusivity estimate respectively. All the observational estimates of eddy diffusivity considered here define their eddy diffusivity using one of these definitions.

Tulloch et al. (2014) and Lacasce et al. (2014) calculated the diffusivity using the observations collected during the DIMES experiment in the Southeast Pacific Ocean. Tulloch et al. (2014) used the rate of growth of the second moment of tracer concentration meridionally and along isopycnals as the metric for along isopycnal passive tracer diffusivity. They used the observations of the tracer patch that was released at $\gamma = 27.9$ during DIMES to validate results of a numerical tracer released in a high resolution model. As the modeled and observed tracers compared well at the $\gamma = 27.9$, it was assumed that the model was a suitable representative of the eddy processes in the Southeast Pacific. Numerical tracers released at other isopycnal levels were used to obtain the vertical structure of the tracer diffusivity. Similarly, Lacasce et al. (2014) calculated the vertical structure

of the Lagrangian diffusivity by calculating the rate of dispersion of numerical particles released in the model velocity fields, instead of a tracer. The diffusivity estimates from the numerical particles were validated using the diffusivity from RAFOS floats that were released during DIMES. Balwada et al. (2016b) used the DIMES RAFOS float data and explored the effects of inhomogeneities on the eddy diffusivity in the presence of jets (mixing barriers) and regions of strong mixing between jets. However, the appropriate estimate to be used here are of Lacasce et al. (2014), which average over the entire width of the ACC, as the interest is to estimate the net eddy flux across the ACC and not specifically across the individual fronts. We will refer to the estimate of Tulloch et al. (2014) as κ_T and of Lacasce et al. (2014) as κ_L.

Roach et al. (2016) calculated the Lagrangian diffusivity at 1000m using the trajectories of Argo floats, referred to as κ_R. Argo floats drift at 1000m and profile between the surface and 2000m every 10 days. The position is sampled every 10 days, each time the float surfaces. Roach et al. (2016) calculated the eddy diffusivity using all Argo trajectories south of 45S, data coverage dropped rapidly south of the PF. This is a large spatial average but the diffusivity is strongly influenced by the presence of the ACC, which is the most energetic flow in the domain. Thus we use this diffusivity estimate as a coarse representation of the eddy diffusivity in the ACC at 1000m.

Cole et al. (2015) calculated mixing length scales in the global ocean using spice (passive tracer) anomalies and mean spice gradients along isopycnals. They also utilized the rms eddy velocity estimates from the ECCO model to calculate mixing length estimates of eddy diffusivity, referred to as κ_C. We use this diffusivity estimate to calculate eddy fluxes in the top 2000 m.

Large Scale PV gradients. We estimate the large scale hydrographic properties in the Southern Ocean from a number of different data sets, as enumerated below. The region of the ACC is defined as the region of the ocean between the climatological positions of the SubAntarctic Front (SAF) and the Polar Front (PF). The positions of these fronts are defined using the mean sea surface height (SSH) contours corresponding to -3 cm (SAF) and -60 cm(PF), shown in Figure 3.1. The utility of SSH contours as coarse representations of frontal positions has been discussed by numerous previous studies (e.g. Kim and Orsi (2014)).

We tested two different climatologies to calculate the isopycnal slopes and thickness gradients. The first is the CSIRO Atlas of Regional Seas (CARS, Ridgway et al. (2002)). This climatology is derived from a quality controlled archive of historical subsurface measurements from both research

vessels and autonomous profiling buoys. The product provides mean fields of temperature, salinity, oxygen and other tracers on a $1/2^o$ horizontal grid and 79 vertical levels between the surface and 5500m. The data below 2000m is solely from research vessel based hydrographic sections, which are limited to few geographical locations. The second is the Monthly Isopycnal and Mixed-layer Ocean Climatology (MIMOC, Schmidtko et al. (2013)). This product has the same horizontal resolution of $1/2^o$, 81 vertical levels that span between the surface and 1950m, and only provides temperature and salinity fields. The results presented here are exclusively from the CARS climatology, except for the surface outcropping locations that are from the MIMOC climatology. The results are not overly sensitive to this choice.

The temperature and salinity fields were used to calculate the neutral density (Jackett and McDougall (1997)) at all grid points. The layer thickness was calculated as the height difference between the neutral density layers corresponding to the target density $\pm 0.025\gamma$, essentially a central differencing in isopycnal coordinates. To calculate the lateral gradients we fit a linear 2D surface ($y = a + bx + cy$) to the thickness values in a $5^o X 5^o$ box centered at the grid point, and use b, c as the estimates of the zonal and meridional gradients. This is comparable to doing a 2D running mean filter. These meridional gradients that lie on the grid points within the SAF and PF are meridionally averaged as a representative thickness gradient across the ACC. The zonal gradients are usually an order of magnitude smaller than the meridional gradients of thickness. The planetary vorticity gradient (β) and the Coriollis frequency (f) are simply taken as the meridionally averaged value of in the ACC region.

Additionally, for the Southeast Pacific Ocean, where the DIMES experiment was conducted, we created a separate meridional climatology using 783 historical full-depth CTD profiles between 80°W and 110°W extracted from the Southern Ocean Data Base. These were complemented with additional recent profiles from the CLIVAR Repeat Hydrography program (S04P in 2011, P18 in 2008, AAIW05 and AAIW06 occupied in 2005 and 2006 respectively). The neutral density was calculated for each profile, the profiles were then zonally averaged in SSH bins, and the mean separation between the SSH bins was used to create a depth vs meridional section that is representative of the cross-ACC hydrographic properties for the DIMES region. For this section the average thickness gradient across the ACC was estimated as the slope of a linear fit to the thickness values

between the SAF and PF. The planetary vorticity gradient was calculated as the mean value of β in the ACC latitude range.

The PV gradients estimated by creating our own meridional climatology and doing a single linear fit across the entire width of the ACC, versus using the CARS product, estimating gradients as local 2D linear surfaces and then averaging across the meridional width of the ACC, produce similar results. This gives us confidence in our estimates of the thickness gradients.

3.3 Results

Thickness gradients along isopycnals are an implication of spatial variations of the interior stratification of the ocean. This interior stratification is primarily set by buoyancy fluxes at the ocean surface, and then advected into the interior by the large scale circulation. Dissipative processes in the interior act to modify this structure, but usually act on very slow time scales, and are significant only in regions that have long residence times, such as the North Pacific Ocean. Before discussing the structure of thickness gradients, eddy diffusivities and associated eddy bolus velocity in the ACC, we present a qualitative overview of the global layer thickness on four representative isopycnals (Figure 3.1).

Figure 3.1 a and b show the layer thickness of neutral density 27.1 and 27.4 γ, which belong the density layers termed as the SubAntarctic Mode Water (SAMW) and Antarctic Intermediate Water (AAIW) respectively. SAMW is characterized by low PV water. This is a result of deep mixed layers forming near fronts, which are also the formation sites of this water mass. This can be seen in the Pacific Ocean as thick water columns emanating from the surface, where the 27.1 γ late winter outcrop aligns with the SAF. Presumably these thick water columns is advected into the interior by the subtropical gyre and slowly eroded by eddies in the interior of the gyre. AAIW are characterized by a salinity minimum (Figure 3.2). This is a result of the formation sites lying near the PF that is supplied by fresh water from sea-ice melt. The thickest portion of 27.4 γ is seen to originate in the Southeast Pacific ocean, where the late winter density outcrop is aligned with the PF. These thick columns are subsequently advected along the ACC into the Atlantic ocean and to the north of the SAF. Advection of these thick layer to the northern flank of the ACC helps in setting the cross ACC thickness gradient in this layer.

The Circumpolar Deep Water (CDW) is transformed to both lighter (SAMW, AAIW) and denser (Antarctic Bottom Water, AABW) water classes, primarily to the south of the PF in the polar gyres where these isopycnals outcrops. The CDW is often subdivided into an upper and lower class, with the upper CDW (UCDW) being primarily formed in the North Pacific Ocean by interior diabatic processes over long residence times, and the lower CDW (LCDW) being primarily formed in the Arctic Ocean by deep convection as North Atlantic Deep Water (NADW). 27.75 γ belongs to the UCDW and shows a large dichotomy between the Pacific and Atlantic ocean, with the Pacific Ocean having significantly thicker layers than the Atlantic Ocean (Figure 3.1 c). Two processes can contribute to the formation of these thick layers of the North Pacific. Firstly, as there are no source waters for the UCDW in the north Pacific, all the water mass is imported into the basin from south of the equator. The equator puts strong constraints on the PV of the fluid ($f = 0$), thus density layers need to stretch and thicken, in addition to other contributions to PV changing, in order to cross the equator (Roussenov et al. (2002)). Secondly, the long residence times of the UCDW in the North Pacific can potentially allow the diabatic processes to erode the stratification at these densities. These thick layers are eventually advected southwards in a flow along the eastern Pacific ocean, to be re-injected into the northern side of the ACC, and set the cross ACC thickness gradient, as appears to be the case from Figure 3.1 c. This injection in to the ACC is also apparent in the oxygen minimum at 1.5 km at the SAF between 250 - 300 E longitude (Figure 3.2). The LCDW, represented here by 27.95 γ, is supplied primarily by deep convection in the North Atlantic and Arctic Ocean, which produces thick, salty and oxygen rich deep layers. This low PV water is advected southward in deep western boundary currents and along the eastern side of the South Atlantic basin, seen as thick layers on the western side of Africa, and merge with the ACC in the Atlantic and Indian Ocean. This is seen as a salinity maximum, and a relative high in oxygen, at 2.5km depth along the SAF in the Atlantic and Indian Ocean sector.

Figure 3.3 show the presence of positive thickness gradients, layers thinning to the south, between the SAF and PF in all the density layers. The density layers that extend south the ACC, show that the strongest thickness gradients are present south of the ACC, where the isopycnal layers are closest to the surface. In the calculations below we consider the mean value of the gradient between the SAF and PF as representative of the PV gradients across the ACC.

The meridionally averaged thickness gradients normalized by the layer thickness (Figure 3.4 a) are positive, thicker layers to the north of the ACC, between 27.3 and 27.95 γ. This will imply to a southward eddy bolus flux, which is in accordance with the expectation that these layers are losing volume to the south of the PF, and thus demand a southward flux of volume across the ACC. The deeper layers (> 27.95) show a negative thickness gradient, thicker layers to the south of the ACC, as they are supplied by AABW from its formation sites around the Antarctic margins. The thickness normalized thickness gradients ($-1/h\, \partial h/\partial y$) generally decrease with depth, and show zonal variations that appear to be associated with locations of topographic features. These zonal variations can be explained by the convergence of ACC streamlines as it traverses over topography. As the contours of constant thickness are approximately aligned with streamlines, due to the along stream homogenization in the ACC, the convergence of streamlines enhances the meridional gradients of thickness. These order of magnitude zonal variations in the thickness gradients, even though obvious, seem to have been not discussed previously in the literature. The planetary PV gradients are smaller than the thickness normalized thickness gradients and vary as the ACC crosses latitude bands north and south on its excursion around Antarctica (Figure 3.4 b).

Figure 3.5 shows plots of the different diffusivity estimates used here. The diffusivity estimates (κ_L, κ_T) in the Southeast Pacific, calculated in the DIMES studies, reveal a peak diffusivity of 1000 m^2/s centered at about 28.05 γ. There are some minor differences between κ_L and κ_T, probably attributable to differences in methodology, but the overall structure is very similar. The diffusivity estimates (κ_R) at 1000m from Argo float float trajectories vary between 400 - 2500 m^2/s, peaking downstream of topographic features. The mixing length diffusivity (κ_C) from Argo float profiles varies between 500 - 3500 m^2/s and peaks downstream of topography, similar to the Lagrangian diffusivity (κ_R) from Argo floats. κ_C and κ_R broadly agree with each other and the DIMES diffusivities (κ_L, κ_T), and the minor differences can be explained by the differences in spatial averaging and methodology of the different estimates.

The eddy driven bolus velocity in the Southeast Pacific is southward and approximately $1 - 2 \times 10^{-4}$ m/s in 27.4 - 28.1 γ range (CDW) (Figure 3.6 b). The main contribution comes from the term associated with the thickness gradients ($-\kappa \frac{1}{h} \frac{\partial h}{\partial y}$), but some layers with weak thickness gradients show equal contribution from the terms associated with the thickness and planetary PV gradients ($\kappa \beta/f$). In the deepest layers the two contributions oppose each other and lead to a net

northward eddy bolus velocity of approximately 2×10^{-4} m/s. The difference in the bolus velocity calculated from κ_L and κ_T are minor, and in accordance with the differences in diffusivities.

To calculate the v^* associated with κ_R, we use the PV gradients from layer 27.8 γ as this layer lies at a mean depth of 1000 m in between the SAF and PF. The v^* at 1000 m vary zonally by approximately an order of magnitude, peaking in relation with topographic features (Figure 3.6). Similar to the regional results from the Southeast Pacific, the contribution of the term corresponding to the thickness gradient dominates the term corresponding to the planetary PV gradient. The v^* at 1000 m (27.8 γ) in the Southeast Pacific using κ_R is slightly greater than the regional estimates from the DIMES diffusivities.

The v^* corresponding to κ_C is shown in Figure 3.6 c, and shows variations approximately on two order of magnitude ($10^{-4} - 10^{-2}$). This v^* decreases at denser layers, in accordance with the vertical structure of PV gradients. The zonal structure is controlled by the structure of both, the diffusivity and the PV gradient. As we have a complete longitude vs density estimate of v^*, we can zonally integrate this get an estimate of the net meridional volume transport across the ACC in each density layer (Figure 3.6 d). The meridional eddy transport corresponding to individual density layers ($d\rho = 0.05$) decreases from 5 Sv to approximately 2.5 Sv with depth. This would imply a southward meridional eddy transport of 25 Sv in the CDW range (27.5 - 28 γ).

Aside on the GM diffusivity

Finally, we use the v^* estimates in the Southeast Pacific from the DIMES diffusivities to calculate κ_{GM} by integrating equation 4. As we do not know a boundary condition to use for κ_{GM}, we varied the κ_{GM} at 27.4 γ from 0 to 1250 m^2/s. The structure of κ_{GM} varies slowly in the vertical, compared to κ_T or κ_L.

The profile of κ_{GM} has a different vertical structure than the κ_{PV}. κ_{GM} has no mid-depth maxima and just slightly increases with depth. This difference, which is a result of the mathematical structure of equation 4, in the vertical structure is the same as the one obtained by Smith and Marshall (2009) and Abernathey and Marshall (2013) from numerical simulations. This result can be used to validate the κ_{GM} used in general circulation models, provided that the boundary condition on κ_{GM} is known.

3.4   Discussion and Conclusions

We calculated the eddy bolus velocity across the ACC, defined as the region between the SAF and PF, in the Southern Ocean. This was done assuming that the eddy bolus velocity, which is related to the the PV eddy fluxes, can be parameterized as a down gradient diffusion of PV. The PV gradients were estimated using a variety of hydrographic climatologies, primarily derived from Argo measurements. The eddy diffusivities came from the DIMES experiment, a passive tracer and RAFOS float release experiment in the Southeast Pacific Ocean, and two other studies that used Argo float trajectories and Argo float profiles to provide estimates at 1000m and from the surface to 1950m respectively.

The eddy bolus velocities vary in the range of $10^{-4} - 10^{-2}$ m/s. The horizontal and vertical structure of these variations is controlled by the structure of both the eddy diffusivity and potential vorticity gradients, with no single dominant influence. However, the (structure of the) eddy diffusivity and large scale PV gradients are correlated, and show an increase as the ACC crosses over topographic features. In these topographically influenced regions the convergence of ACC streamlines also leads to convergence of PV contours, hence increasing the PV gradients. This convergence of streamlines also produces a steepening of isopycnals, creating a local region of enhanced available potential energy (APE). This enhanced APE is released via baroclinic instability, leading to greater eddy kinetic energy and thus greater eddy diffusivities in regions near topography. This ACC - topography interaction produces stronger eddy bolus velocities as a response to enhanced PV gradients and enhanced eddy diffusivities. Although numerous previous investigators have noted the role of topography in enhancing the eddy diffusivity (e.g. Lu and Speer (2010); Sallée et al. (2011); Thompson and Sallée (2012)), the obvious contribution of large scale PV gradients to the cross stream transport has not been noted.

The above story line might present a dilemma for the more dynamically inclined reader. Usually one expects the PV gradient and eddy diffusivity to be anti-correlated, because an increase in PV gradients constrains the movement of water parcels and should lead to a decrease in eddy diffusivity (Dritschel and McIntyre (2008)). However, It is possible that this relation between the eddy diffusivity and PV gradient is non-linear. Large increase of PV gradients in local regions (< 100 km, size of mesoscale eddies) can produce jets, very strong PV gradients and mixing barriers, and limit the cross stream flux. However, convergence of streamlines due to topography

leads to a modest increase in PV gradient over larger scales ($500 - 1000$ km, width of the ACC) and enhances the averaged eddy diffusivity, by increasing EKE, and thus increases the cross stream flux. However, this is a hypothesis that remains to be checked using idealized modeling studies.

Speer et al. (2000) estimated that the zonally averaged eddy bolus velocity should be on the order of 10^-3 m/s. Naveira-Garabato et al. (2007) estimated an upwelling rate of 330 ± 110 m/yr, which corresponds to a cross stream bolus velocity (v^*) of 10^{-2}m/s, in the Scotia Sea by estimating the rate of translation of the center of mass of a helium plume across the ACC streamlines. Garabato et al. (2016) provided an estimate on the order of 10^{-3} m/s, also in the Scotia Sea, using microstructure measurements. The zonally averaged value and the estimates in the highly stirred Scotia Sea compare well with our estimates. It is no surprise that our estimates show that regions of smaller v^* exist. The total zonally integrated meridional transport is approximately 25 Sv in the density range of 27.5 - 28 γ. For the same density range Lumpkin and Speer (2007) have estimated a zonally averaged meridional overturning transport of approximately 10-15 Sv using inverse models. Mazloff et al. (2013), using SOSE estimated a meridional overturning transport of approximately 10Sv as well. However, the eddy driven component was greater, and partially cancelled by the mean geostrophic flow. Our result is consistent with this view, and an eddy driven transport that is greater than the total overturning transport is to be expected.

The first key result of this study is that the diffusivity estimates, which were estimated during the DIMES experiment and by other studies instigated due to the DIMES experiment, are able to provide eddy transport estimates that are consistent with previous work from observations and models. The second key result is bringing to light the important contribution of PV gradients in setting the zonal variations of the eddy transport, which even though known previously has remained under appreciated. The zonal structure of the eddy transports quantified here will help in improving our understanding of the 3D structure of the MOC.
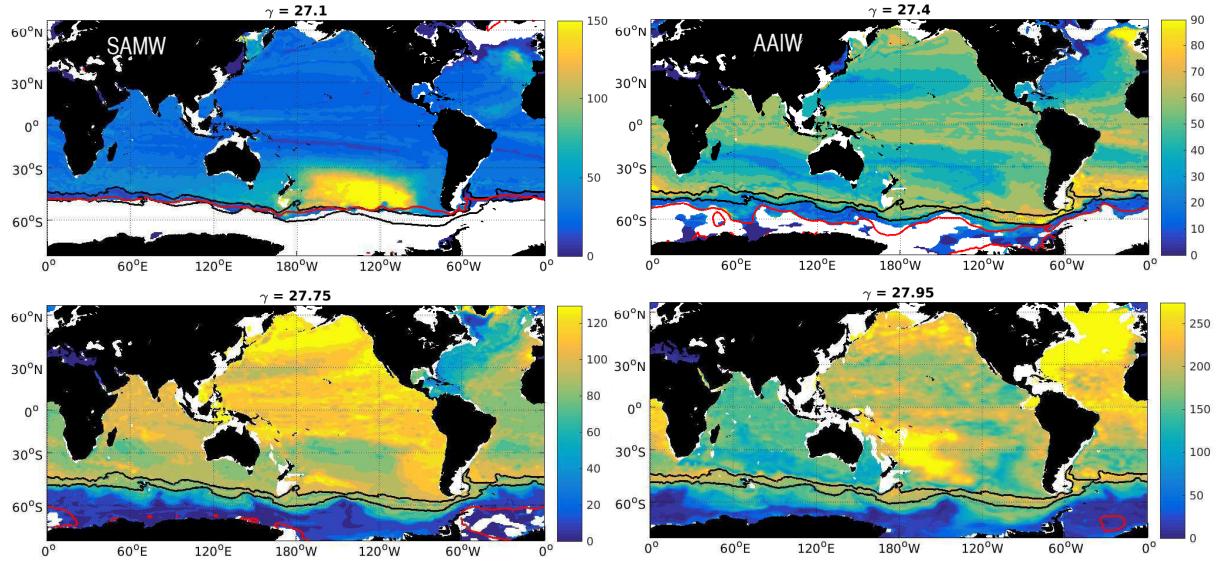
Figure 3.1: Global structure of isopycnal thickness for different water masses that are of interest for the Southern Ocean (water masses and neutral density are marked on the panel). The black contour lines represent the approximate positions of the SubAntarctic Front (SAF), northern contour, and Polar Front (PF), southern contour, defined as the -3cm and -60cm SSH contours. The red contour marks the climatological outcropping position of the corresponding isopycnal in late winter (September).
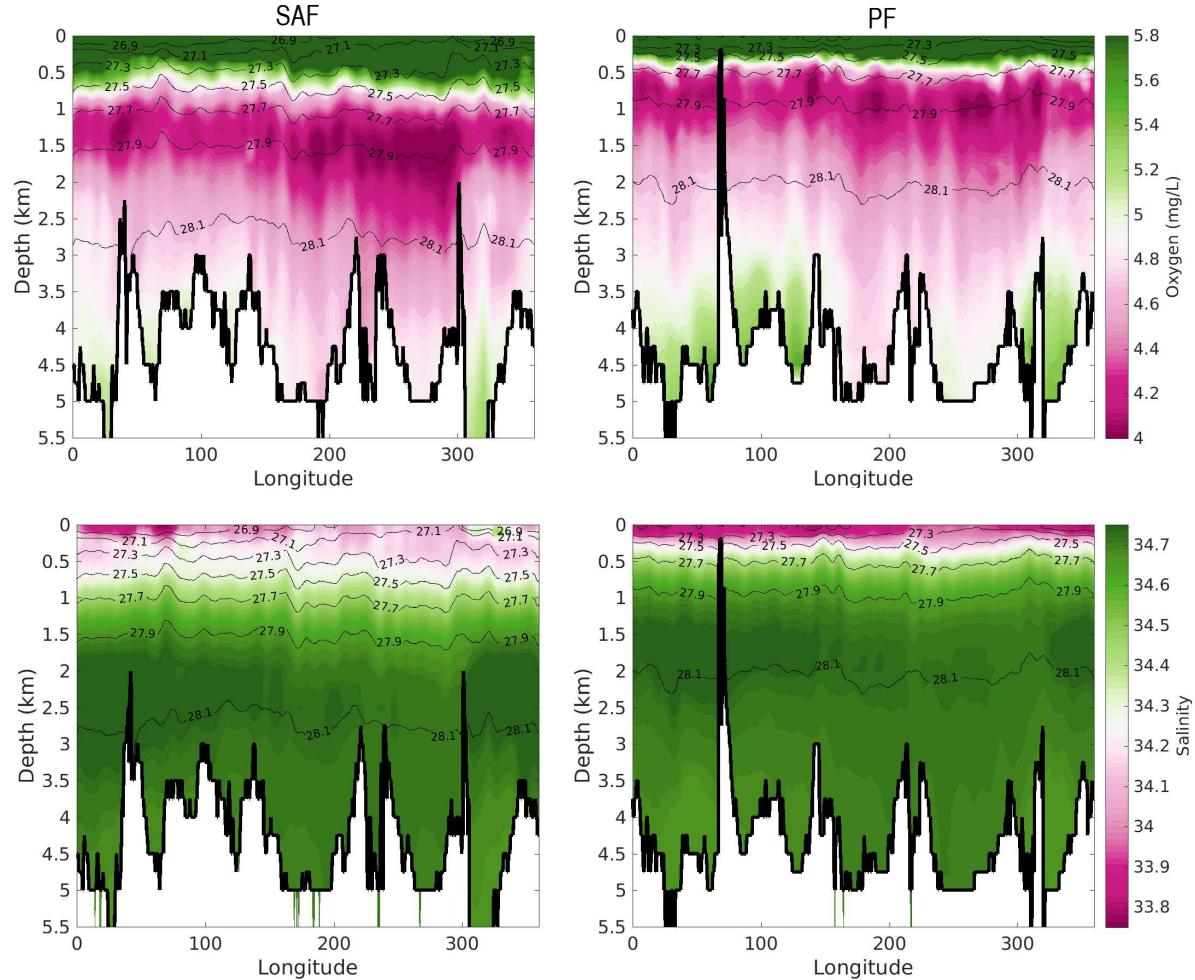
Figure 3.2: Longitude vs depth structure of oxygen (top) and salinity (bottom) concentrations along the SAF and PF, which are marked in Figure 3.1. The thin black contours represent the positions of the isopycnals and the thick black contour marks the bottom topography.
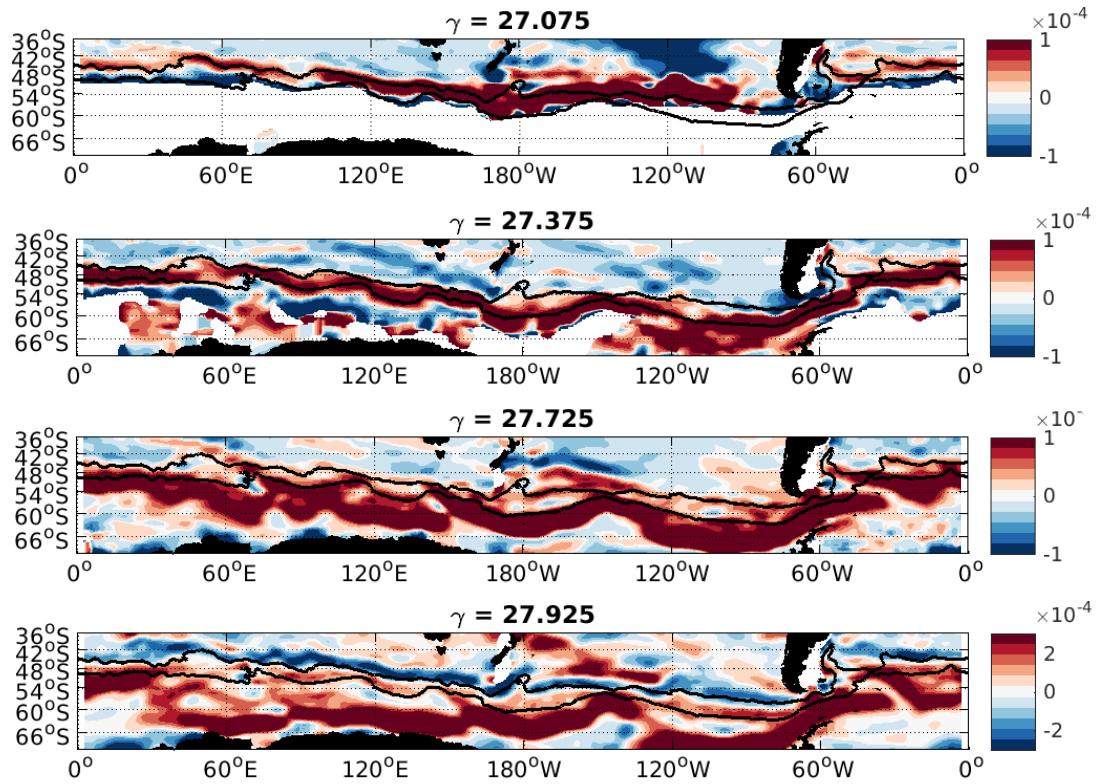
Figure 3.3: Meridional thickness gradients (dh/dy) along different isopycnal sufaces (labeled). The black contours mark the SAF and PF.
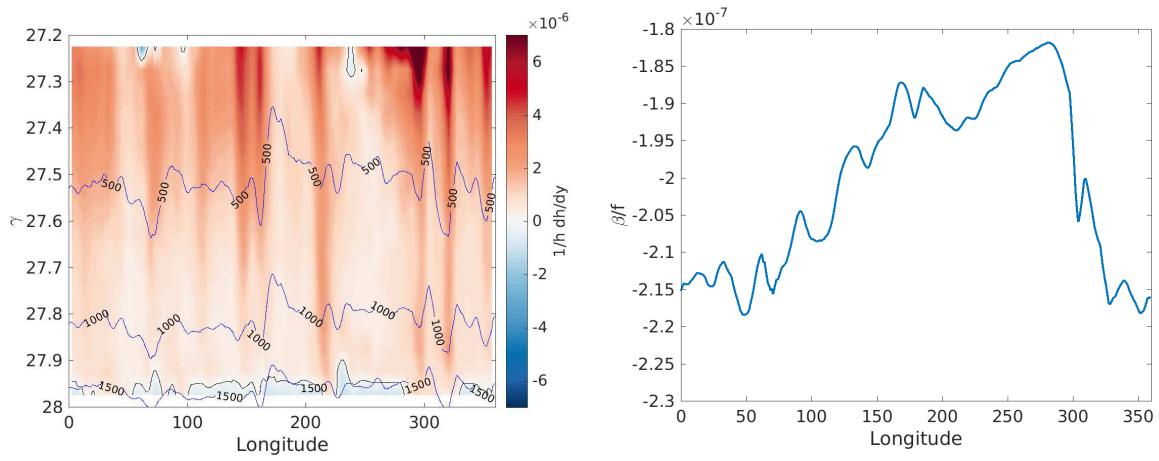
Figure 3.4: Left - Across stream gradients of layer thickness normalized by layer thickness $(1/h\partial h/\partial y)$ averaged in the region between the SAF and PF. Blue contours mark the average depth between the SAF and PF corresponding to the isopycnal layer. Right - β/f along the ACC, averaged in between the SAF and PF.
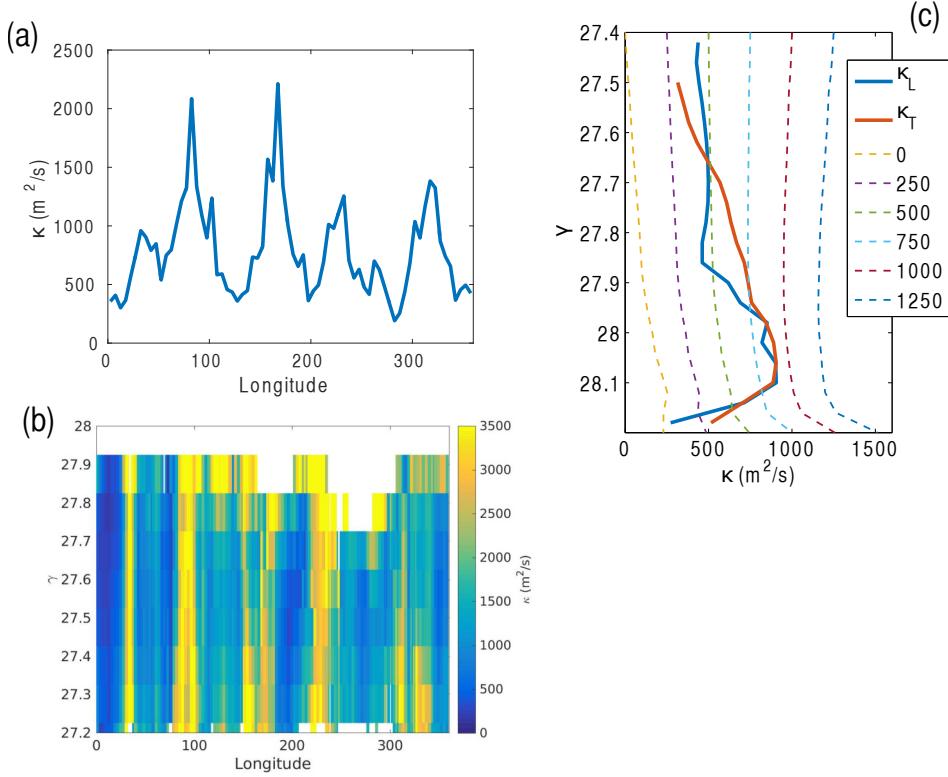
Figure 3.5: (a) Diffusivity estimates (κ_R) from trajectories of Argo floats (Roach et al. (2016)), which are representative of the horizontal eddy stirring at 1000m and south of 45S. (b) Diffusivity estimates (κ_C) from temperature and salinity profiles collected by Argo floats (Cole et al. (2015)), averaged between the SAF and PF as a function of density. (c) Diffusivity estimates from DIMES tracer release (Tulloch et al. (2014)), κ_T, and DIMES float release (Lacasce et al. (2014)), κ_L, augmented with a high resolution numerical model to obtain the vertical structure. The dashed lines show the κ_{GM} corresponding to different boundary conditions at $\gamma = 27.4$, as labeled in legend, used to solve equation 4.
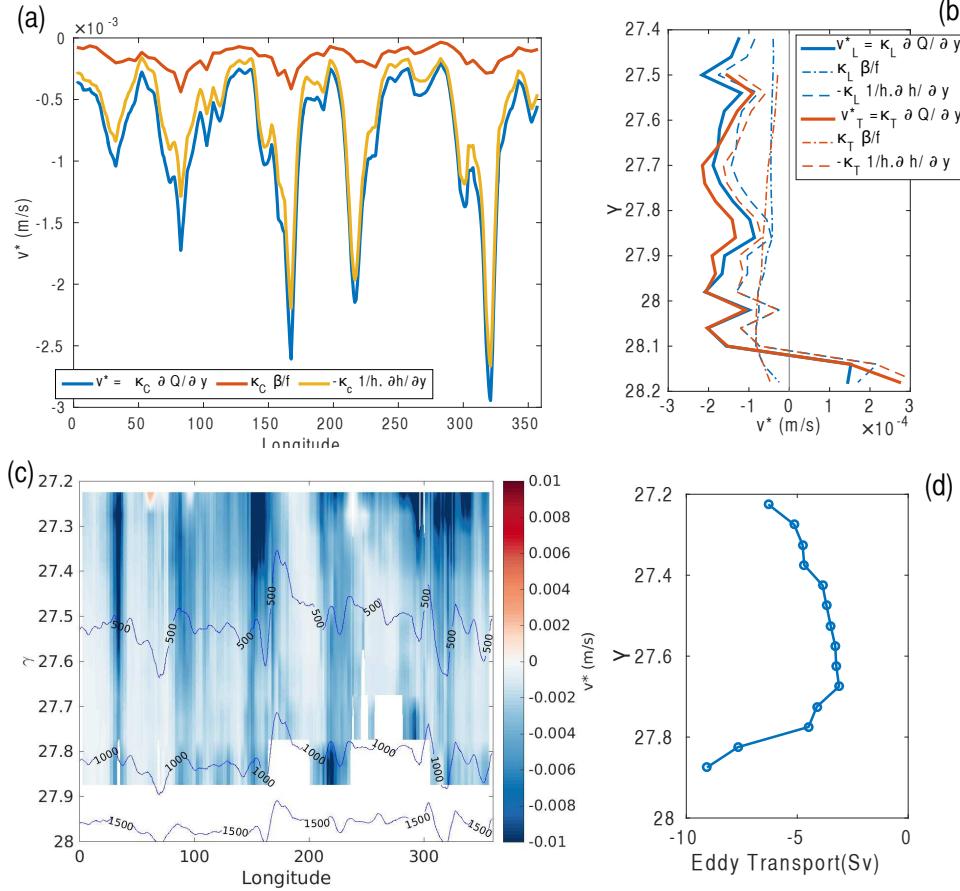
Figure 3.6: (a) Eddy bolus velocity (v^*) calculated using κ_R and PV gradients on 27.8 neutral density surface, which lies at approximately at a depth of 1000m in between the SAF and PF. The blue, yellow and red lines are the contributions corresponding to the total PV gradient, thickness gradient and planetary PV gradient respectively. (b) Eddy bolus velocity calculated using κ_T and κ_L in the Southeast Pacific. Different contributions to the total v^* are plotted and labeled in the legend. (c) Eddy bolus velocity calculated using κ_C. (d) Zonally integrated eddy transport ($\oint v^* \bar{h} dx$) on individual density layers ($\delta\rho = 0.05$) calculated using the v^* from panel c.

66

CHAPTER 4

MESOSCALE TURBULENCE AND DISPERSION IN THE ANTARCTIC CIRCUMPOLAR CURRENT

4.1   Introduction

Large scale flow in the ocean is often characterized by small values of the Rossby number ($Ro = U/fL$, where U is a characteristic velocity scale, L is the characteristic length scale and f is the Coriollis frequency). Turbulence at small Ro in the interior of the fluid, interior quasi-geostrophy (QG), is theoretically hypothesized to have two inertial cascades (Charney (1971)), a forward cascade of potential enstrophy (k^{-3}, where k is the wavenumber) and an inverse cascade of total eddy energy ($k^{-5/3}$) separated at an intermediate eddy energy injection length scale. The eddy energy injection length scale in the ocean is approximately at the first Rossby radius of deformation, where baroclinic instability injects kinetic energy into the barotropic mode (Salmon (1978)).

Since the development of these ideas, investigators have tried to determine the validity of these cascades in the ocean and atmosphere. Atmospheric observations from measurements along commercial flight paths have established the presence of a spectral slope of k^{-3} at wavenumbers higher than those corresponding to the (atmospheric) Rossby deformation radius, but no indication of $k^{-5/3}$ in the low wavenumber range (Nastrom and Gage (1985)), for the kinetic energy spectrum. However, the same atmospheric observations revealed the presence of a $k^{-5/3}$ spectra at the high wavenumber range. The possible mechanism responsible for this latter range have been postulated to be inertia-gravity waves (Dewan, 1997; Callies et al., 2014), stratified turbulence (Lindborg, 2006, 2015) and surface dynamics (Tulloch and Smith, 2006).

Direct measurements of the oceanic energy wavenumber spectrum have been limited to the surface ocean. These have relied on measurements of sea surface height (SSH) from satellite based altimeter (Stammer (1997); Scott and Wang (2005); Xu and Fu (2012)), measurements of upper ocean velocities from ship based ADCP (Wang et al. (2009); Callies and Ferrari (2013)), and measurements using surface drifters (e.g. LaCasce and Ohlmann (2003); Koszalka et al. (2009); Poje et al. (2014); Balwada et al. (2016a)). The results generally indicate the presence of an

enstrophy cascade at length scales between approximately 40 - 100 km, and hints of an inverse energy cascade at large-scales. Tulloch et al. (2011) suggested that the energy injection scales of the baroclinic instability in the ocean are marginally smaller than the observed eddy length scales, hinting at a small range of scales where the inverse energy cascade might be operating. Surface based observations (Callies and Ferrari (2013); Rocha et al. (2015); Balwada et al. (2016a)) have also indicated the presence of shallow energy spectra at smaller length scales (submesoscale, $< 30 km$), reminiscent of the observations from the atmosphere. The different mechanisms that have been proposed for this shallow spectra range in the ocean rely critically on the presence of a surface boundary, at which the vertical velocity disappears, and is forced by winds and buoyancy (recent reviews can be found in Thomas et al. (2008); McWilliams (2016)).

Observing the energy spectrum in the deep ocean is challenging due to the difficulty associated with measuring the flow at depth. Deep flows can only be measured directly with Lagrangian floats and moored current meters, the latter providing observations that are typically a very sparse sampling of the kinetic energy spectrum. Pairs of Lagrangian floats can be used to estimate the characteristics of the energy spectrum, the details of the methods are provided in section 2. The direct method is to estimate second order velocity structure functions ($S2$) from the velocities measured by floats. The S2 are related to the velocity correlations as a function of separation, and thus to the energy spectrum via a Fourier transform (Babiano et al. (1985)). The indirect method is to estimate the relative dispersion, second moment of the displacement PDFs, and other associated moments of the displacement PDFs from the floats. The moments of the displacement PDF and their evolution in time can then be used to characterize the slopes of the energy spectrum, as the slope of the energy spectrum governs the evolution of these displacement PDFs (LaCasce (2010)). It is important to note here that understanding the dispersion in the ocean is important in its own right, and not simply as a tool to diagnose the energy spectrum. Eddying flows in the ocean, such as the Antarctic Circumpolar Current (ACC), Gulf Stream etc., play an important role in transport and dispersal of heat, carbon, nutrients and other climatically important tracers (e.g. Gnanadesikan et al. (2015)). Observations of oceanic dispersal can help improve parameterizations of sub-grid processes in ocean models and help better quantify and constrain the ocean circulation (e.g. Hallberg and Gnanadesikan (2006)).

Here we will use both the above mentioned approaches to analyze a Lagrangian data set that sampled the mid-depth circulation of the ACC. RAFOS floats were deployed as part of the Diapycnal and Isopycnal Mixing Experiment in the Southern Ocean (DIMES) to sample the flow in the Southeast Pacific Ocean and Scotia Sea sectors of the ACC. The floats were deployed in pairs and triplets to sample the smallest scales ($\sim 1 - 3$ km) initially. We also advected particles in a numerical model to compare against the observational results.

4.2   Theory

The inertial ranges of interior QG turbulence are analogous to those of 2D turbulence theory (Kraichnan (1967); Charney (1971)), with the exception that inertial ranges for interior QG apply to total energy instead of kinetic energy. However, in interior QG the potential energy spectrum is equal to the longitudinal kinetic energy spectrum, longitudinal and transverse directions are defined later. Also, the longitudinal and transverse kinetic energy spectra have the same slopes for power law behavior. Thus, k^{-3} and $k^{-5/3}$ power law scalings also apply to both components of the kinetic energy in interior QG. First we discuss the structure functions and their relation to the energy spectrum, and next we describe the relative dispersion behavior expected for particle pairs in different inertial cascade ranges.

4.2.1   Structure Functions

Structure functions are fundamental metrics used to characterize turbulent behavior. The i component of the pth order structure velocity function is defined as $Sp_i = < \delta u_i^p >$, where $\delta u_i = u_i(\mathbf{x}) - u_i(\mathbf{x}')$ is the difference of a velocity component between two positions, and $< . >$ is an ensemble averaging. Usually the velocity components are decomposed into the longitudinal ($u_l = \mathbf{u}.\mathbf{r}/|\mathbf{r}|$) and transverse ($u_t = \mathbf{u} \times \mathbf{r}/|\mathbf{r}|$) components, where $\mathbf{r} = \mathbf{x} - \mathbf{x}'$ is the position vector connecting the two positions.

The second order velocity structure function ($S2_i$) is directly relatable to the kinetic energy spectrum as,

$$S2_i(r) = 2 \int_0^\infty E_i(k)(1 - J_0(kr))dk, \tag{4.1}$$

where $E_i(k)$ is the i component of the energy spectrum $(u_i^2 = \int_0^\infty E_i(k)dk)$, and $r = |\mathbf{r}|$. This can be approximated as,

$$S2_i(r) \approx 2\{\frac{r^2}{4} \int_0^{2/r} k^2 E_i(k)dk + \int_{2/r}^\infty E_i(k)dk\}, \tag{4.2}$$

using the asymptotic limits of $(1 - J_0(kr))$. This approximate form reveals the physical significance of $S2_i(r)$. $S2_i(r)$ is a cumulative quantity that sums the energy of eddies that are smaller than $\pi r/2$ and the enstrophy of the eddies that are larger than $\pi r/2$, where the length scale corresponding to k is π/k. Physically this means that the eddies that are smaller than the separation distance contribute their kinetic energy to the $S2_i(r)$, while the eddies that are larger than separation distance contribute through their imposed velocity gradient to $S2_i(r)$ (Davidson, 2015).

It can be shown using equation 1, or scaling arguments, that $S2_i \sim r^n$ when $E_i \sim k^{-(n+1)}$, for long inertial ranges and $1 < n + 1 < 3$. Thus $S2_l \sim S2_t \sim r^2$ for the enstrophy cascade and $S2_l \sim S2_t \sim r^{2/3}$ for the energy cascade (Babiano et al. (1985), Lindborg (1999)). Conditions of 2D incompressibility and isotropy relate the longitudinal and transverse components as $S2_t = d(rS2_l)/dr$. Thus, if $S2_t \sim S2_l \sim r^m$ then the ratio $S2_t/S2_l = m + 1$ (Lindborg (2007)).

It is also possible to perform a Helmholtz decomposition on $S2$, i.e. a decomposition into its corresponding rotational $(S2_r)$ and divergent $(S2_d)$ components, using the relations (Lindborg (2015))

$$S2_r = S2_t + \int_0^r \frac{1}{r}(S2_t - S2_l)dr \tag{4.3}$$

$$S2_d = S2_l - \int_0^r \frac{1}{r}(S2_t - S2_l)dr, \tag{4.4}$$

provided that the flow is isotropic and homogeneous.

Exact relations can be derived for the longitudinal component of the third order velocity structure function in isotropic 2D turbulence (Lindborg (1999)). The relation is $S3 = <\delta\mathbf{u}.\delta\mathbf{u}\delta u_l> = 1/4\eta r^3$ in the enstrophy cascade regime, where η is the enstrophy dissipation rate, and the relation is $S3 = <\delta\mathbf{u}.\delta\mathbf{u}\delta u_l> = 2Pr$ in the energy cascade regime, where P is the energy dissipation rate. Here the sign of P indicates the directionality of the energy cascade, large to small (negative) or small to large (positive) scales (Lindborg and Cho (2001)).

Velocity structure functions can be easily calculated using velocity observations from Lagrangian floats, provided that at least two floats sample the flow field simultaneously. Such calculations have

been performed previously using Lagrangian observations by Koszalka et al. (2009); Beron-Vera and LaCasce (2016); Balwada et al. (2016a) using surface drifters.

4.2.2 Relative Dispersion

Spreading of pairs of particles in a turbulent flow for homogeneous, incompressible 2-D flow can be described in terms of probability distribution functions (PDF) of pair separations, which can be shown to evolve in accordance with the Fokker-Plank (F-P) equation (Richardson (1926); Kraichnan (1966); Lundgren (1981)),

$$\frac{\partial}{\partial t}p = \frac{1}{r}\frac{\partial}{\partial r}(r\kappa_2\frac{\partial}{\partial r}p), \tag{4.5}$$

where $p(r,t)$ is the separation PDF and $\kappa_2(r)$ is the relative diffusivity.

Relative diffusivity (κ_2) is defined as

$$\kappa_2 = \frac{1}{2}\frac{d\overline{r^2}}{dt} = \overline{r_o v(t_o)} + \int_{t_o}^t \overline{v(t)v(\tau)}d\tau \tag{4.6}$$

where r is the pair separation, v is the pair separation velocity, and the $\overline{(.)}$ implies an ensemble average. $\overline{v^2(t)} = \overline{(u_1(t) - u_2(t))^2}$ and the velocity correlation are related as,

$$2\overline{u_1 u_2} = 2\mu^2 - \overline{(u_1(t) - u_2(t))^2}, \tag{4.7}$$

where u_1, u_2 are the velocities for float 1 and 2 that belong to a pair, and μ^2 is the velocity variance. The second term on the RHS of equation 6 is proportional to the second order velocity structure function. At large length scales and long times, where the velocity correlation is zero, the second order structure function is twice the velocity variance and the relative diffusivity is a constant, which is twice the single particle diffusivity (LaCasce (2008)).

LaCasce (2010) present analytical solution to equation 5 for three forms of κ_2, corresponding to the case of a constant diffusivity or Rayleigh regime, an energy cascade or Richardson regime ($\kappa_2 = \beta r^{4/3}$, where is β is proportional to the third root of energy dissipation rate), and an enstrophy cascade or Lundgren regime ($\kappa_2 = r^2/T_L$, where T_L is proportional to the inverse cubic root of the enstrophy dissipation rate). The relationship of the relative diffusivity to different inertial cascades is derived based on scaling arguments. The usual approach, also followed here, is to compare the separation PDF and its moments obtained from the solution of equation 5 to the observed PDF

and its moments. The exact solutions for $p(r, t)$ are listed in the appendix of Graff et al. (2015). Here, we only discuss the key results.

In the Rayleigh regime ($\kappa_2 = constant$) the kurtosis ($Ku = <r^4>/<r^2>^2$, the fourth moment of the PDF normalized by the square of the second moment of the PDF) asymptotes to 2 and the relative dispersion grows linearly in time. Equation A1 and A2 in Graff et al. (2015) present the solution for the PDF and its asymptotic form, which is self-similar, solution for this regime.

The Richardson regime ($\kappa_2 = \beta r^{4/3}$) is a local dispersion regime, where local implies that the relative dispersion is driven by the eddies that are the size of the separation scale (Richardson (1926)). For this regime the kurtosis asymptotes to 5.6 and the dispersion grows as t^3. Graff et al. (2015) present the solution for the PDF and its asymptotic form, which is self-similar (A7 and A16).

The Lundgren regime ($\kappa_2 = r^2/T_L$) is also referred to as the non-local dispersion regime, where non-local implies that the stirring is produced by eddies that are much larger in scale than the separation scale (Lundgren (1981)). In this case the PDF is not self similar (equation A20 in Graff et al. (2015)), and instead becomes more peaked in time. The relative dispersion and kurtosis grow exponentially with a growth rate of $T_L/8$.

4.2.3   Finite Scale Lyapunov Exponents

Finite Scale Lyapunov Exponents (FSLE) is an alternative statistic to relative dispersion, which averages in spatial rather than temporal bins. It has the same advantages as S2 as a scale dependent metric, allowing the use of all pairs that pass through a distance bin, and does not rely critically on pairs that are initially released together.

The FSLE is defined as the time scale corresponding to the growth rate of the separation (δ). The rate of growth of delta is assumed to be represented by an exponential function in the definition ($\delta = \delta_o exp(\lambda t)$), with λ being the Lyapunov exponent. The growth rate (spreading rate) is truly exponential if λ is a constant, as would be expected in the Lungdren regime of relative dispersion when the energy spectrum follows a power law that corresponds to k^{-3} or steeper. As λ is an inverse time scale, it can be expected to have different slopes on log-log plots corresponding to the different dispersion regimes. For the local Richardson regime the slope will be -2/3 and for the diffusive Rayleigh regime the slope will by -2 (e.g. LaCasce (2008)).

4.3   Data and Methods

In this study we examine two sets of Lagrangian trajectories: RAFOS floats released during the DIMES experiment (Balwada et al. (2016b)), and numerical particles advected in a MITGCM simulation of flow in the Southeast Pacific Ocean and Scotia Sea (Lacasce et al. (2014)).

The RAFOS floats were released at two isopycnal levels along the $105^o W$ meridian, between $54^o - 60^o S$. The RAFOS floats behaved more akin to isobaric floats, and for the most part did not maintain their target isopycnal, so we grouped the RAFOS float trajectories into two depth bins: shallow(500-1000m) and deep(1000-1800m). As the entire analysis in this study hinges on the floats being present in the domain simultaneously and within small separations ($<$ 100 km), the results are representative of the flow downstream of 105^oW in the Southeast Pacific Ocean, where the floats were originally deployed in pairs and triplets (Figure 4.1). No two floats were simultaneously closer than 100 km in the Scotia Sea, so that region is not represented here.

Velocity structure function separation bins were chosen according to $r = 1000 \times 1.5^n, (n = 1, 2, 3...)$ m, to provide equally spaced bins on a log scale. The averaging was done over all available simultaneous velocity pairs in a separation bin and all time. It should be noted that float labels are not important for this analysis, i.e. no explicit consideration needs to be given to the history of a float pair. To reduce the effect of vertical shear we only consider velocity pairs from floats that were vertically separated by a maximum of 50 dbar. Varying this criterion between 25 - 100 dbar did not significantly alter the results.

As the FSLE (λ) can vary as a function of separation, it is suitable to calculate λ corresponding to the time it takes for a pair of particles separate from δ_n to δ_{n+1}. Defining $\alpha = \delta_{n+1}/\delta_n$, $n = 0, 1, 2...$ as the bin number and with δ_0 chosen as 1km. Then the FSLE, $\lambda = ln(\alpha)/\triangle t_n$, can be calculated by measuring the time taken ($\triangle t_n$) for the pair separation to grow by a factor of α. The λ corresponding to all the pairs in the domain are averaged, both spatially and temporally, to give a single value corresponding to each n to produce $\lambda(\delta_n)$. Care must be taken when calculating FSLEs, as the results can be sensitive to the methodology (LaCasce (2008); Lumpkin and Elipot (2010)). If the choice of α is too small, then its possible that the $\triangle t_n$ might be smaller than or comparable to the time resolution of the particle trajectories. This can be avoided by choosing a large enough α, tested by varying α till the FSLE results converge, and interpolating the particle trajectories to a finer time resolution. Here, we linearly interpolated between the resolved times.

The second issue that arises has to do with the definition of the $\triangle t_n$ when the pair separation might not grow monotonically. In this situation different $\triangle t_n$ may be defined, such as the fastest time or the first crossing time. This issue is very clearly described in Figure A1 of Lumpkin and Elipot (2010). We tested both the choices of $\triangle t_n$, and found that the choice did not have any substantial impact on the calculation of λ in our study. We present results corresponding the $\triangle t_n$ to be the fastest time possible, when it is possible to associate multiple times with the same separation event.

Calculations of the separation PDFs require float pairs to be identified and their evolution be tracked in time. Ideally, a large number of floats would be released in pairs, and these original pairs would be spread homogeneously over the domain to produce an even sampling. In practice, this is hard to achieve due to logistical limitations on number of floats that can be deployed, where floats can be released, and because some pairs are inevitably lost to instrument failures. Thus, when working with observation one has to rely on chance pairs, floats that are not originally released together, but move together at some later time. Labeling of two floats as a pair is a non-trivial issue (LaCasce and Bower (2000); LaCasce and Ohlmann (2003); Ollitrault et al. (2005)). If two floats come closer than a certain separation criterion, then they would be labelled a chance pair. However, deciding on the starting time of this chance pair, should it be minimum separation that this pair achieves, or the first time the separation goes under the criterion, or the last time time that the pair is less than the criterion, is not obvious. Here, primarily for simplicity, we selected the chance pairs and initialized them at the time when the two individuals corresponding to the chance pair are at their minimum separation. We also tested other choices of choosing pairs, not shown, and found that the conclusions of this study did not depend on this choice.

We define the maximum separation criteria for selecting chance pairs to be 20 km for both the shallow and deep float groups. To reduce the effect of the vertical shear on the pair separation we only use the float pairs that maintain a mean vertical separation of less than 200 dBar during the 100 day segments, noting that this is greater than vertical separation that is chosen for the calculation of structure functions. The results were not very sensitive to the choice of 200dBar. These choices provide us with 72 pairs at the shallow level and 88 pairs at the deep level. The distribution of the initial separations is shown in Fig.4.1b and c and the trajectories of the pairs is shown in Fig.4.1d and e for the shallow and deep floats respectively. As we are using chance pairs, some of the pairs start downstream of the $105^o W$ deployment line. Fig.4.1f shows the trajectories

74

of the pairs in depth-latitude space and supports our choice of depth levels to divide the data into groups.

The numerical particles used here are the same as those used in Lacasce et al. (2014). The velocity fields, used to advect the particles, were simulated using the MITGCM with a horizontal resolution of 3km X 6km and 70 vertical levels. The model domain spanned $160^o - 20^oW$ and $75^o - 35^oS$, and was forced at the lateral boundaries by Ocean Comprehensive Atlas (OCCA) and at the surface by ECMWF ERA-Interim 6h wind fields. Details of the model run and comparison to hydrography can be found in Tulloch et al. (2014). 100 particles were released at 20 vertical levels (defined by isopycnal surfaces), between $55^o - 60^oS$, along a line at 105^oW, at a separation of the grid resolution, every 10 days for 120 days (12 releases) and advected using the 1 day averaged full 3D velocity fields. This provided 1200 particle trajectories at each of the 20 levels spanning from 300 m to 3000 m. Particles released at adjacent grid points were considered as pairs, and due to the large number of original pairs there was no need to consider chance pairs.

Fig.4.1 g,h and i show the numerical trajectories for the particles at three of the 20 vertical levels, which are considered in this study, with mean depths of 750, 1450 and 2100m. Similar to the RAFOS floats, the shallower particles are advected farther down stream than the deep ones, and show the presence of large-scale ACC meanders. The depth-latitude trajectories of the particles (Fig.4.1j) shows that particles, similar to the RAFOS floats, span a range of depths due to the large scale sloping isopycnals and heaving of isopycnals due to eddies.

4.4   Results

4.4.1   Isotropy and Correlation

It is important to to address the time scales and length scales over which the pair separation are correlated and isotropic, as correlated motion is a prerequisite for the relative dispersion phenomenology. The assumption of homogeneity is satisfied as the spatial variation of eddy kinetic energy within the region of the ACC represented here is small (Balwada et al. (2016b)).

Isotropy is assessed by plotting the square root of the ratio of the zonal to meridional dispersion (Fig.4.2) as a function of time and a function of mean separation (Morel and Larceveque (1974)). The isotropy ratio starts at zero for the model particles as the particles were initially released along a longitude line. It quickly, by 10km and 10 days, increases to one for all depths, as the pair

orientations are randomized. The ratio starts to become greater than one by 70km and 50 days for the shallowest level considered (745m). For the intermediate depth particles (1450m) the ratio stays near one for the first 100 days and grows after the separation has increased to more than 200 km. The deepest particles (2100 m) show isotropic spreading over almost all scales and times. For the RAFOS floats the isotropy ratio is more variable, due to a small sample size, but oscillates around one. The shallow depth floats show an increase in the ratio from one, similar to the 750m particles, around 70-80 km and 40-50 days. The ratio for the deeper depth floats stays close one for the 100 day portions considered, during which the separation increases to about 200 km. The anisotropy at longer time and separations seen at shallower depths in the model and observations is due to the shear of the ACC, which diminishes with depth (Lacasce et al. (2014)).

The mean of the zonal and meridional velocity correlations is shown in Fig. 4.3. For both the particles and floats the motions are well correlated at the smallest sampled scales and the correlation gradually drops to below 0.5 by approximately 70-80 km separation. Due to the presence of a large scale ACC the zonal velocity correlation only decreases to 0.2, while the meridional velocity correlation reduces to zero at large separations (not shown). This is similar to the correlation of particles advected in atmospheric flows (Graff et al. (2015)). The correlations for the observations are more variable, but the general behavior replicates the model particle behavior very well. It should also be noted that the anisotropic behavior seen at longer separations and time, due to the presence of the ACC, starts to become prominent at separations and time when the correlation coefficient becomes smaller than 0.5. This indicates that at the smallest scales the particle pairs feel the influence of local eddy features, which are isotropic on average, and are only influenced by the ACC after significant spreading has taken place.

4.4.2 Relative Separation PDFs

Having established that both the model particles and RAFOS floats show correlated motion at length scales smaller than ~ 100 km and up to ~ 50 days, we focus on the relative separation statistics at scales smaller than these.

To compare these results against the theoretical expectations, discussed in section 2b, we first need to estimate the relevant theoretical parameters. Two parameters are needed for each of the three regimes: the initial separation r_o and the respective growth parameters; relative diffusivity for Rayleigh, β for Richardson and T_L for Lundgren. As all model particles are released at equal

separation with r_o of 5 km, the initial separation PDF is a delta function. For the observations we use the mean initial separation of all pairs as r_o, where the initial separation PDF has some structure (unlike a delta function). To estimate the growth parameters of the Richardson and Lundgren regime we perform a least squares fit of the theoretical relative dispersion curves to the observed and modeled relative dispersion curves. This is from day zero to the time it take for mean pair separation to increase by a factor of 'a' times the initial separation ($< r(t)^2 >^{0.5} = a < r_o^2 >^{0.5}$, $r(t)$ is the pair separation at time t, r_o is the initial pair separation). The factor 'a' was chosen to be 3.5 here, which leads to a comparison at a mean dispersion corresponding to 17.5 km for model particles and 28 km and 45 km for the deep and shallow floats. Further discussion of this choice is presented in appendix A. Essentially, the fitting needs to be done during the initial period when correlation coefficients are small. $a = 3.5$ was found to be a good compromise between letting the pairs spread and sample the flow dynamics, but not long enough that majority of the pairs have entered uncorrelated motion. The relative diffusivity for the Rayleigh regime was estimated by matching the variance of the PDF to $4\kappa_2 t$ at the time when ($< r(t)^2 >^{0.5} = a < r_o^2 >^{0.5}$).

The PDFs from the model particles are compared to the theoretical curves at 10 days after release (Fig.4.4a, b and c). PDFs at all depth levels compare well with the Lundgren PDF (solid). The Rayleigh PDF (dash-dot) has a larger mode, and the Richardson PDF has a smaller maximum in comparison to the model particles and to the Lundgren distributions. The relative dispersion grows faster at the shallower level as compared to the deeper levels (Fig.4.4d). However, the difference in growth rate between particles at 750 m and 1450 m is significantly more than the difference in growth rate between 1450 m and 2100 m (also shown in Fig. 4.12). The dispersion curves from the particles show a slightly better match with the exponential curve expected from the Lundgren curve (thin solid line), over the initial 10 days, as compared to the Richardson curve (dashed line). At longer time the dispersion does not flatten out to a linear growth regime, which is due to the ACC leading to shear dispersion at large scales (also shown in Fig. 5 of Lacasce et al. (2014)). Kurtosis at all depths show a close to exponential initial growth (Fig.4.4 e). The kurtosis for the 750m particles peaks to 25 around 15 days, while the peak for the 1450m particles is lower, closer to 15, and occurs at around 25 days. Overall, the spreading of pairs is more rapid at the shallowest level and the statistics are comparable at the two deeper levels.

The PDFs from the RAFOS float observations are compared to the theoretical PDFs in Fig.4.5 a and b, also at 10 days after release. The PDFs at both the depth levels are indistinguishable from the Richardson or Lungdren PDFs, but appear to be clearly different from the Rayleigh PDFs. Thus the dispersion is clearly non-diffusive. The PDFs have tails that are thicker than the tails that were seen for the model pairs, which might be a result of not having very closely spaced initial pairs (20km). The relative dispersion for the shallower floats grows faster than that for the deeper floats. Both shallow and deep dispersion curves agree with both the Lundgren and Richardson dispersion curves within error bars (Fig.4.5c). The kurtosis for both the shallow and deep RAFOS float pairs show rapid initial growth that takes the peak values to greater than 5.6, but the peaks are at smaller values than those for the model particles (Fig.4.5d), and also the error bars at initial times on the kurtosis are very large. This hints at a slightly more Lungdren dispersion like behavior of PDFs. However, it is important to remember that the initial pair separation is not a delta function that is expected from theory and it will potentially take some time, presumably a few Lungdren time scales, before the influence of the initial condition of the PDF is not significant any more. Also, the initial separation PDF is non-smooth and looks bimodal, with lots of pairs at small initial separation corresponding to the original initial pairs and a significant number of pairs at the maximum separation of the bin corresponding to the chance pairs. The structure of this PDF can vary quite dramatically if a few pairs are dropped and resampled, as done when bootstrapping for estimating errors, and this will significantly affect the kurtosis. This is seen clearly as large errorbars on the kurtosis estimates for the first 20-30 days, varying between values of 0 - 25. At longer times, the dispersion smooths out the PDFs, also reducing the influence of individual pairs on it structure.

We further tested the effect that the initial distribution of separations has on the PDF metrics, by selecting model pairs to recreate an initial PDF that resembles the initial PDF from the observations. Note that even though the shape of the initial distribution is the same, the number of pairs is significantly greater and thus the results are robust. Here we only show results for model particles at 1450 m, which represent the RAFOS floats between 1000-1800 m (Fig. 4.6 a). The simulated PDF at 10 days is indistinguishable from both the Richardson and Lungdren PDFs. In particular thicker tails are noticed, similar to those seen for the observations. This is result of the large number of pairs that initially started farther apart ($\sim$ 20 km). The simulated relative

dispersion is also ambiguous. The kurtosis increases slowly to a value of 6 and then reduces gently, no initial exponential growth, expected for a Lungdren regime, is seen. This test shows that the 'initial' separation PDF from the observations, is atleast one direct limiting factor that affects our ability to identify the correct dispersion regime using the observations.

4.4.3 Second Order Structure Functions

Fig.4.7 a,b and c show the second order structure function ($S2$) and its different components calculated using the model particles. The total, longitudinal, transverse and rotational components of S2 follow power laws with a slope that is slightly smaller than 2 from the grid scale to approximately the decorrelation length scale (100km), where the structure functions flatten out to twice the velocity variance. The slopes are close to those expected for an enstrophy cascade, and no indication of an energy cascade is present. The total S2 is almost entirely produced by the rotational component, with very little contribution from the divergent component. The ratio of the transverse to the longitudinal component is approximately 2.5 for the shallowest and 1.5 for the deepest particles between 10 and 100km, this ratio should be 3 for a purely rotational enstrophy cascade (k^{-n}, with $n > 3$). As one examines deeper levels the slopes are farther from the enstrophy cascade slope of 2, the ratio between transverse and longitudinal component is smaller, and the relative influence of the divergent component is greater.

The second order structure functions from the RAFOS floats are shown in Fig.4.7 d and e for the shallow and deep floats respectively. S2 for both depths flatten out at the large scale to energy levels which are comparable to those from the model, indicating that the model and observations have comparable eddy kinetic energies. However, the observations clearly show that the S2 at the smaller length scales is greater than those from the model by almost an order of magnitude, indicating that the model is underestimating the kinetic energy at small scales. For the total S2 of shallow floats, at scales below 100 km, no clear power law behavior can be seen, but the approximate slope appears to be steeper than 2/3 and shallower than 2. The transverse component is greater than the longitudinal component and the rotational component is greater than and divergent component at all scales, but the different components appear to converge at the smallest observed scales. For the deeper floats, the slope of the total S2 flattens at separations greater than 100 km, is steeper than 2/3 in the 30-100 km separation range, and is approximately 2/3 below

79

30 km. The transverse component is equal to the longitudinal component at 5km separation, and greater between 5 - 200km.

The rotational component of S2 is significantly greater than the divergent component above 30 km separations, the rotational and divergent components converge at smaller scales. Also, the slope of the rotational component is steeper than the total, and is closer to 2.

In Fig. 4.8 the ratio of the divergent to rotational component of S2 and the Rossby number are shown. The ratio of the divergent to rotational component of S2 ($S2_d/S2_r$) for the model is always smaller than 0.5, and achieves its smallest value (< 0.1) close to 5 km. The ratio increases with increasing separations, which might be indicative of an increase in anisotropy. The decomposition method assumes isotropic flow, and the errors in the decomposition will grow as the flow becomes more anisotropic. In contrast to the model, the ratio, $S2_d/S2_r$, increases at smaller separations, being 0.6 for the shallow and 1 for the deep floats at 5 km. The deeper floats in particular show a very rapid growth in the ratio as the separation decreases, unlike the model particles. The Rossby number calculated using S2 is small for both the model and observations. Ro for the model stays almost constant below separation of 100 km, as one would expect in an enstrophy cascade (with $S2 \, r^2$, $Ro \, \sqrt{r^2}/fr = constant$, where C_o is a constant). The values at the shallower level are greater than at the deeper level, a result of the reduction in kinetic energy and S2 with depth. The Ro is clearly not a constant between separations of 5 - 100 kms for the observations, and both the deep and shallow values increase steadily with decreasing scale to 0.04 at 5 km. This is to be expected as the slope of S2 for the observations is shallower than 2. Also, the Ro for the shallow and deeper level are the same at 5 km, unlike the model.

4.4.4 Finite Scale Lyapunov Exponents

FSLEs calculated from the model particles and RAFOS floats show marked differences between the observations and model (Fig. 4.10). FSLEs for different values of α are shown to indicate that the results are converged, and are not sensitive to this choice. FSLEs from the model are flat on a log-log plot at length scales at length scales smaller than 100 km at all depth levels and steeper than -2/3 at larger length scales. This clearly implies that the model pair separations below 100 km for the model are exponential, as expected for Lungdren dispersion, and tending towards a diffusive regime above 100 km. The FSLEs from observations do not show any range over which the FSLEs are flat on a log-log plot. At the shallower level the FSLE has a slope of -2/3 at scales smaller than

80

10 km. The slope is less steep between 10 - 100 km, and then steeper again at length scales greater than 100km. At the deeper level the FLSE is marginally steeper than -2/3 below 2km, becoming less steep between 10-100 km, and steeper than -2/3 above 100 km. The FSLEs show indications of local dispersion for the observations, which is consistent with the observational structure functions having slopes that are significantly less steep than 2. In contrast the model clearly shows non-local dispersion, which is in agreement with the results from the displacement PDFS and to be expected based on S2 slopes close to 2.

4.4.5   Relative Diffusivity

We estimate the relative diffusivity (Fig. 4.9) as half the averaged rate of change of pair dispersion. Here the averaging is done over all pairs that are present in a separation bin, at all times, and after the time derivative is calculated. The relative diffusivity is on the order of 10 - 100 m^2/s at 10 km separation, varying with depth and in between observations and model. It is greater at the shallower levels than the deeper levels, for both the model and observations. Further, the observational relative diffusivities are greater than the model relative diffusivities at the smaller length scales, in agreement with the model having less energy than the observations at the smaller length scales. The relative diffusivity grows as r^2, expected in an enstrophy cascade, at the small scales and shallower at the large scales. The relative diffusivity does not approach a constant at large scales, as the large scale ACC shear will cause the zonal dispersion at large scales to grow due to shear. For a linear shear the relative diffusivity grows as $r^{4/3}$.

4.4.6   Third Order Structure Functions and Time Scales of the Enstrophy Cascade

In the enstrophy cascade of 2D turbulence an exact relationship for the third order structure function can be used to calculate the enstrophy dissipation rate ($\eta = 4S3/r^3$). Here we assume that the same relation can be used in the ocean at the appropriate length scales.

Second order velocity structure functions and the relative separation PDFs indicated the presence of an enstrophy cascade. We therefore check if S3 scales accordingly. We do not expect the S3 to be cubic at all the correlated scales, as the S2 were not exactly quadratic with separation. In Fig.4.11 we plot the S3 and compensated S3 ($S3/r^3$) at all depths. Except for the near-surface layer, all depth show a short range (5-20km) over which the S3 is cubic. This short range seems

81

reasonable as the deformation radius in this region is approximately 15km. At scales above 20km the S3 rolls off and flattens out, where the flattening to a constant happens at smaller length scales for deeper levels. There is no range of scales at which S3 is linear, as would be expected for an inverse energy cascade. S3 from the RAFOS floats are not shown as they were noisy and did not show any clear signal.

The time scale corresponding to the enstrophy dissipation rate $(T_\eta = \eta^{-1/3})$ should scale similar to the Lundgren time scale (T_L). We use the value of S3 in the short range between the grid size and the Rossby deformation radius to estimate $T_\eta = (4S3/r^3)^{-3}$. Comparing T_η to the T_L at showed that they are approximately related as $T_L \sim 8T_\eta$ (note that this factor of 8 is not related to the factor of 8 that appears in the exponential growth rate of the Lungdren regime). $8T_\eta$, which varies almost exactly like T_L, decreasing rapidly from 20 days at 300 m to 60 days at 1800 m, below which the variation is small (shown as the orange triangles in Fig. 4.12). It is important to note that the T_L and T_η, which are calculated using very different metrics, show the same vertical structure in depth. T_L estimated using the RAFOS floats are slightly greater than those estimated from the model (shown as points in Fig. A1), but this could potentially be due to the parameter fitting for the observations representing larger length scales (discussed in Appendix A).

4.5   Discussion

The relative separation PDFs and their associated moments for the model particle pairs released 5km apart are in agreement with isotropic non-local dispersion at length scales and time scales when pair motions are correlated, less than 100 km and 50 days. This result implies spectral slopes of k^{-3} or steeper. At large separation, the pair motion is uncorrelated and the mean shear of the ACC produces zonal anisotropy in spreading.

The RAFOS floats also showed correlated and isotropic motion at the same length and time scales as the model particles. However, the relative separation PDFs and its associated moments were inconclusive for the RAFOS floats. The kurtosis showed a short initial growth that may be in agreement with non-local dispersion, but the error bars on the kurtosis were large for the first 20 - 30 days. The inconclusive nature of the PDFs from the observations is due to a lack of sufficient number of pairs and a starting PDF that is very broad (0 - 20 km), unlike a delta function. Thus, results from observational PDFs mix information over scales, similar to the numerical particles

released at over a range of separations, and the PDFs cannot be used to distinguish between local and non-local dispersion.

Second order velocity structure functions calculated from the numerical particles follow power law behavior with an exponent close to two, which becomes smaller at deeper levels. The transverse component is greater than the longitudinal component at all length scales scales with correlated motion. At length scales greater than 100 km the second order velocity structure functions flatten out, and the transverse and longitudinal structure functions become equal in magnitude. A Helmoholtz decomposition shows that the rotational component contributes almost entirely to the total S2. The Rossby number was smaller than 0.03, decreased with depth, and is constant at separations smaller than 100km. These results are indicative of mesoscale turbulence that is approximately consistent with the interior quasi-geostrophic turbulence theory.

The S2 calculated from the RAFOS floats shows some similarities to those calculated from the numerical particles at length scales greater than approximately 30km. The slopes of the rotational component on a log-log plot are similar to those from numerical particles, and the energy level at which the observational S2 flatten out ($\sim$ 100 km) is also comparable to the model. However, the slope of the total S2 is shallower than the rotational component, becoming significantly different at smaller length scales. The total observational S2, sum of rotational and divergent components, are greater by factor of 5-10 than the total model S2 at length scales smaller than 30km. At these smaller length scales the longitudinal and transverse components have similar magnitudes, and also the rotational and divergent components become comparable in magnitude. The shallower float results were based on fewer data, and are less conclusive than the deeper floats. The Rossby number was smaller than 0.04, but showed a clear increasing trend as the separation becomes smaller.

This shallower slope of S2 at small length scales in the deep ocean is reminiscent of the atmospheric observations of shallower energy spectra at length scales smaller than the Rossby deformation radius (Nastrom and Gage (1985)). Shallow slopes of of energy spectrum at small length scales has also been observed in the surface ocean (Callies and Ferrari (2013); Rocha et al. (2015)), and has been attributed to inertia-gravity waves. However, at the surface a variety of other mechanisms are also possible, such as mixed layer instabilities, Langmuir turbulence, Ekman driven ageostrophic circulations, surface quasi-geostrophy etc, that can energize the smallest length scales and lead to shallower slopes of the energy spectra. Either way, it is not very surprising that flatter

spectra at smaller length scales are observed at the surface. It is, however, a surprising result that shallower slopes for S2 at smaller scales are observed in the interior. The mechanism of surface influenced dynamics can be ruled out as these observations were made at mid-depth, away from any boundaries. Thus, the shallower slopes of S2 can be a result of some combination of inertia gravity waves and vortical motions, and a divergent component that is comparable to the rotational component supports this.

The Rossby number, defined as $\sqrt{S2}/fr$, grows rapidly at separations smaller than 20km and approaches 0.04 at separations of 5 km, still much smaller than 1. Extrapolating this Ro to smaller scales, assuming $r^{2/3}$ dependence of S2, implies a Ro of 0.1 at 1km and 0.5 at 150m. This increase in Ro indicates that the flow may not necessarily be balanced at small scales. Also, the Ro discussed above are domain averaged Ro, and significantly higher values can be expected in specific regions, such as close to fronts. Thus there might be specific events in the interior where loss of balance leads to a forward cascade of energy, as has been shown in a few numerical simulations of interior flows (McWilliams (2016) and references therein).

FSLEs strongly indicate that there are differences in the characteristics of dispersion in the model and the observations. The FSLE from the model particles show exponential spreading, in agreement with the results of the separation PDFs showing non-local dispersion and S2 slopes close to 2. The FSLE from the observations indicate local dispersion, as one would expect based on the observational S2 having slopes that are clearly different from those of an enstrophy cascade. The relationship between the structure functions and dispersion (Bennett (1984)) is derived based on purely non-divergent 2D flows and not expected to hold for flows that have strong divergent components. However, its qualitative success in this study might be expected as the divergent component is much smaller than the rotational component over most of the length scales.

The relative diffusivities are scale dependent, and increase from 10 - 30 m^2/s at 5km to $\sim$ $1000 m^2/s$ at 100 km. The increase at length scales greater than 1000 km is probably due to the effects of the large scale horizontal shear associated with the ACC. The diffusivities observed by the floats are slightly greater than those from the model, approximately by a factor of 2 at length scales smaller than 100 km. This is in agreement with the rough estimate of 20-50 m^2/s, applicable in the 5-50km range, estimated from the observed DIMES tracer concentration roughness (Boland et al. (2015)).

Thus, we conclude that the DIMES floats observed local dispersion in the ACC at length scales where the pair velocities are correlated and spreading is non-diffusive ($< 100km$). This is based on the slopes of S2 being less steep than that expected for an enstrophy cascade, and FSLE showing no indications of exponential spreading. The separation PDFs produced ambiguous results, and could not distinguish between local and non-local dispersion due to limited number of original pairs.

These results challenge the commonly accepted phenomenology of lateral stirring in the ocean (Garrett (2006)), which assumes that the stirring is a 3 stage process - local dispersion and mixing at small length scales ($< 1km$) corresponding to small scale turbulent mixing, an intermediate range ($1 - 100km$) of non-local dispersion in the enstrophy cascade where the stirring is driven by mesoscale eddies and produces filamentary structures, and finally lateral diffusion corresponding to the uncorrelated motions of particles once they have separated to farther than the dominant size of the eddies ($> 100km$). Instead, it appears that the dispersion might be local, even in the interior of the ocean, at least up to length scales close to 30 km.

4.6   Fitting Parameters

Here we test the sensitivity of the Lungdren time scale (T_L) to the fitting parameters. Estimation of T_L depends on the choice of an initial separation (r_o) and a factor of 'a' times the initial separation ($< r^2 >^{0.5} = a < r_o^2 >^{0.5}$). A least squares fitting is done to the second moment of the separation PDF, relative dispersion, from the start to the time when the separation grows to 'a' times the initial separation to determine the growth parameters.

We test for two initial separations $r_o = 5, 25km$, the initial separation of numerical particle pairs discussed in the text, and a larger initial separation that might crudely represent the larger initial spread of RAFOS float pairs. We also discuss two cases of $a = 2.5 and 4.5$, $a = 3.5$ is the case discussed in the text. The results are shown in Fig. A1.

Associated with the factor of 'a' is a time T^* that is taken by the pairs to separate out to a distance of 'a' times the starting separation. T^* varies based on the choice of 'a' and r_o as should be expected, getting longer for larger 'a' and larger r_o.

T_L shows a greater sensitivity to r_o than 'a'. For $r_o = 5km$, T_L is insensitive to the choice of 'a', decreases rapidly from 20 days at 300 m to 60 days at 2000 m and stays constant below that depth. For $r_o = 25$ km, T_L increases with depth and the value of 'a'. Also, T_L has a greater value than

that estimated for the smaller initial separation. Thus, if the fitting is done at a time when the particles have separated significantly (greater 'a' and r_o) then the fit is not very accurate, and can overestimate T_L and be sensitive to choice of the fitting paramters. This is because the spreading is not quite exponential at larger separations, as pairs are transitioning from an enstrophy cascade to uncorrelated motion. This might be the reason for the observations showing larger T_L and some disagreement with the Lungdren separation (non-local) regime.
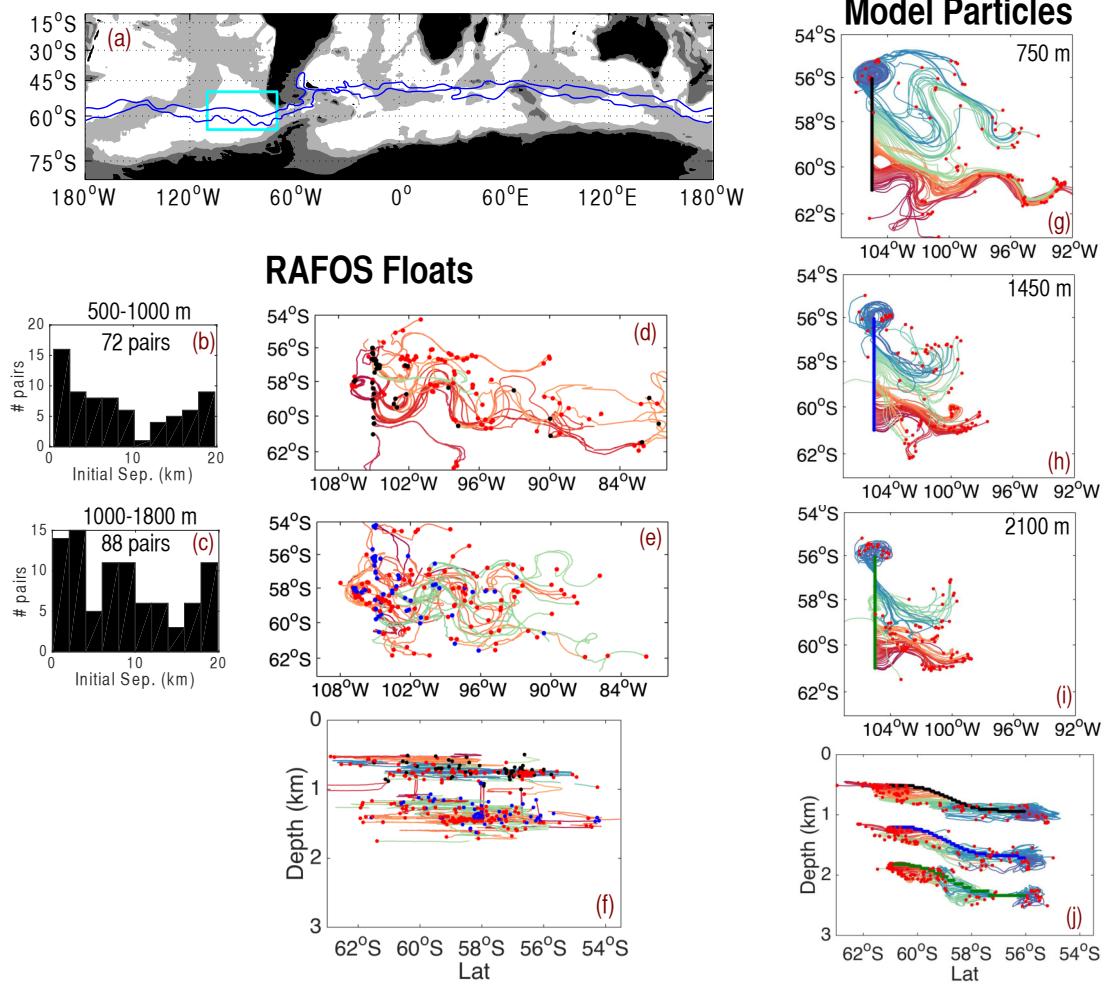
Figure 4.1: (a) Location of the DIMES experiment (cyan rectangle) along with the SAF and PF (blue contours, Orsi et al. (1995)), and bathymetric contours corresponding to 0, 2000 and 4000m. (b) and (c) Distribution of the initial separation of RAFOS float pairs considered in this study for 500-1000m and 1000-1800m depth ranges respectively. (d) and (e) Day 1-100 trajectories of the floats that belong to the same depth ranges as (b) and (c) respectively. (f) RAFOS float trajectories in depth vs latitude space. In (d), (e) and (f) the black and blue dots represent the initial position of the pairs in the deep and shallow depth bins, and red dots show the position after 100 days. (g), (h) and (i) Day 1-100 trajectories of a representative sample of model particles at mean depths of 750, 1450 and 2100m. (j) trajectories of the same particles in depth vs latitude space. In (g), (h), (i) and (j) the black, blue and green dots represent the initial positions and the red dots show the 100th day position of the particles at the three respective depth levels.
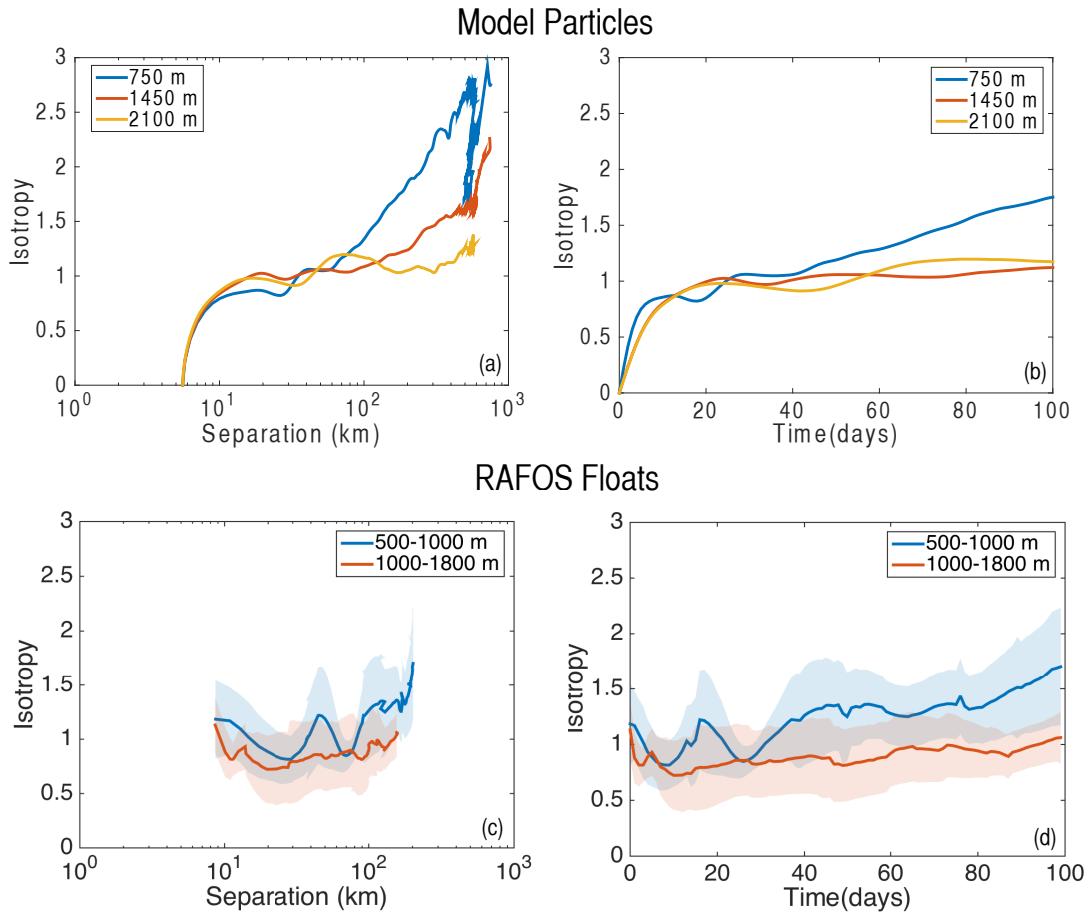
Figure 4.2: Isotropy, defined as the ratio of the square root of zonal vs meridional dispersion $(< r_x^2 > / < r_y^2 >)^{0.5}$, for the model particles (top pane, a, b) at three depths and RAFOS floats (bottom panel, c,d) in two depth bins.
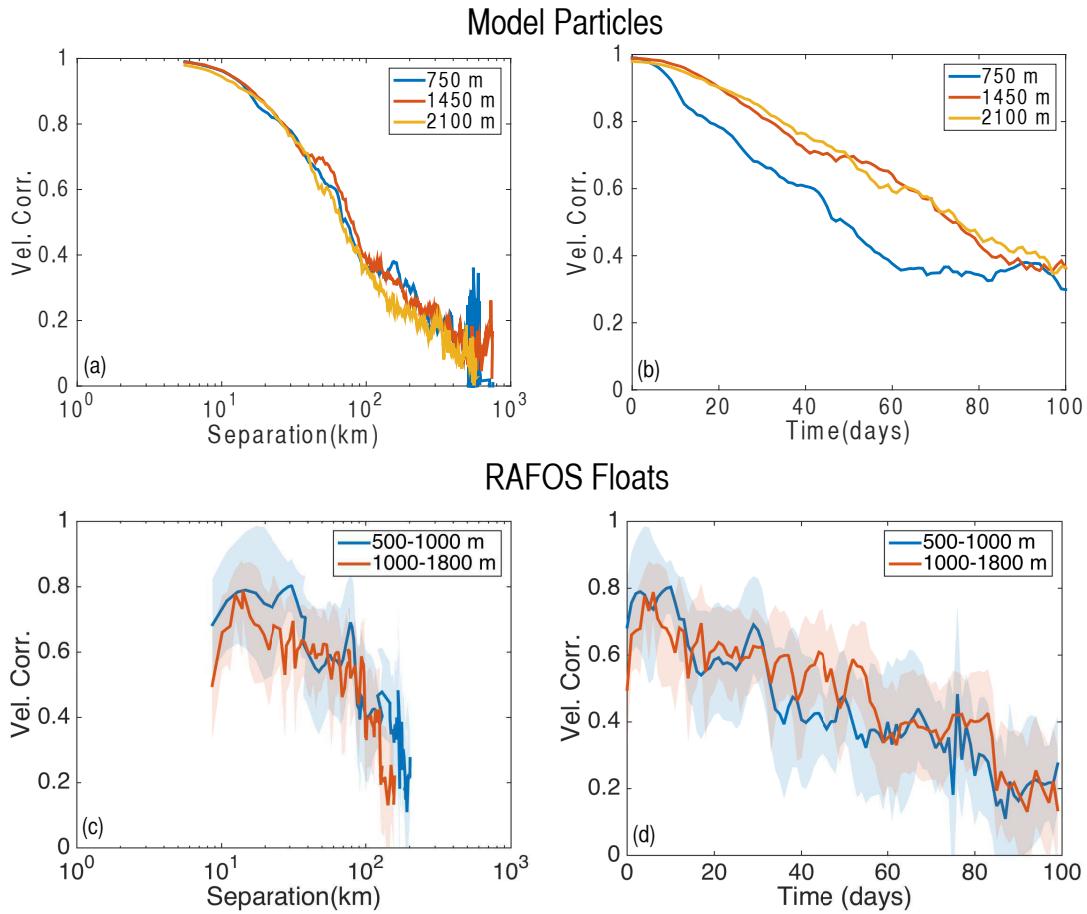
Figure 4.3: Mean of zonal and meridional velocity correlations for the model particles (top panel, a,b) at three depths and RAFOS floats (bottom panel, c, d) in two depth bins.
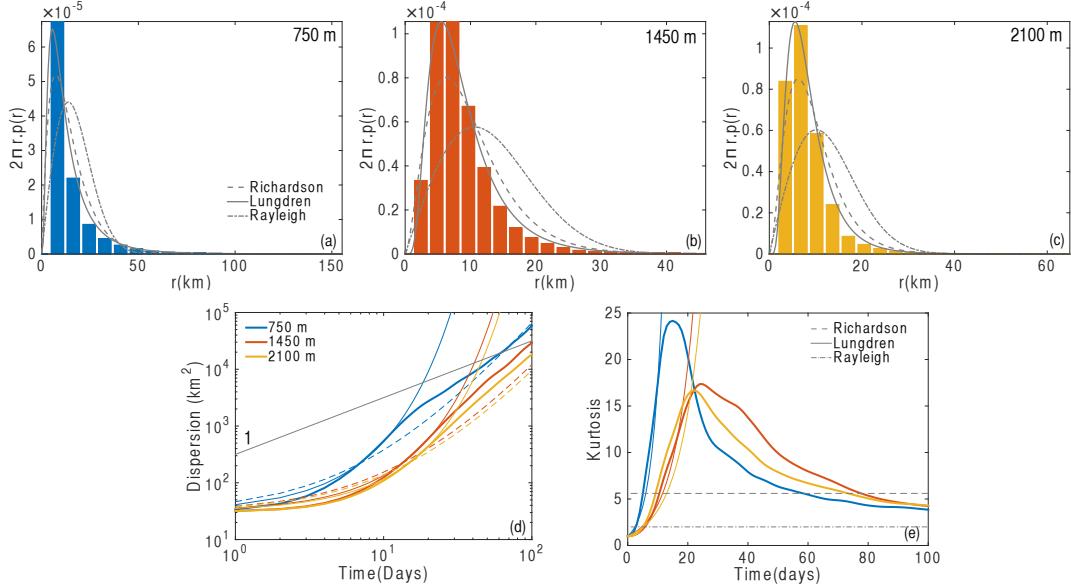
Figure 4.4: Temporal Statistics for model particle pairs. (a), (b) and (c) The displacement PDFs at 10 days after deployment for three depth levels (750, 1450 and 2100m). The dashed, solid and dotted dashed curves are the fits of Richardson, Lundgren and Rayleigh PDFs (details of fitting in text). (d) The relative dispersion for the particles at the three depths as thick solid lines (colored by depth). The theoretical fits, colored based on the depth, are shown as thin solid line for the Lundgren and dashed line for the Richardson dispersion. The gray line is the slope of 1 corresponding the Rayleigh dispersion (diffusive). (e) The kurtosis (thick solid lines) for the three depths, with the thin solid lines representing kurtosis for the fitted Lundgren curves (colored based on depth). Dashed line at 5.6 corresponds to the asymptotic Richardson regime and dot-dashed at 2 corresponds to the Rayleigh regime.
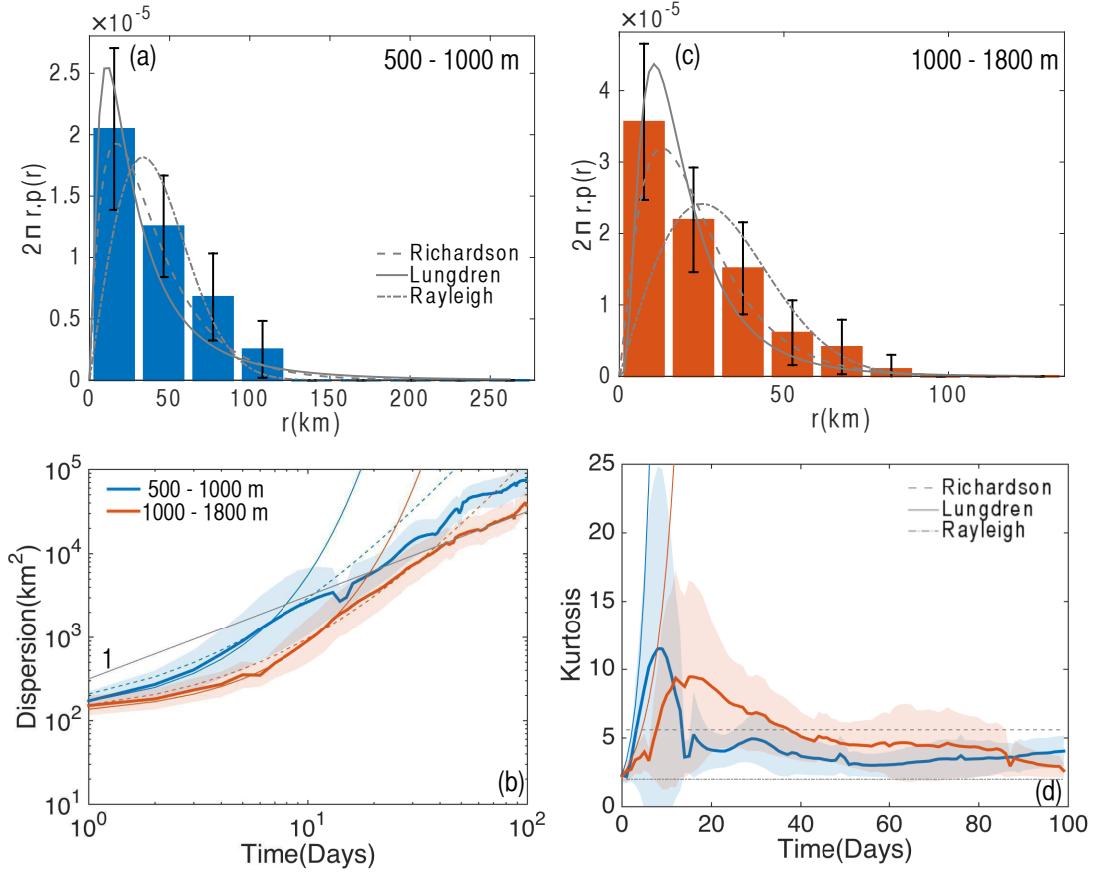
Figure 4.5: Temporal Statistics for RAFOS float pairs. (a) and (b)The displacement PDFs at 10 days after deployment for the two depth levels (500-1000m and 1000-1800m) respectively. The dashed, solid and dotted-dashed curves are the fitted Richardson, Lundgren and Rayleigh PDFs. (c) The relative dispersion for the floats in the two depth bins as thick solid lines colored by depth. The theoretical fits, colored based on the depth, are shown as thin solid line for the Lundgren and dashed line for the Richardson dispersion. The gray line is the slope of 1 corresponding the Rayleigh dispersion (diffusive). (d) The kurtosis (thick solid lines) for the same, with the thin solid lines representing kurtosis for the fitted Lundgren curves (colored based on depth). Dashed line at 5.6 corresponds to the asymptotic Richardson regime and dot-dashed at 2 corresponds to the Rayleigh regime.
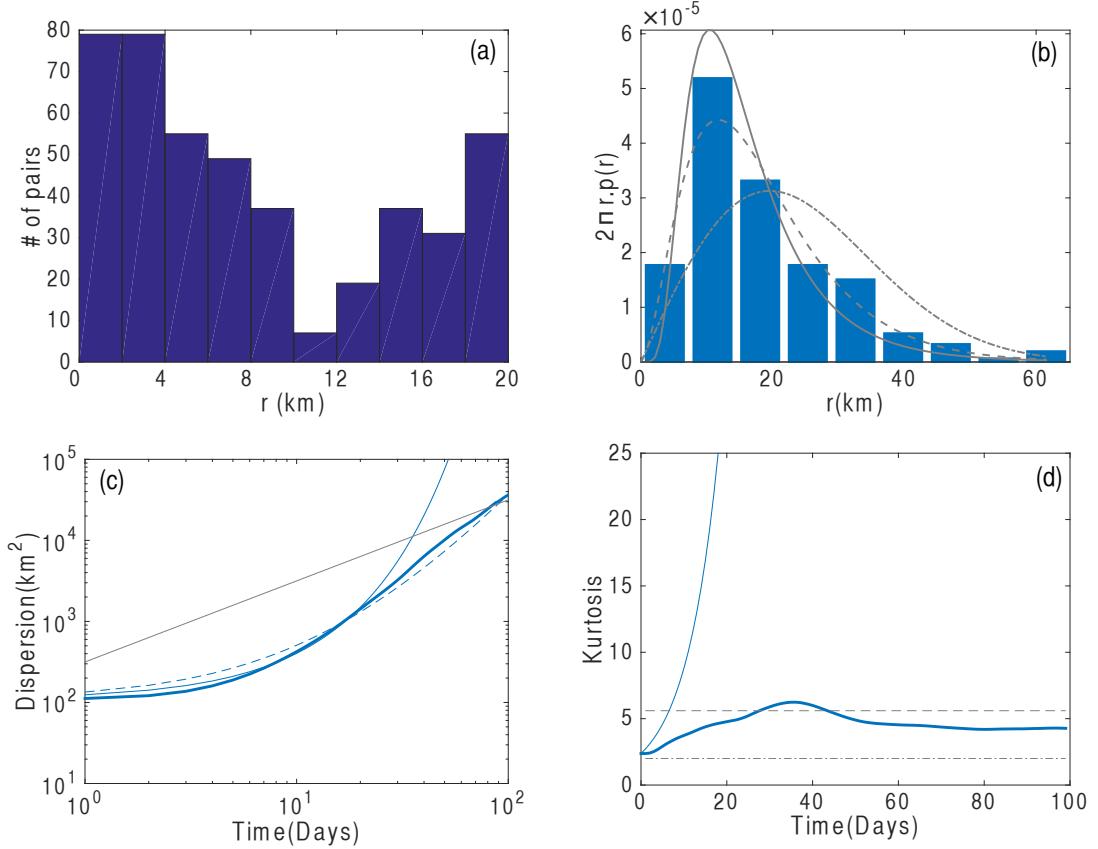
Figure 4.6: Temporal Statistics for model particle pairs selected to represent the initial separation distribution corresponding to RAFOS float pairs in the 1000 - 1800m bin. (a) Initial distribution of selected pairs. (b) The displacement PDFs at 10 days after deployment. The dashed, solid and dotted-dashed curves are the fitted Richardson, Lundgren and Rayleigh PDFs. (c) The relative dispersion (blue thick solid line). The theoretical fits, colored based on the depth, are shown as thin solid line for the Lundgren and dashed line for the Richardson dispersion. The gray line is the slope of 1 corresponding the Rayleigh dispersion (diffusive). (d) The kurtosis (thick solid lines) for the same, with the thin solid lines representing kurtosis for the fitted Lundgren curves. Dashed line at 5.6 corresponds to the asymptotic Richardson regime and dot-dashed at 2 corresponds to the Rayleigh regime.
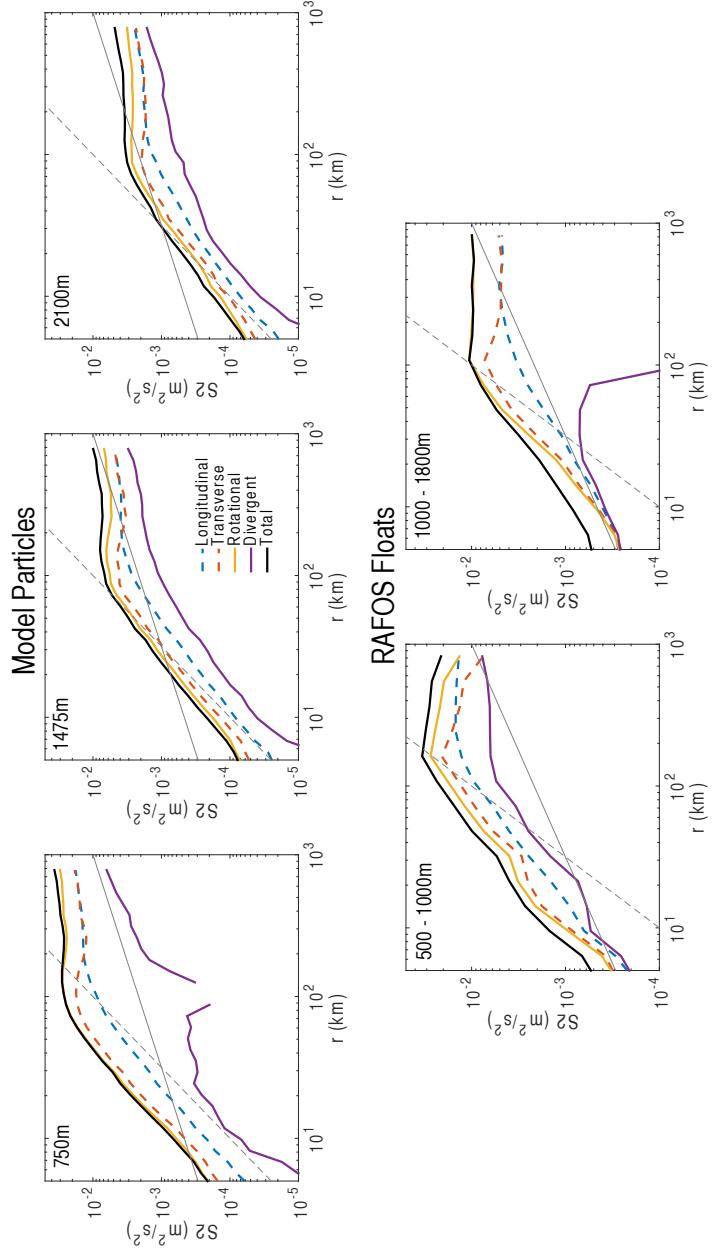
Figure 4.7: Second order structure function (S2, green) and its longitudinal (dashed blue), transverse (dashed red), rotational (yellow) and divergent (purple) components for the model particles and RAFOS floats. (a), (b) and (c) S2 and its components for model particles at 750, 1450 and 2100m. (d) and (e) S2 and its components the RAFOS floats in the depth bins of 500-1000m and 1000-1800m respectively. The dashed gray and solid gray line represent slopes of 2/3 and 2 corresponding to the energy and enstrophy cascade inertial range scalings. Note the difference in the extent of the Y axis for the model and observations.
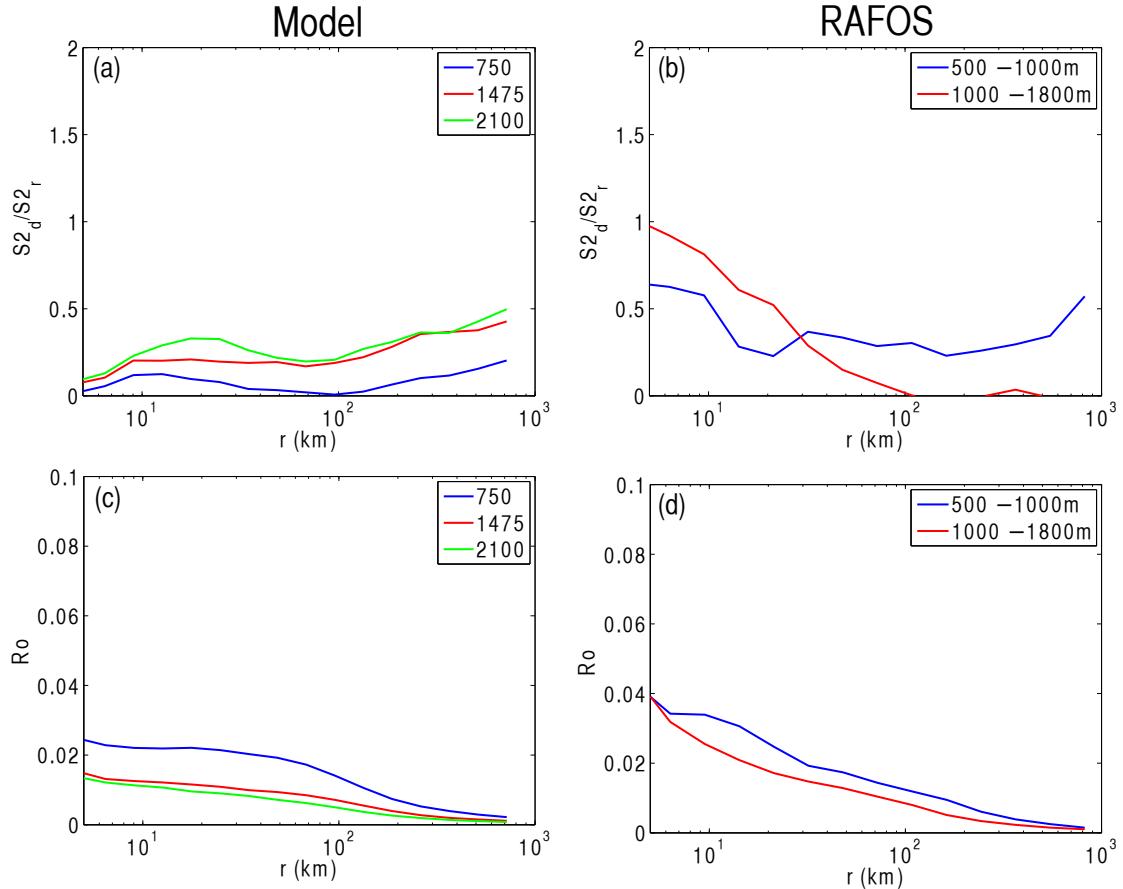
Figure 4.8: (a) and (b) Ratio of the divergent to rotational S2 for the model particles and RAFOS floats, colored corresponding to depth levels. (c) and (d) Rossby number ($\sqrt{S2}/fr$) calculated from S2 for the model particles and RAFOS floats, colored corresponding to depth levels.
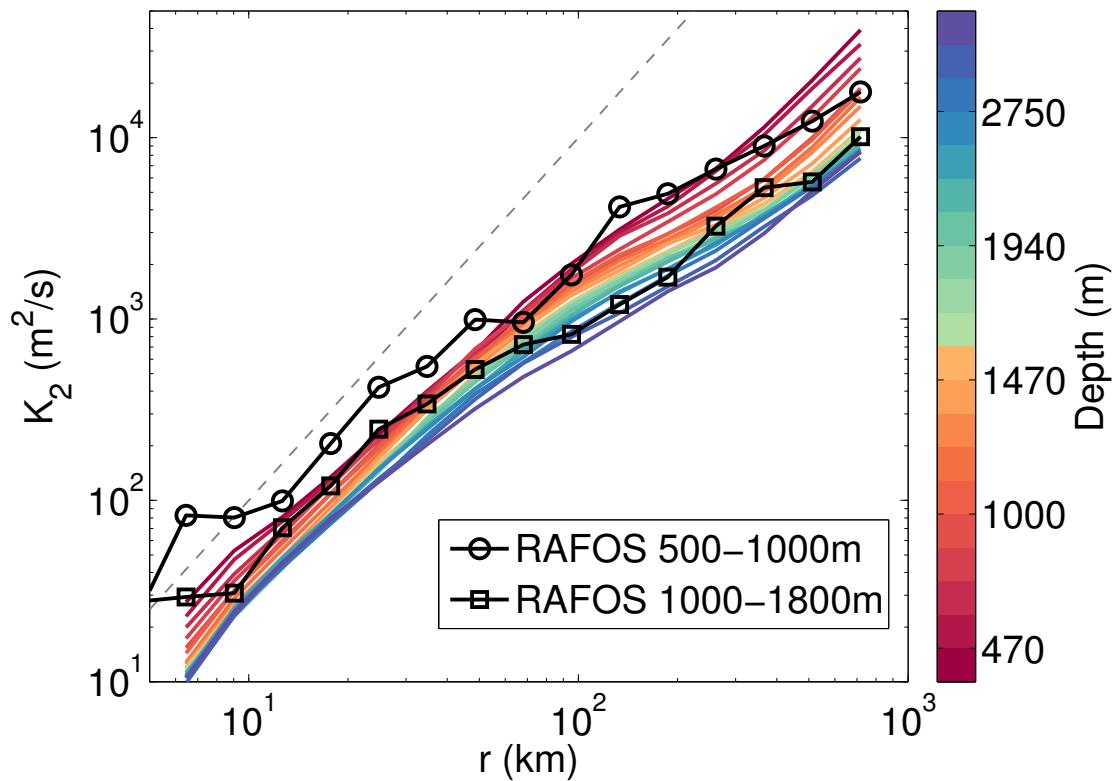
Figure 4.9: The relative diffusivity for the model particles (colored lines) and RAFOS floats (black lines) at different depths. The color bar indicates the depth level for the lines corresponding to the model particles.
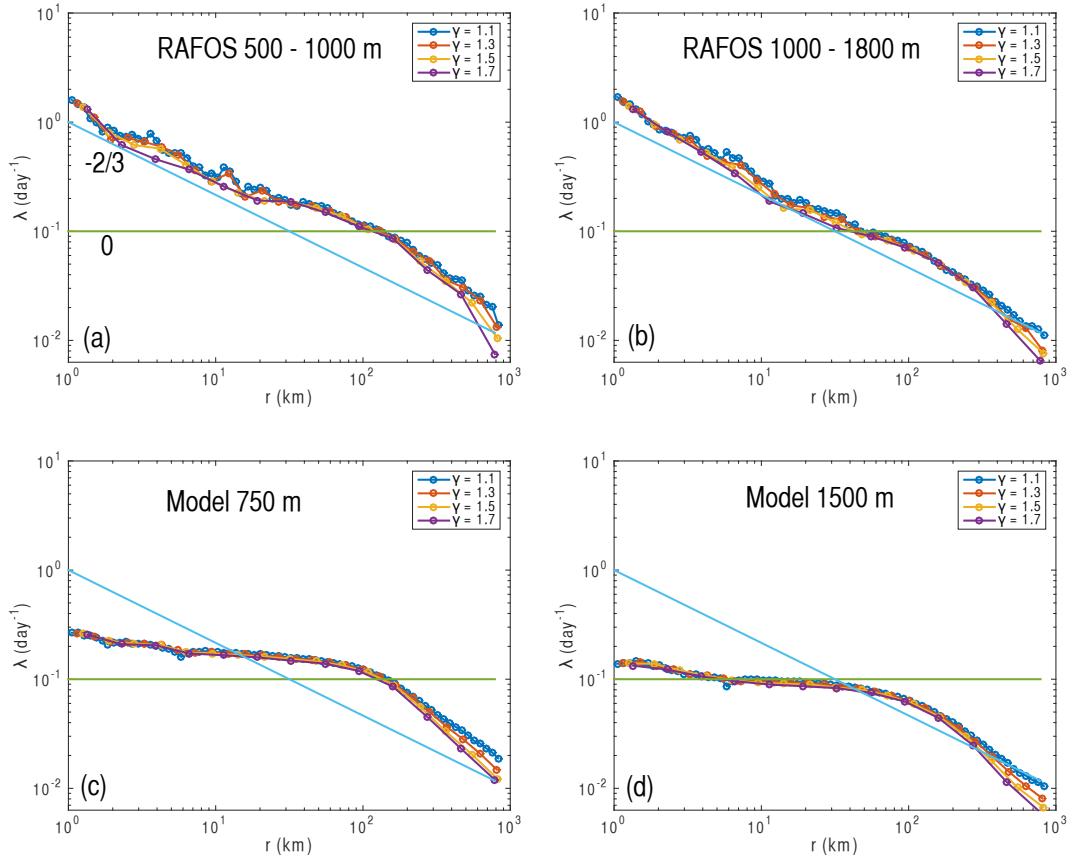
Figure 4.10: (a), (b) FSLE for the RAFOS floats in the shallow and deep depth bins respectively. Bottom (c), (d) FSLE for the model particles at 750 and 1500m. Solid blue and green lines correspond to slopes of -2/3 and 0, corresponding to Richardson and Lungdren dispersion. Different lines (marked as 'o-') correspond to different choices of bin sizes, as indicated in the legend.
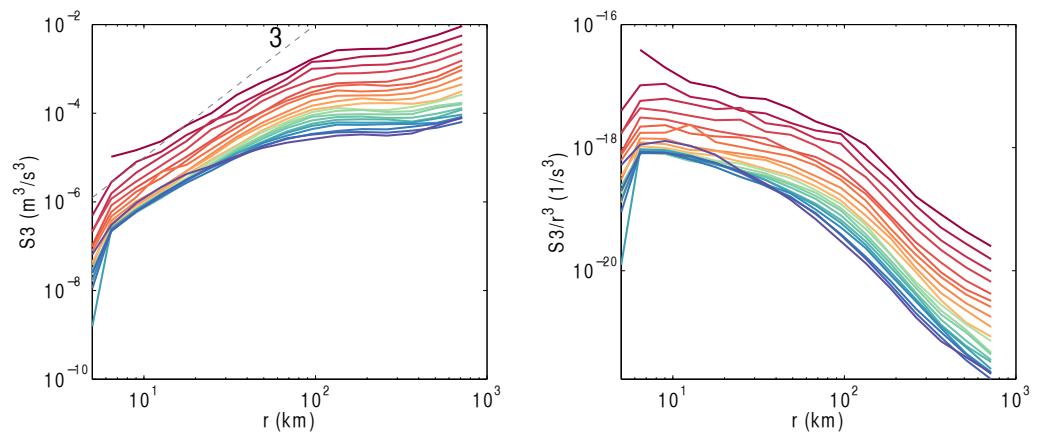
Figure 4.11: S3 (left) and the compensated S3 ($S3/r^3$) (right) at different depth from the model. Color corresponding to depth is the same as that from the colorbar in Fig. 4.9
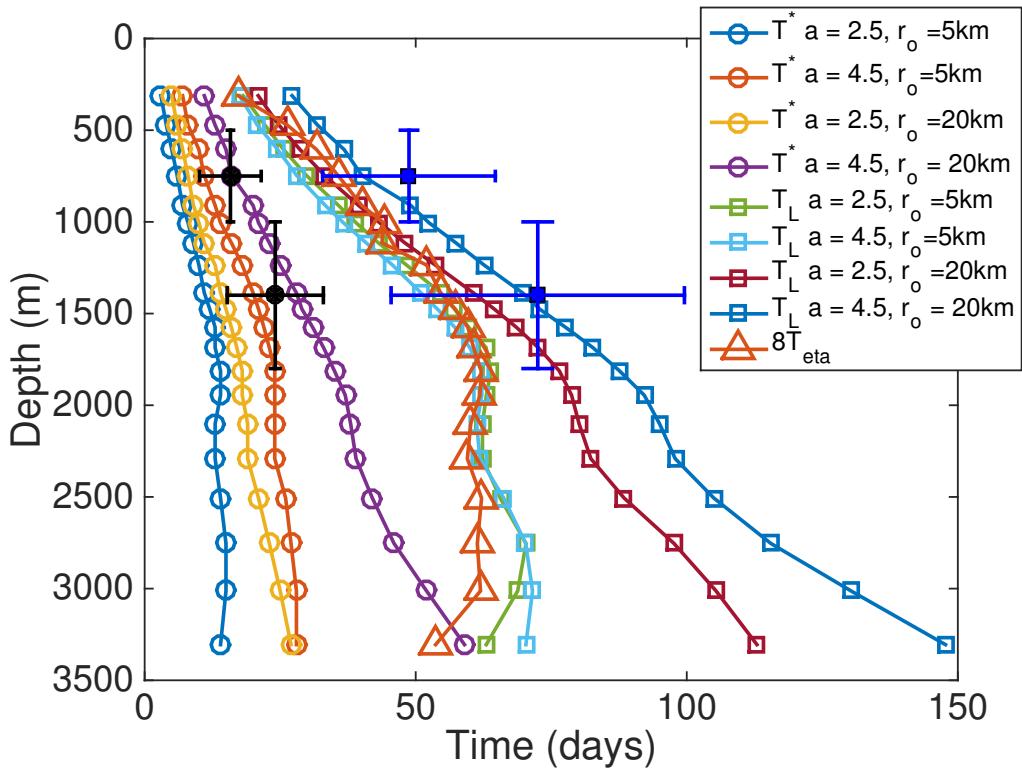
Figure 4.12: Time scales and their sensitivity to parameters. T^* is plotted as circle markers, T_L as square markers and $8T_\eta$ as triangle markers. Multiple T^* and T_L curves represent different choices of 'a' and r_o as shown in the legend. The blue and black markers with error bars are the T_L and T^* from the RAFOS floats.

CHAPTER 5

SCALE DEPENDENT DISTRIBUTION OF KINETIC ENERGY FROM SURFACE DRIFTERS IN THE GULF OF MEXICO

The scale dependent distribution of kinetic energy is probed at the surface in the Gulf of Mexico using surface drifters from the Grand Lagrangian Deployment (GLAD) experiment. The second order velocity structure function and its decomposition into rotational and divergent components are examined. The results reveal that the divergent component, compared to the rotational component, dominates at scales below 5 km, and the pattern is reversed at larger scales. The divergent component has a slope near 2/3 below 5 km, similar to an energy cascade range ($k^{-5/3}$). The third order velocity structure function at scales below 5km is negative and implies a forward cascade of energy to smaller scales. The rotational component has a steeper slope, roughly 1.5, from scales of 5km up to the deformation radius. This is similar to a 2D enstrophy cascade, although the slope is shallower than the predicted 2. There is a brief 2/3 range from the deformation radius to 200 km, suggestive of a 2D inverse cascade.

5.1   Introduction

Macroscopic turbulence in the atmosphere and the ocean is responsible for the fluxes of energy, enstrophy and tracer variance across scales. Knowing the nature of turbulence that is occurring indicates, for example, whether the energy is cascading towards larger or smaller scales. In the upper troposphere, the kinetic energy spectrum was calculated with startling clarity from velocity measurements via commercial aircraft (Gage and Nastrom (1986)). The results suggested a 2D turbulent cascade (of enstrophy) (Kraichnan (1967); Charney (1971)) from the baroclinic deformation radius, of order 2000 km in the atmosphere, down to several hundred kilometers. The kinetic energy spectrum was shallower at smaller scales, exhibiting the $k^{-5/3}$ slope expected for a turbu-

lent energy cascade, where k is the polar wavenumber. The nature of this latter range has been attributed to inertia-gravity waves (Callies et al. (2014)), stratified turbulence (Lindborg (2006, 2015)) and surface dynamics (Tulloch and Smith (2006)), and remains a subject of debate.

The ocean is more challenging in this regard, measuring the kinetic energy spectrum, because the deformation radius is smaller, typically 10-50 km (Chelton et al. (1998)). Thus gridded satellite data, with a typical resolution of 100 km, are unable to resolve sub-deformation scales (Stammer (1997)). Continuous shipboard current measurements using acoustic techniques (ADCP) have better resolution ($\sim$ 1-5 km). Studies using these ADCP data have given indications of an enstrophy range, as in the atmosphere, at length scales approximately between 30-100 km in different parts of the ocean (Wang et al. (2009); Callies and Ferrari (2013); Bühler et al. (2014); Rocha et al. (2015)), with some minor regional differences in scales. However, these analyses have also revealed that the dynamics between 5-30 km have a significant contribution from ageostrophic flows, and differ from predictions of traditional quasi-geostrophic dynamics. It should be noted, even using ADCP data, that the length scales (< 5 km) where the Rossby number, Ro, is order one are barely resolved.

GPS-tracked surface drifters on the other hand can resolve horizontal scales down to 10 m, in principle, two orders of magnitude finer than with shipboard ADCP. The present work builds on previous studies, which quantified the nature of the energy spectrum in the ocean, by using surface drifter data. A convenient diagnostic for use with drifter data is the second order velocity structure function ($D2$ hereafter), which is related to the energy spectrum and can be decomposed into rotational and divergent parts (Bühler et al. (2014); Callies et al. (2014); Lindborg (2015)). We also examine higher order velocity structure functions, to characterize other aspects of the turbulent behavior.

5.2   Methods

Structure functions are calculated from the velocities of pairs of drifters. We define the longitudinal velocity, the component along the separation vector $\mathbf{r} = \triangle x \hat{i} + \triangle y \hat{j}$ ($\triangle x = (x_2 - x_1)$ and $\triangle y = (y_2 - y_1)$ are the zonal and meridional components), as $\mathbf{u_l} = \frac{\mathbf{r \cdot u}}{|\mathbf{r}|}\hat{l}$ and the transverse velocity as $\mathbf{u_t} = \frac{(\mathbf{r \times u}) \cdot \hat{\mathbf{k}}}{|\mathbf{r}|}\hat{t}$ ($\hat{l}$ and $\hat{t}$ are unit vectors in the longitudinal and transverse directions respectively). The velocity difference between the drifters can be similarly projected.

Any velocity vector ($\mathbf{u}$) can be expressed as a sum of a rotational ($\mathbf{u_r}$) and a divergent ($\mathbf{u_d}$) component:

$$\mathbf{u} = \mathbf{u_r} + \mathbf{u_d} = -\nabla \times (\mathbf{k}\psi) + \nabla\phi, \tag{5.1}$$

where ∇ is the horizontal gradient operator, $\mathbf{k}$ is the vertical unit vector, ψ the stream function and ϕ the velocity potential (Bühler et al. (2014)). This (Helmholtz) decomposition is non-unique. However, assuming doubly periodic boundary conditions the stream function might differ at most by a constant, which does not affect the velocities.

The velocity structure functions are the moments of the velocity difference between the two drifters, $\delta\mathbf{u}$. $D2$, the mean of the squared difference, for homogeneous and isotropic flows is related to the kinetic energy spectrum via the Fourier transform (Bennett (1984)), and can be shown to be

$$D2(r) = 2 \int_0^\infty E(k)(1 - J_0(kr))dk, \tag{5.2}$$

where $E(k)$ is the energy spectrum, $J_0(kr)$ is the zeroth order Bessel function, r is the separation and k is the polar wavenumber. Using the asymptotic limits of $(1 - J_0(kr))$,

$$\frac{1}{4}D2(r) \approx \frac{r^2}{4} \int_0^{2/r} k^2 E(k)dk + \int_{2/r}^\infty E(k)dk. \tag{5.3}$$

This relationship reveals the physical significance of $D2$ and its relation to the spectrum. The $D2(r)$ is a cumulative quantity that sums the energy of eddies that are smaller than $\pi r/2$ and the enstrophy of the eddies that are larger than $\pi r/2$. This can be physically understood as - the eddies that are smaller than the separation distance contribute their kinetic energy to the $D2$, while the eddies that are larger than separation distance contribute through their imposed velocity gradient to $D2$ (Davidson and Pearson (2005); Davidson (2015)).

$D2(r)$ also can be separated into components, $D2_l = \delta u_l^2$ and $D2_t = \delta u_t^2$. Scaling arguments, such as those applied for the kinetic energy spectrum in the turbulent inertial ranges, apply here as well: $D2_t \sim D2_l \sim r^m$ if $E_l \sim E_t \sim k^{-(m+1)}$, provided that $m + 1 \leq 3$ (e.g. Babiano et al. (1985); Bennett (1984); Lindborg (2007)). Also, the length scale where different components of $D2(r)$ intersect, indicating the length scale where the different flow components (longitudinal and transverse or rotational and divergent) exchange dominance, provides a reasonable approximation

to the length scale where the corresponding components of $E(k)$ intersect for the results presented in this study. This is discussed further in the supplementary text.

Under certain conditions, the transverse and longitudinal structure functions are related (Lindborg (2007)). For purely rotational 2D flow (horizontally non-divergent), the incompressibility condition yields

$$D2_t = \frac{d}{dr}(rD2_l). \tag{5.4}$$

For potential flow (horizontally irrotational), the condition of zero curl yields

$$D2_l = \frac{d}{dr}(rD2_t). \tag{5.5}$$

Thus if the second order velocity structure function exhibits a power law dependence, $D2_t \sim D2_l \sim r^m$, the above relations imply the ratio $D2_t/D2_l = m+1$ for a purely rotational flow and $D2_l/D2_t = m+1$ for a purely divergent flow (Lindborg (1999); Bühler et al. (2014)).

If the rotational and divergent components are uncorrelated, the second order velocity structure function is simply their sum (Lindborg (2015)). This equals the sum of the functions based on the rotational and divergent velocities as well, as

$$D2 = D2_l + D2_t = D2_r + D2_d. \tag{5.6}$$

Under the assumptions of homogeneity, isotropy and the uncorrelated components, the following expressions are obtained:

$$D2_r = D2_t + \int_0^r \frac{1}{r}(D2_t - D2_l)dr, \tag{5.7}$$

and

$$D2_d = D2_l - \int_0^r \frac{1}{r}(D2_t - D2_l)dr. \tag{5.8}$$

Higher order velocity structure functions can also be calculated, and these can reveal more about the turbulence. The third order velocity structure function, defined $D3_l =< \delta u_l \delta \mathbf{u}.\delta \mathbf{u} >$, is related to the spectral energy or enstrophy flux (Frisch (1995); Lindborg and Cho (2001)). The sign in particular, if the $D3_l$ is linear, reflects the direction of energy transfer, either up or downscale. The fourth order velocity structure function is often written as a kurtosis, e.g. $F_l = \frac{<\delta u_l^4>}{<\delta u_l^2>^2}$ for

the longitudinal component. This indicates the degree of non-Gaussianity or intermittency as a function of scale.

5.3 Dynamical Expectations

Kolmogorov used velocity structure functions in developing his theory for 3D turbulence at high Reynolds numbers (Kolmogorov (1941); Frisch (1995)). With a constant flux of energy across scales, ϵ, the second order velocity structure function scales as $D2 \propto \epsilon^{2/3} r^{2/3}$, Kolmogorov's '2/3 Law'. The same dependence applies to an inverse energy cascade in 2D turbulence. He also showed that the third order longitudinal velocity structure function, $D3_l$, equals $-4/5\epsilon r$, an exact result (his '4/5 Law'). The function equals $-2\epsilon r$ in a quasi-2D forward energy range (Lindborg and Cho (2001)) and $2\epsilon r$ in the 2D inverse energy range (Lindborg (1999)), where ϵ is a positive quantity and a positive/negative $D3_l$ indicates an upscale/downscale energy transfer. In a 2D enstrophy cascade, the scaling is instead $D2 \propto \eta^{2/3} r^2$, where η is the enstrophy flux (e.g. Lindborg, 1999; LaCasce, 2002). The third order longitudinal function in this case equals $1/4\eta r^3$ (Lindborg (1999)).

There are of course other possibilities at the ocean surface. Under surface quasi-geostrophy (SQG), there are also two inertial ranges, one for total energy and one for temperature variance (Held et al. (1995)). There are claims that the latter occurs at the ocean surface ((e.g. Le Traon et al., 2008)), but observational evidence is currently lacking (Callies and Ferrari (2013); Rocha et al. (2015)). The energy spectrum is the same as in an energy cascade and also yields an $r^{2/3}$ dependence for $D2$. A similar spectral slope is seen in the high wavenumber range of the empirical Garret and Munk spectrum, with energy cascading downscale due to wave-wave interactions (Garrett and Munk (1972)). Other possibilities exist, due for example to frontal processes, inertial oscillations and Langmuir turbulence (Thomas et al. (2008)). Thus it is not clear a priori that a single scaling regime should apply.

5.4 Results

The trajectories of the GLAD drifters are shown in Figure 5.1. These lie in the northeastern Gulf of Mexico and span the period from July-October in 2012. The drifters were launched in clusters, with a minimum initial separation of 100 m (Poje et al. (2014)). However smaller separations or "chance pairs" (Morel and Larceveque (1974); LaCasce and Ohlmann (2003)) also occurred.

The Lagrangian kinetic energy frequency spectrum, shown in the insert in Figure 5.1, has a typical shape: flat at low frequencies and decreasing as ω^{-2} at high (Rupolo et al. (1996); LaCasce (2008)). A significant inertial peak is also seen, clearly visible as anticyclonic loops in the trajectories.

The structure functions were averaged using distance bins with a size distribution given by $r_k = 0.1 \times 1.4^k$ m, yielding equal spacing on a logarithmic scale. The smallest bin, at 10m separation, has more than 5000 velocity estimates, and there are more than 10^7 at 200 km. The nominal position and velocity errors are expected to be 10 m and 3 cm/s respectively, which result from errors in GPS positioning along with interpolation and smoothing operations that are used to obtain the 15 min resolution. A detailed account of these position and velocity errors can be found in the metadata provided with the data set. Random errors on the second order velocity structure functions are extremely small (Figure S1) and thus provide us confidence in the results. The random errors are greater for the third order velocity structure function, as it is not an average of a sign definite quantity, but they do not obscure the key qualitative results presented here.

The longitudinal and transverse pair velocity correlations (not shown) suggest strongly correlated motion up to separations of 50 km, as noted previously by (Beron-Vera and LaCasce (2016)). Pairs with separations exceeding 100 km display uncorrelated motion. $D2$ has a slope near 2/3 up to about 200 km (Fig. 5.2a), also noted previously (Poje et al., 2014; Beron-Vera and LaCasce, 2016). At larger scales $D2$ flattens out, as the pair velocity correlation goes to zero ($D2 = <\boldsymbol{\delta u}^2> = 2<|\mathbf{u}|^2> -2<\mathbf{u_1} \cdot \mathbf{u_2}>$).

The different components of $D2$ are also shown in Fig. 5.2a. Most conspicuously, the rotational and divergent components cross at roughly 5 km separation, with the divergent component dominating at smaller scales and the rotational component at larger. Likewise, the transverse and longitudinal velocity structure functions cross near this scale, with the transverse component dominating at large scales and the longitudinal component being somewhat larger at small scales. The Rossby number can be estimated as $Ro = \sqrt{D2_l + D2_t}/(fr)$, where f is the Coriolis parameter and r the separation. The transition scale is approximately where the Ro is unity (Fig. 5.2b). Ro is smaller at larger scales, indicating the flow is nearer to geostrophic balance, and hence rotational (Pedlosky (1987)).

At small scales, the divergent velocity structure function, $D2_d$, has a slope near 2/3, as expected for an energy range. This essentially determines the slope of the total function, $D2$. Further, the ratio of the transverse and longitudinal velocity structure functions is close to 3/5 (Fig. 5.2b), as expected for a divergent flow with a slope of 2/3.

From 5 - 50 km, the rotational velocity structure function is greater. Below roughly 30 km, this has a slope of 1.5. The steeper $D2_r$ accounts for the steepening in $D2$ seen above 5 km. The deformation radius, L_d, in the Gulf of Mexico is near 45 km (Chelton et al. (1998)), so the rotational velocity structure function resembles that for an enstrophy cascade below L_d, but has a shallower slope than 2. The ratio $D2_t/D2_l$ increases rapidly in the range of 5-50km to a value of 2.2 (the theoretical value for an enstrophy cascade is 3 with a slope of 2 for the velocity structure function).

Between 40 - 100km, $D2$ essentially reflects $D2_r$. The slope in this range is near 2/3, suggestive of a 2D inverse energy cascade. However, the range of scales is small. The ratio $D2_t/D2_l$ is falling but is obviously not constant (Fig. 5.2b).

The higher order moments provide additional insight. The longitudinal third order velocity structure function, $D3_l$, increases approximately linearly over all scales below 200 km (Fig. 5.3). A linear slope is expected in an energy cascade (sec. 5.3). $D3_l$ is positive at the larger scales, but changes sign at 2 km. The negative, linear dependence at small scales implies a forward energy cascade. A similar result was obtained previously with atmospheric data, below 100 km, by Cho and Lindborg (2001). The implied dissipation rate, $\epsilon = D3_l/(2r)$ with the sign signifying the direction, is shown in the insert in Fig. (5.3). Below 2 km the value is approximately $5 \times 10^{-8} m^2/s^3$ and negative, which is in line with estimates of energy dissipation rate based on microstructure measurements in the near surface ocean (Moum and Smyth (2001)).

The positive, linear $D3_l$, seen here at the larger scales, would imply an upscale transfer in an energy cascade. However as the divergent and rotational components are both present in the range of 2-20 km, the result probably represents a combination of the positive, cubic behavior expected in an enstrophy range (sec. 5.3) with the negative contribution from the divergent motions. Above 20 km the third order function increases faster than linear, but the range of scales is too small to make definite conclusions.

The longitudinal and transverse kurtoses are shown in orange in Fig. (5.3). The two are consistent in that the small scales are non-Gaussian while the scales above L_d are nearer Gaussian.

However the transition scale differs slightly for the two, occurring near 5 km for the transverse function and 20 km for the longitudinal. The kurtosis is expected to be non-Gaussian in either an energy or enstrophy range and Gaussian at scales where the pair motion is uncorrelated, so we expect the transition to occur instead at 50 - 100 km. Why this transition occurs at smaller scales is unclear.

Homogeneity and isotropy are essential for the turbulence scaling laws and the Helmholtz decomposition to hold. However, these assumptions are rarely, if ever, perfectly satisfied in the ocean. To test the validity of these assumptions we performed a binned statistical analysis on the GLAD data. This analysis showed a higher kinetic energy away from the boundaries, presumably a result of the loop current eddies (Figure S2). The variance ellipses did not show any coherent patterns and suggested the flow variability is primarily isotropic. We repeated the analysis on smaller sections by dividing the data according to geographical region (Figure S3 and S4). The results from the more energetic regions indicated a slightly steeper $D2$ and $D2_r$ in the 5 - 50 km range, with the ratio $D2_t/D2_l$ peaking at 3. Also, the cross over of $D2_r$ and $D2_d$ happened at a smaller separation scale ($\sim$1 km, Figure S4).

To assess the extent to which inertial and super-inertial motions contribute to the structure functions we repeated the analysis on frequency filtered Lagrangian velocity and position time series from the GLAD data (Figure S5 and S6). As Lagrangian measurements mix temporal and spatial information, filtering only in the frequency domain is not ideal. Also, it is not clear if the filtering should be performed only on the velocity time series or on both the velocity and position time series. This choice should mostly effect the results in the smaller separation bins, where the spatial resolution is finer, as the velocity difference samples are redistributed in separation bins due to filtering of the position time series. Due to these caveats, the results of the filtering should be viewed as suggestive rather than definitive. Removing only the inertial energy resulted in a small reduction of the divergent component below 10km. However, it increased the contribution of the rotational component at length scales smaller than 5 km, which is likely a filtering artifact. Removing both the inertial and super-inertial energy led to a significant reduction in the divergent component below 10 km, a slight steepening of the rotational component in the 5 - 50 km range, aligning it more with the predictions for an enstrophy cascade, and a disappearance of the negative linear $D3_l$ range between 100 m - 2 km . These results suggest that the super inertial divergent

motions might be strong contributors to the forward energy cascade, and can also potentially contaminate the scaling behavior at the length scales of the enstrophy cascade. Choosing to only filter the velocity time series produced similar results (not shown).

5.5   Summary and Discussion

We have examined a Helmholtz decomposition of the second order velocity structure function into rotational and divergent components, following (Bühler et al., 2014; Lindborg, 2015), using velocities from surface drifters deployed in the GLAD experiment (Poje et al. (2014)). This is the first such decomposition applied to Lagrangian data, and the smallest sampled scale, 10 m, is two orders of magnitude below that sampled in comparable ADCP studies (Callies et al. (2014)).

The results reveal that the rotational component dominates at scales above 5 km and the divergent component below. The Rossby number is approximately 1 at 1 km, so the divergent component emerges when Ro is order 1 or larger. The divergent component has a slope near 2/3 below 5 km, similar to an inertial energy range spectrum. The third order velocity structure function is negative at these scales, implying a downscale cascade of energy.

The rotational velocity structure function has a steeper slope, roughly 1.5, from scales of 5 km up to the deformation radius. This is similar to a 2D enstrophy cascade, although the slope is shallower than the predicted 2 for an inertial range of infinite extent. From L_d to 200 km, there is a brief 2/3 range, suggestive of a 2D inverse energy cascade.

The results are reminiscent of those from the upper troposphere, where there is an enstrophy cascade from 2000 km down to several hundred kilometers, and a transition to a shallower kinetic energy spectrum where $Ro \approx 1$ (Nastrom and Gage (1985)). Callies et al. (2014) used the MOZAIC data to show that the rotational energy spectrum dominates at the large scales near the tropopause, while the rotational and divergent components are nearly equal at the small scales. Structure functions, calculated with the same data, also show equal contributions at small scales, at least in the lower stratosphere, and a weaker divergent component in the upper troposphere across all scales (Lindborg (2015)).

In the present analysis, the rotational component is also greater at large scales, but the divergent component clearly dominates at small scales. A possible candidate for this large divergent contribution is inertial oscillations, which are are often significant in the ocean mixed layer and

are prominent in the GLAD data (Beron-Vera and LaCasce (2016)). Other candidates also exist, such as tidal motion (Chavanne and Klein (2010)) and wind forced surface flows, and have similar frequencies. However, it is difficult to test exactly which candidates dominate the divergent contribution with the current data set. In the future, drifters that measure buoyancy could provide greater insight via the buoyancy structure functions.

The second order velocity structure function integrates across the energy spectrum and hence raises the question if the much greater divergent component seen in this study, when compared to the atmospheric literature, stems from the difference between spectra and structure functions. One can in principle calculate the spectra from the structure functions directly, however this conversion is complicated by contributions from large scales, which are typically noisy with Lagrangian data (LaCasce (submitted)), and does not produce meaningful results (not shown). Nevertheless, when the divergent spectrum is less than the rotational spectrum at large scales and equal at small scales, as in the atmospheric cases, the divergent structure function cannot exceed the rotational structure function. Thus the present results imply that the divergent spectra actually do exceed the rotational spectra at small scales, again pointing to differences in the dynamics at smaller scales.

Studies in the Drake Passage and the Gulf Stream using ADCP data (Bühler et al. (2014); Callies and Ferrari (2013); Rocha et al. (2015)) observe a k^{-3} kinetic energy spectrum, transitioning to k^{-2} at smaller length scales. A Helmholtz decomposition suggested roughly equal contributions from the divergent and rotational components at approximately 10 km in the Gulf Stream and 50 km in the Drake Passage. These studies show a wider range of scales over which a k^{-3} kinetic energy spectrum is observed, compared to the results presented here. The scales where the divergent components exceeded the rotational component were not resolved due to coarser resolution (1 - 5 km) of the ADCP data. Bühler et al. (2014) also show that in the eastern Subtropical North Pacific, which is less energetic than the Gulf Stream, the energy spectrum is closer to k^{-2} at all length scales smaller than 100 km, with no k^{-3} range.

Further work remains to be done, for instance to illuminate the nature of the divergence-dominated regime and to test for seasonal variations (e.g. Callies et al., 2015). But the results of the present study shows that drifters can be used to deduce important aspects of the turbulent dynamics at lateral scales far below those sampled with most other instruments.
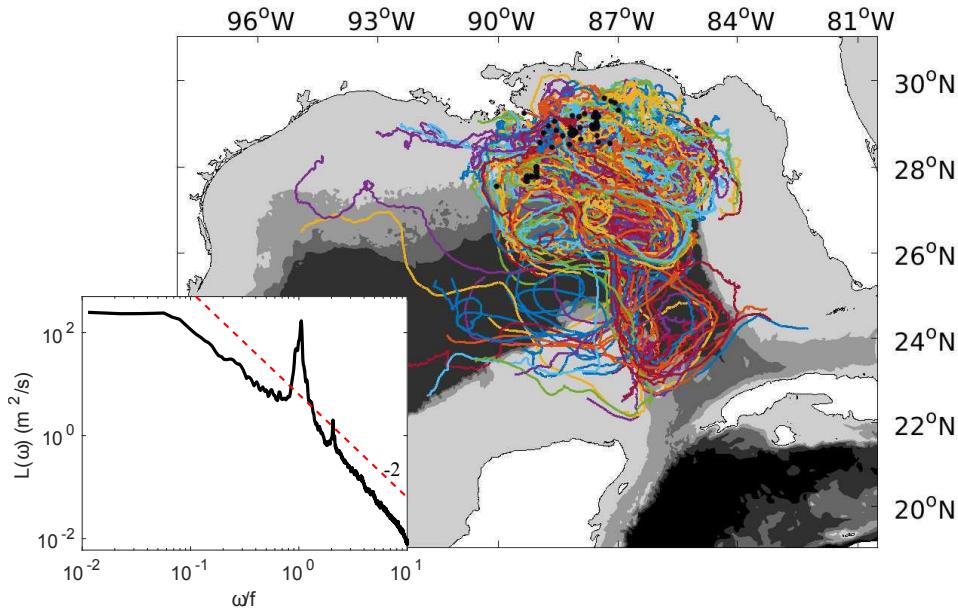
Figure 5.1: Surface drifter trajectories from Grand Lagrangian Deployment (GLAD) experiment conducted in 2012, where each colored line represents a single trajectory and the black dots represent the deployment locations. Contour shading represents bathymetry between 0-5000m, contour intervals of 1000m. Bottom left inset shows the averaged Lagrangian kinetic energy frequency spectrum of the velocity time series from these surface drifters. Dashed red line represents power law behavior of ω^{-2}.
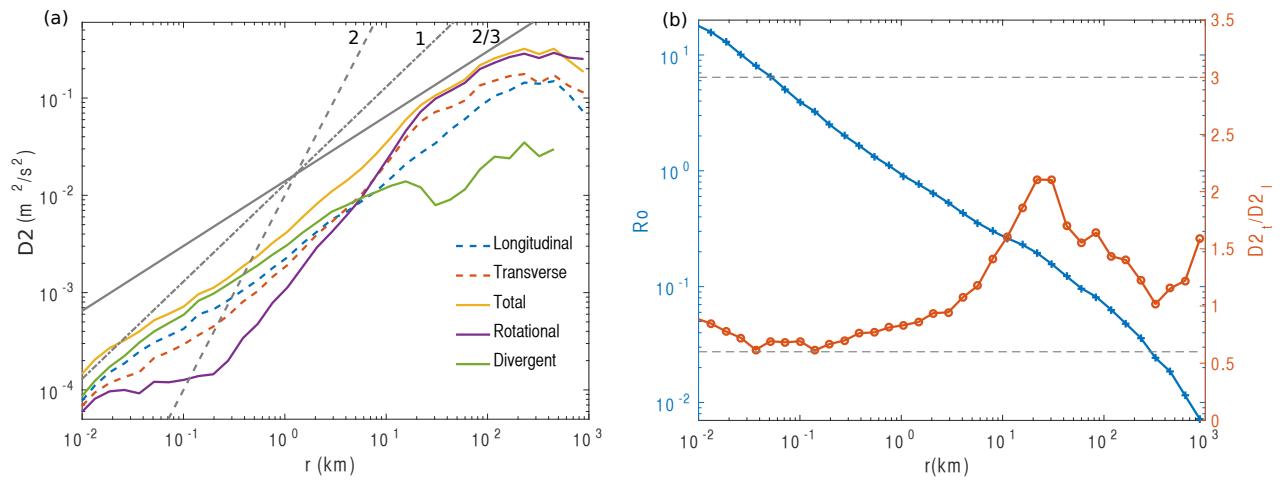
Figure 5.2: (a) Different components of the second order velocity structure functions. Three power law relationships are plotted as gray lines with slopes marked on the top. (b) Left axis, blue, shows the Rossby number defined as $\sqrt{D2}/(fr)$, where f is the Coriolis parameter and r is the separation distance. Right axis, orange, shows the ratio of the transverse to longitudinal second order velocity structure function ($D2_t/D2_l$).
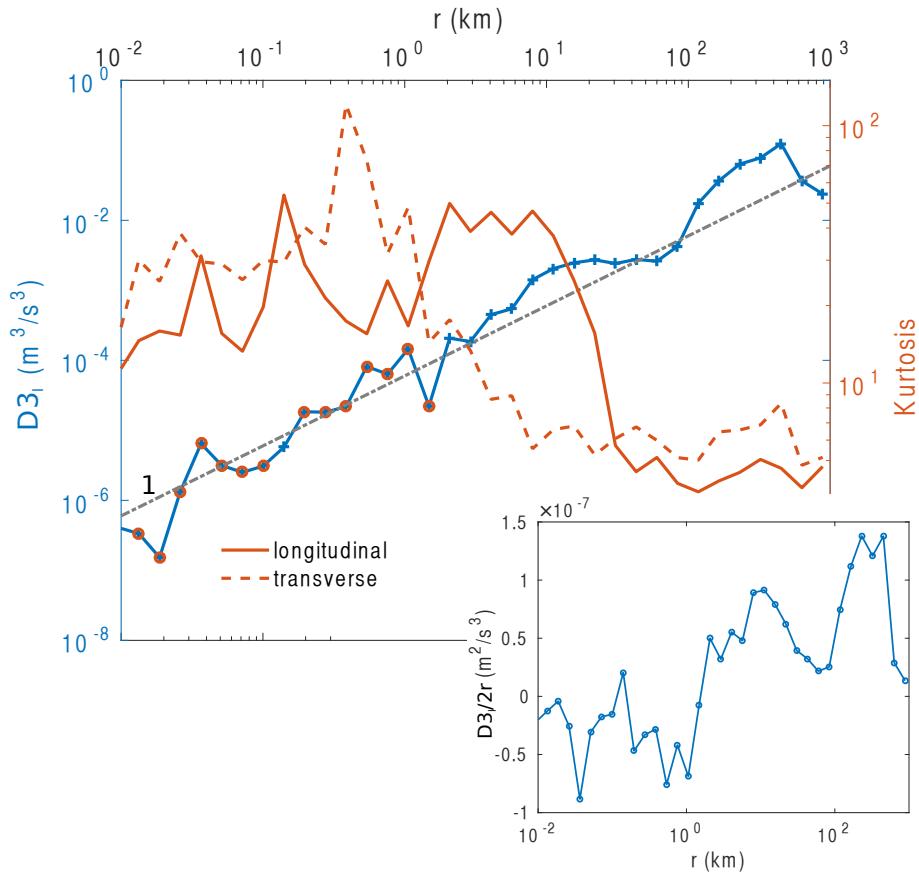
Figure 5.3: Absolute value of the longitudinal component of the third order velocity structure function ($D3_l$) on the left axis (blue axis and line). Orange circles and blue pluses represent negative and positive values, respectively. A linear power law relationship is shown as dashed gray line. Kurtosis ($\frac{<\delta u^4>}{<\delta u^2>^2}$), both longitudinal and transverse components, is shown in orange on the right axis. Inset on bottom right shows the relation $D3_l/2r$.

5.6   Supplementary Material

5.6.1   Relationship Between the Second Order Structure Function and the Energy Density

In this appendix we discuss how the cross over length scale of two components of the kinetic energy spectrum, say the divergent and rotational components, are related to the cross over length scale of the corresponding second order velocity structure functions, where the cross over length scale is defined as the length scale where two components intersect and exchange dominance. As the energy spectrum represents the energy density as a function of length scales, it is beneficial to know the cross over length scale for the divergent and rotational components of the energy spectrum. We also provide a complementary discussion in terms of signature functions, which are the real space alternative to the energy spectra.

The second order velocity structure function can be related to the 2D isotropic energy spectrum as

$$D2_{ii}(r) = 4 \int_0^\infty E_{ii}(k)(1 - J_0(kr))dk \tag{5.9}$$

$$E_{ii}(k) = \int_0^\infty \frac{D2_{ii}(\infty) - D2_{ii}(r)}{4} J_0(kr)krdr, \tag{5.10}$$

and to the 1D isotropic energy spectrum as

$$D2_{ii}(r) = 4 \int_0^\infty E_{ii}(k)(1 - cos(kr))dk \tag{5.11}$$

$$E_{ii}(k) = \frac{1}{2\pi} \int_0^\infty (D2_{ii}(\infty) - D2_{ii}(r))cos(kr)dr. \tag{5.12}$$

Subscript ii does not imply summation here. These relationships have been derived previously in Babiano et al 1985, Bennett 1985 and LaCasce 2016. LaCasce 2016 also showed that the transform of the energy spectrum to the structure function is straight forward and well behaved for both idealized and observational data. However, the inverse transform is sensitive to the details at large separations and produces very noisy results. We attempted to transform the GLAD structure functions to the corresponding energy spectrum, but were unsuccessful in producing any meaningful results.

Due to the integral nature of the relationship between the structure function and the energy spectrum, the cross over length scales observed using the second order velocity structure function and the energy spectrum would be different. However, as shown below for an idealized scenario, the difference might be minor for some cases.

We consider an idealized power law spectrum

$$E_\alpha(k) = C_\alpha(k/k_o)^{-\alpha}, \tag{5.13}$$

with a finite range $k_o < k < k_1$, where k_o and k_1 are the lower and higher wave number cutoffs.

This energy spectrum can be transformed to the corresponding structure functions using equation 1. Here, we use an approximation to equation 1,

$$D2(r) \approx 4(\frac{r^2}{4} \int_0^{2/r} k^2 E(k)dk + \int_{2/r}^\infty E(k)dk), \tag{5.14}$$

however the results are not sensitive to this choice.

This approximate can be easily integrated with the above choice of $E_\alpha(k)$ and results in

$$D2_\alpha(r) = \frac{C_\alpha k_o^\alpha}{(3-\alpha)} r^2 k^{3-\alpha}|_{k_o}^{2/r} + 4\frac{C_\alpha k_o^\alpha}{1-\alpha} k^{1-\alpha}|_{2/r}^{k_1}. \tag{5.15}$$

Two energy spectra (E_α and E_β) with different slopes intersect at the wavenumber $k_i = k_o(C_\alpha/C_\beta)^{1/(\alpha-\beta)}$, and a corresponding length scale that can be defined as π/k_i. The intersection length scale (r_i) for the corresponding second order velocity structure functions ($D2_\alpha(r)$ and $D2_\beta(r)$) can found numerically by finding the roots to $D2_\alpha(r) - D2_\beta(r) = 0$.

An idealized case was considered with a fixed α of 5/3, representing the divergent component, and β that is varied from 5/3 to 3, representing a range of slopes for the rotational component. The wavenumber where the two spectra intersect was also varied from k_o to k_1. The ratio of the two cross over length scales ($\pi/(k_i r_i)$) is generally order 1, as shown in Figure S7. Thus, for idealized scenarios where the structure functions or energy spectrum follow the same power law behavior over a range of scales, the cross over length scale determined from either measure are similar. This might be applicable to the GLAD results, where the rotational and divergent component seem to have a constant power law behavior over 100m - 10km range of scales.

Davidson and Pearson 2005 define a real space alternative to the energy spectrum, the "signature function". For 2D (not necessarily non-divergent) isotropic flows the signature function is defined

as

$$V(r) = \frac{-r^2}{4} \frac{\partial}{\partial r} \frac{1}{r} \frac{\partial D2(r)}{\partial r}. \tag{5.16}$$

Calculating signature functions for a given second order velocity structure function is straight-forward, but the estimate can be very noisy for observations due to the additional derivatives in the definition of the signature function. In Figure S8, we present a smoothed version of second order velocity structure functions from the GLAD drifter data and the corresponding signature functions ($rV(r)$ is the measure of energy density). The smoothing shifts the cross over length scale for the structure functions to a slightly smaller length scale (~ 2 km), compared to the original structure function estimates (Figure 2, main text). The estimated signature function is noisy, but indicates a cross over length scale that is similar to the one seen using the structure functions.

Thus, signature functions support the earlier result using idealized energy spectra, the second order velocity structure functions potentially provide a length scale at which the energy density of divergent and rotational flows exchange dominance.

Finally, even though these results indicate that the cross over length scales are comparable in this study, this might not always be the case (Callies et al 2016). If possible, investigators should calculate both the energy spectrum and structure functions before drawing conclusions.

5.6.2 Derivation of the Relationship Between Structure Functions and Energy Spectrum

The relationship between the second order structure function and the energy spectrum have previously been explored and documented, e.g. Batchelor (1953); Babiano et al. (1985); LaCasce (submitted). Here a summary is provided for completeness.

Consider the velocity vector $\mathbf{u}(\mathbf{x}) = u_i(x, y)\hat{i} + u_j(x, y)\hat{j}$, where i, j are two orthogonal directions, such as zonal and meridional or longitudinal and transverse. A spatial correlation function, between two points $\mathbf{x_1}, \mathbf{x_2}$, is defined as

$$Q_{ij}(\mathbf{x_1}, \mathbf{x_2}) = < u_i(\mathbf{x_1}) u_j(\mathbf{x_2}) > . \tag{5.17}$$

$< . >$ implies an ensemble averaging, over multiple realizations of the experiment. For a **homogeneous** flow field the individual locations $\mathbf{x_1}, \mathbf{x_2}$ are irrelevant, and only the position vector joining the two points $\mathbf{r} = \mathbf{x_1} - \mathbf{x_2} = x\hat{i} + y\hat{j} = r\hat{r} + \theta\hat{\theta}$ is significant. Under this assumption the

averaging operator also encompasses spatial averaging. Further, under the assumption of **isotropy**, only the separation distance $r = |\mathbf{r}|$ is the independent variable effecting $Q_{ij}(r)$ and the averaging is over both space and direction.

The 2D second order structure function for a homogeneous field is defined as

$$S_{ij}(\mathbf{r}) = < u_i(\mathbf{x}) - u_j(\mathbf{x} + \mathbf{r}) > . \tag{5.18}$$

For an isotropic field this can be averaged over all directions and we obtain the 1D second order structure function,

$$S_{ij}(r) = \frac{1}{2\pi} \int_0^{2\pi} S_{ij}(\mathbf{r}) d\theta \tag{5.19}$$

A collection of Lagrangian particles, by default, measure the 2D $S_{ij}(\mathbf{r})$ and on averaging over all possible orientations provide the 1D $S_{ij}(r)$. For an isotropic system the distance r is the only influence and the averaging over all angles has no effect on $S_{ij}(\mathbf{r})$, $S_{ij}(\mathbf{r}) = S_{ij}(r)$. If measurements are available only on a single line, such as with ADCP data, and isotropy holds, then one directly measure the 1D $S_{ij}(r)$.

The 2D Fourier transform of the spatial correlation function is defined as

$$\begin{aligned}
\hat{Q}_{ij}(\mathbf{k}) &= \frac{1}{(2\pi)^2} \int_{-\infty}^{\infty} \int_{-\infty}^{\infty} Q_{ij}(\mathbf{r}) e^{-i\mathbf{k}.\mathbf{r}} dx dy \\
&= \frac{1}{2\pi} \int_{-\infty}^{\infty} \check{Q}_{ij}(x, l) e^{-ikx} dx \\
&= \frac{1}{2\pi} \int_{-\infty}^{\infty} \check{Q}_{ij}(k, y) e^{-ily} dy,
\end{aligned} \tag{5.20}$$

where $\mathbf{k} = (k, l)$ is wavenumber vector and $\check{Q}_{ij}$ are the 1D Fourier transforms. The inverse is

$$\begin{aligned}
Q_{ij}(\mathbf{r}) &= \int_{-\infty}^{\infty} \int_{-\infty}^{\infty} \hat{Q}_{ij}(\mathbf{k}) e^{i\mathbf{k}.\mathbf{r}} dk dl \\
&= \int_{-\infty}^{\infty} \check{Q}_{ij}(k, y) e^{ily} dl \\
&= \int_{-\infty}^{\infty} \check{Q}_{ij}(x, l) e^{ikx} dk.
\end{aligned} \tag{5.21}$$

Also a single directional transform can be taken, as seen from A4 and A5

$$\check{Q}_{ij}(k, y) = \int_{-\infty}^{\infty} \hat{Q}_{ij}(\mathbf{k}) e^{ily} dl \tag{5.22}$$

For isotropic turbulence $\hat{Q}_{ij}(\mathbf{k})$ can be expressed only as a function of $k_h = \sqrt{k^2 + l^2}$. Thus, switching to polar coordinates

$$
\begin{aligned}
Q_{ij}(\mathbf{r}) &= \int_0^\infty \int_0^{2\pi} \hat{Q}_{ij}(k_h) e^{ik_h r(cos(\theta - \phi))} k_h dk_h d\phi \\
&= 2\pi \int_0^\infty \hat{Q}_{ij}(k_h) J_0(k_h r) k_h dk_h
\end{aligned}
\tag{5.23}
$$

The inverse relationship is simply

$$
\hat{Q}_{ij}(k_h) = \frac{1}{2\pi} \int_0^\infty Q_{ij}(r) J_0(k_h r) r dr
\tag{5.24}
$$

The trace of $Q_{ij}(0)$ is twice the total kinetic energy.

$$
\begin{aligned}
E_{tot} = \frac{1}{2} Q_{ii}(0) &= \frac{1}{2} \int_{-\infty}^\infty \int_{-\infty}^\infty \hat{Q}_{ij}(\mathbf{k}) dk dl \\
&= \int_0^\infty \hat{Q}_{ij}(k_h) \pi k_h dk_h \\
&= \int_0^\infty E(k_h) dk_h
\end{aligned}
\tag{5.25}
$$

$E(k_h) = \hat{Q}_{ij}(k_h) \pi k_h$ is the 2D energy spectrum.

Often, measurements can be made only along a single a track and it is not possible to to estimate the 2D energy spectrum. In such scenarios we can only estimate $\check{Q}_{ij}$,

$$
\check{Q}_{ij}(k, y_o) = \frac{1}{2\pi} \int_{-\infty}^\infty Q_{ij}(x, y_o) e^{-ikx} dx,
\tag{5.26}
$$

and the transform

$$
Q_{ij}(x, y_o) = \int_{-\infty}^\infty \check{Q}_{ij}(k, y_o) e^{ikx} dk,
\tag{5.27}
$$

where x is along the track and y_o is the y location of the track in the rotated coordinate system.

Twice of the total energy is still the trace of $Q_{ij}(0, y_o)$

$$
\begin{aligned}
E_{tot} = \frac{1}{2} Q_{ii}(0, y_o) &= \frac{1}{2} \int_{-\infty}^\infty \check{Q}_{ii}(k, y_o) dk \\
&= \int_0^\infty \check{Q}_{ii}(k, y_o) dk \\
&= \int_0^\infty E_1(k) dk,
\end{aligned}
\tag{5.28}
$$

where $E_1(k) = \check{Q}_{ii}(k, y_o)$ is the 1D energy spectrum. The dependence on y_o is irrelevant for a homogeneous flow. The relationship between the 1D and 2D spectrum can be shown easily at this point by inverting the third relationship of A.6 at $y = 0$, as

$$\check{Q}_{ij}(k, 0) = \int_{-\infty}^{\infty} \hat{Q}_{ij}(k, l) dl$$
$$E_1(k) = \int_{-\infty}^{\infty} \hat{Q}_{ij}(k_h) dl \qquad (5.29)$$
$$E_1(k) = \frac{2}{\pi} \int_0^{\infty} \frac{E(k_h)}{k_h} dl.$$

Now using $k_h^2 = k^2 + l^2$ and at constant k, we get $k_h dk_h = l dl$. Thus

$$E_1(k) = \frac{2}{\pi} \int_{|k|}^{\infty} \frac{E(k_h)}{\sqrt{k_h^2 - k^2}} dk_h. \qquad (5.30)$$

The second order structure can be related to the correlation function as

$$S_{ii}(r) = <u_i^2(0)> + <u_i^2(r)> - 2 <u_i(0)u_i(r)>$$
$$= 4E_{tot} - 2Q_{ii}(r). \qquad (5.31)$$

We only consider the non-cross terms because the cross terms are usually not considered. However, they algebra is straightforward.

As for isotropic second order structure functions the averaging along a line and over all space is the same $(S_{ij}(\mathbf{r}) = S_{ij}(r))$, we can write $S_{ij}(r) = S_{ij}(x, 0)$. Thus

$$S_{ii}(x, 0) = 4E_{tot} - 2Q_{ii}(x, 0)$$
$$= 4 \int_0^{\infty} E(k) dk - 2 \int_{-\infty}^{\infty} \check{Q}_{ii}(k, 0) e^{ikx} dk \qquad (5.32)$$
$$= 4 \int_0^{\infty} E_1(k)(1 - \cos(kx)) dk.$$

and this can be inverted by simply taking the Fourier transform

$$E_1(k) = \frac{2}{\pi} \int_0^{\infty} \frac{S_{ii}(\infty) - S_{ii}(r)}{4} \cos(kx) dx \qquad (5.33)$$

117

The relationship to the 2D spectrum is also obvious using A.7 in A.14

$$
\begin{aligned}
S_{ii}(r) &= 4E_{tot} - 2Q_{ii}(r) \\
&= 4\int_0^\infty E(k_h)dk_h - 4\pi \int_0^\infty \hat{Q}_{ii}(k_h)k_h J_o(k_h r)dk_h \\
&= 4\int_0^\infty E(k_h)(1 - J_o(k_h r))dk_h
\end{aligned}
\tag{5.34}
$$

It is also possible to invert this using A.8 and definition of E(k)

$$
E(k_h) = \int_0^\infty \frac{(S_{ii}(\infty) - S_{ii}(r))}{4} J_0(k_h r)k_h r dr
\tag{5.35}
$$
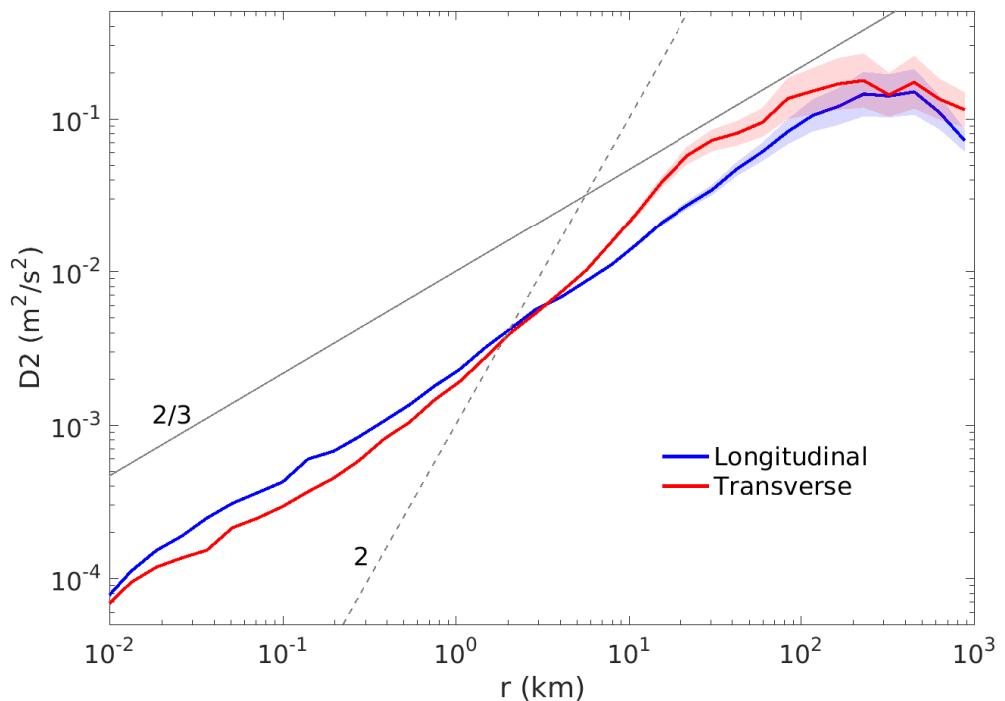
Figure 5.4: [supplementary figure] The longitudinal and transverse second order velocity structure functions with errorbars estimated as the 95th percentile confidence intervals using bootstrapping.
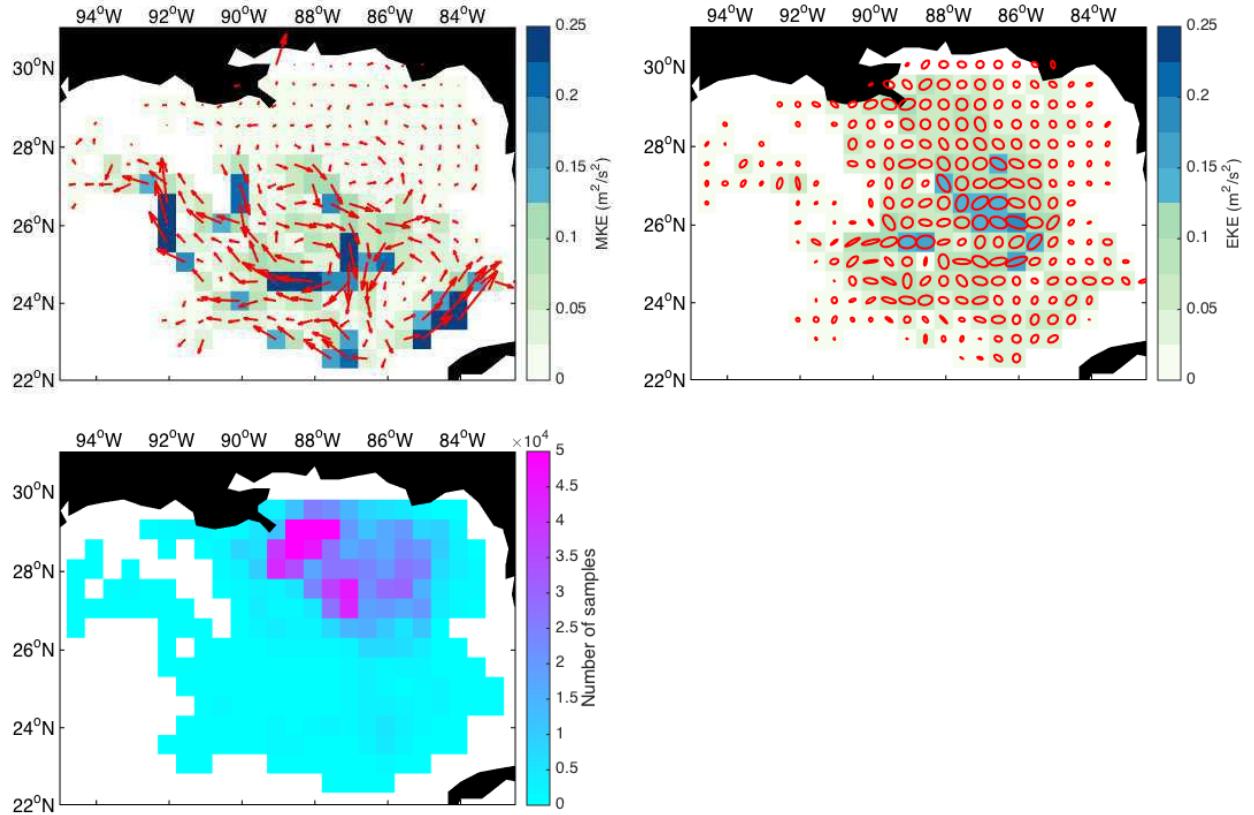
Figure 5.5: [supplementary figure] **Binned statistics in 0.5X0.5 degree bins calculated using the GLAD data in the Gulf of Mexico** (a) Mean kinetic energy and velocity vectors, (b) eddy kinetic energy and variance ellipses, and (c) number of drifter samples per bin.
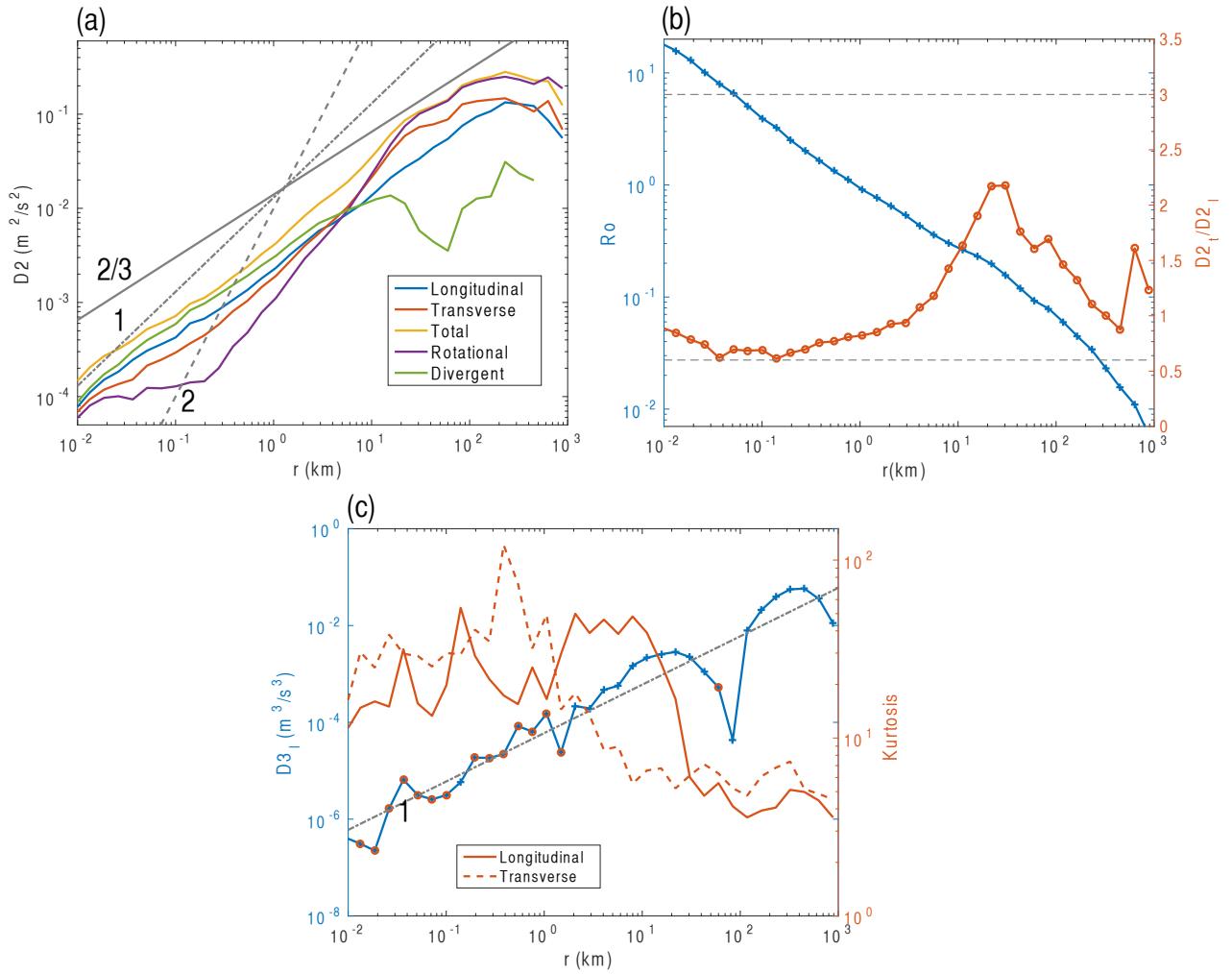
Figure 5.6: [supplementary figure] **Results for drifters trajectories situated to the north and west of 87W and 27N.** (a) Different components of the second order velocity structure functions. Three power law relationships are plotted as gray lines with slopes marked on the top. (b) Left axis, blue, shows the Rossby number defined as $\sqrt{D2}/(fr)$, where f is the Coriolis parameter and r is the separation distance. Right axis, orange, shows the ratio of the transverse to longitudinal second order velocity structure function ($D2_t/D2_l$). (c) Absolute value of the longitudinal component of the third order velocity structure function ($D3_l$) on the left axis (blue axis and line). Orange circles and blue pluses represent negative and positive values, respectively. A linear power law relationship is shown as dashed gray line. Kurtosis ($\frac{<\delta u^4>}{<\delta u^2>^2}$), both longitudinal and transverse components, is shown in orange on the right axis.

121
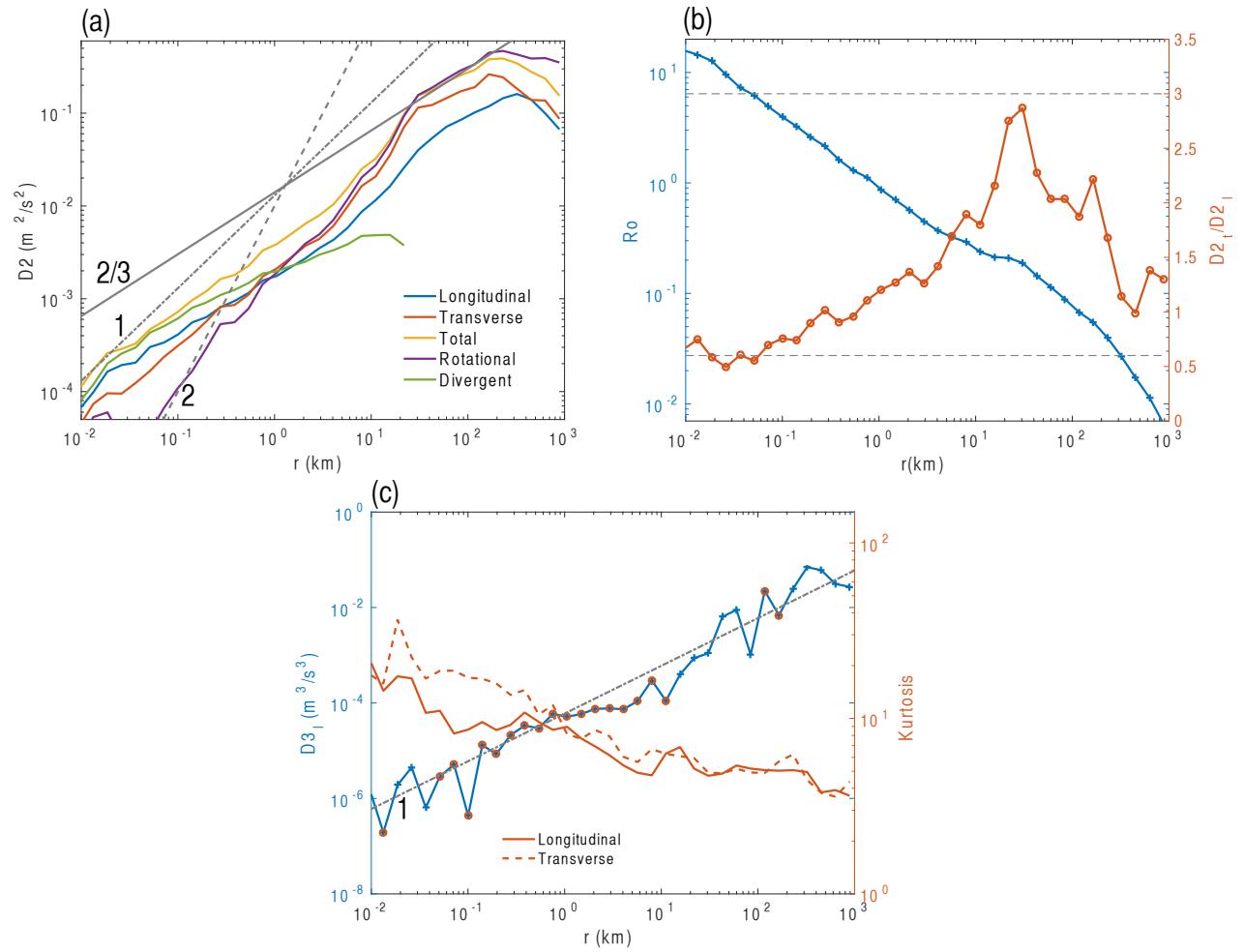
Figure 5.7: [supplementary figure] **Results for drifters trajectories situated to the south and east of 87W and 27N.** (a), (b) and (c) are the same as for Figure S3.
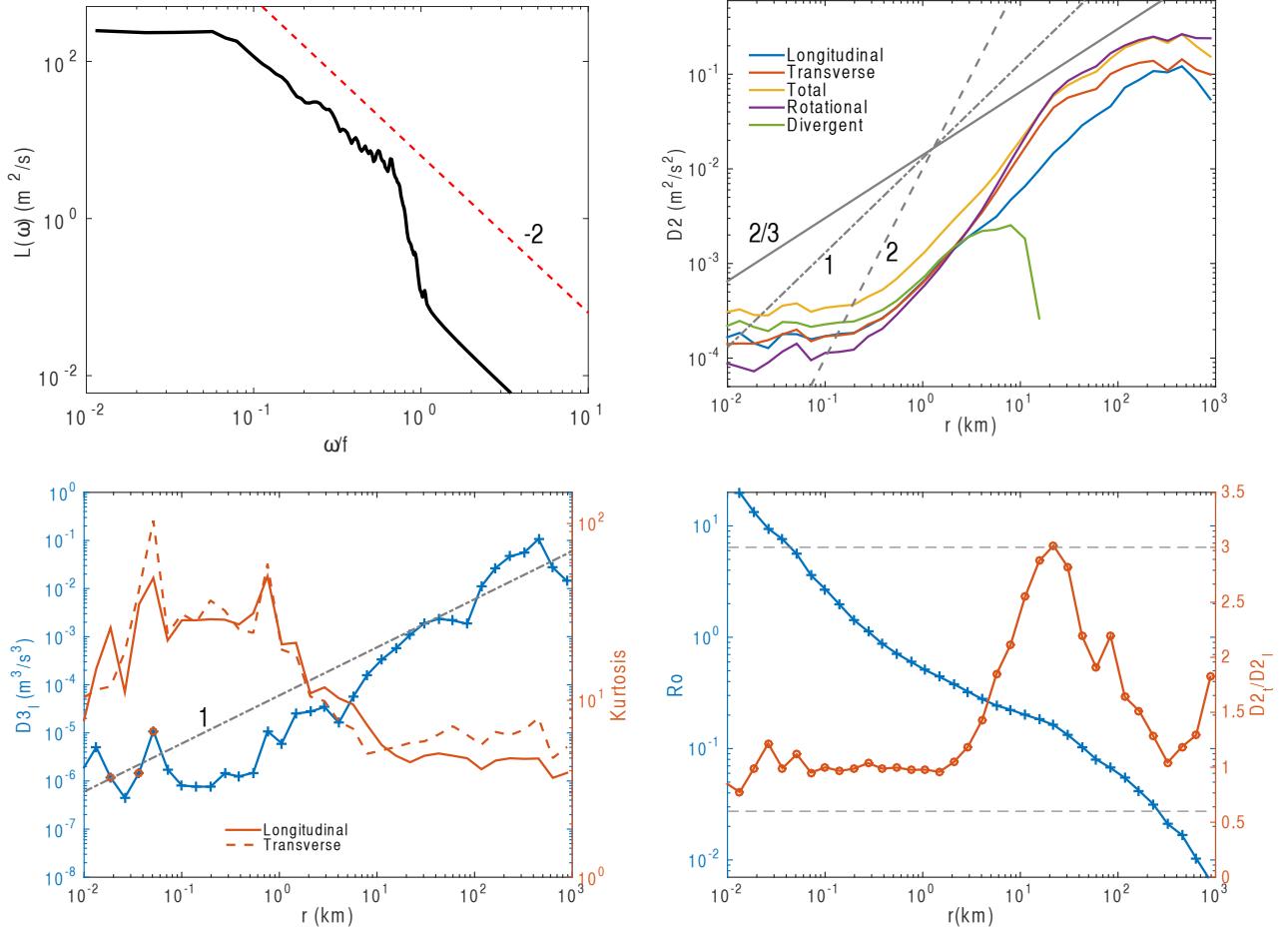
Figure 5.8: [supplementary figure] **Lowpass filtered results** (a) Lagrangian frequency spectrum after filtering. (b) Different components of the second order velocity structure functions. Three power law relationships are plotted as gray lines with slopes marked on the top. (c) Left axis, blue, shows the Rossby number defined as $\sqrt{D2}/(fr)$, where f is the Coriolis parameter and r is the separation distance. Right axis, orange, shows the ratio of the transverse to longitudinal second order velocity structure function ($D2_t/D2_l$). (d) Absolute value of the longitudinal component of the third order velocity structure function ($D3_l$) on the left axis (blue axis and line). Orange circles and blue pluses represent negative and positive values, respectively. A linear power law relationship is shown as dashed gray line. Kurtosis ($\frac{<\delta u^4>}{<\delta u^2>^2}$), both longitudinal and transverse components, is shown in orange on the right axis.
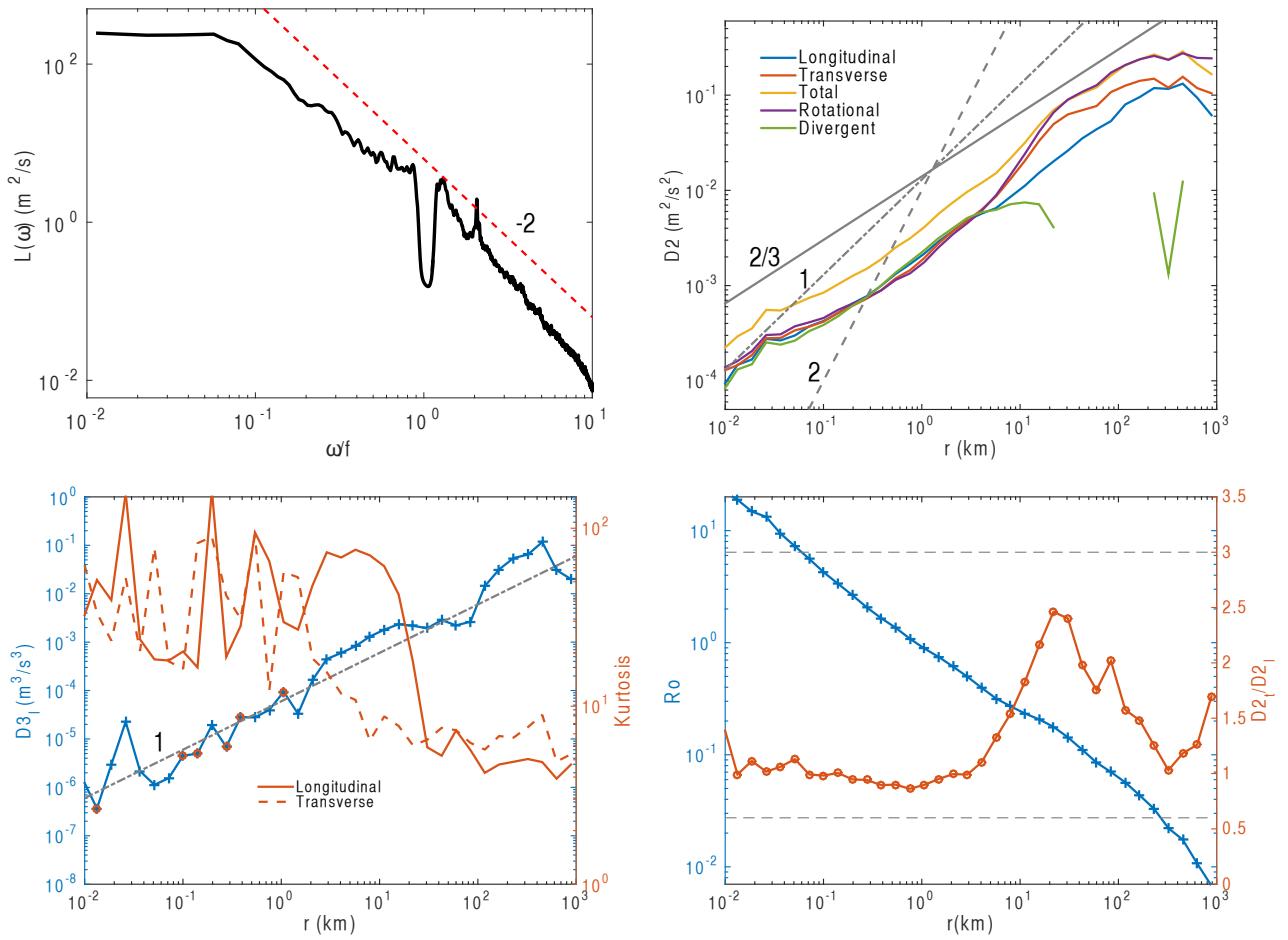
Figure 5.9: [supplementary figure] **Bandpass filtered results** (a), (b), (c) and (d) are the same as for Figure S5.
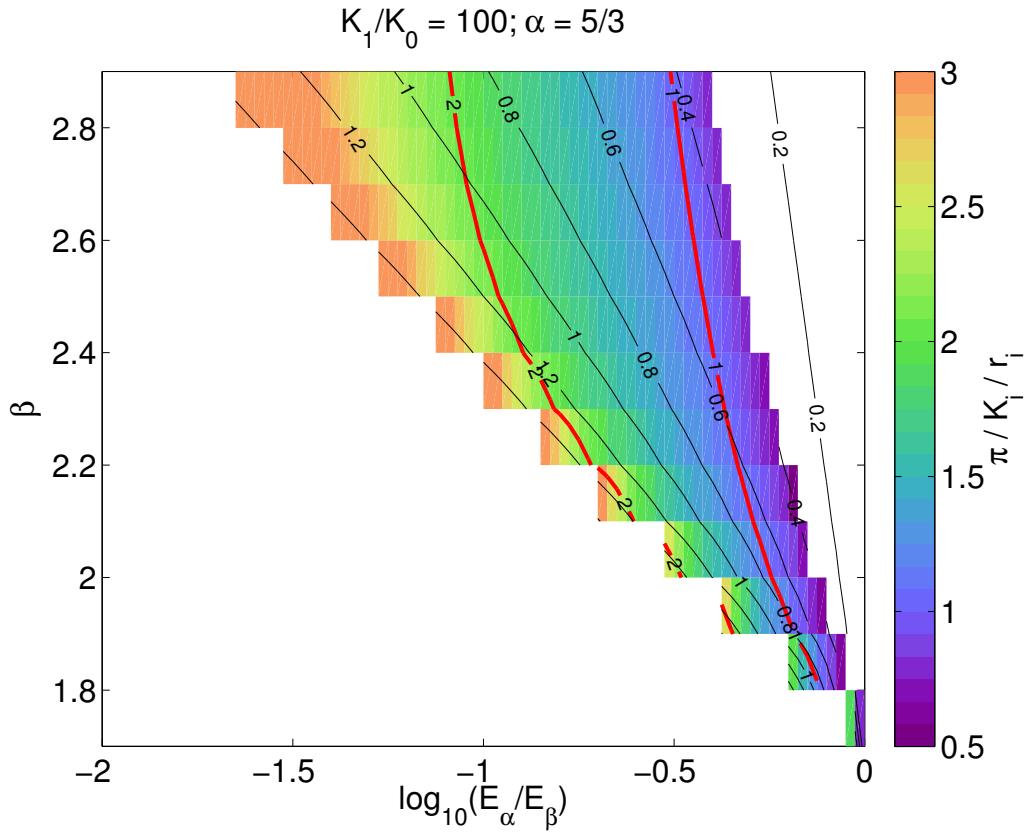
Figure 5.10: [supplementary figure] Colored contours show the ratio of the intersection length scale for the energy spectra to the intersection length scale $(\pi/(k_i r_i))$ for the structure functions as a function of slope and ratio of energy density at the the lower wavenumber cut off. The red colored contour lines represent the ratios of of 1 and 2. α was fixed to be 5/3 and β varies from 5/3 to 3. The marked black contour lines show the ratio of k_o to the intersection wavenumber (k_o/k_i) on a log scale.
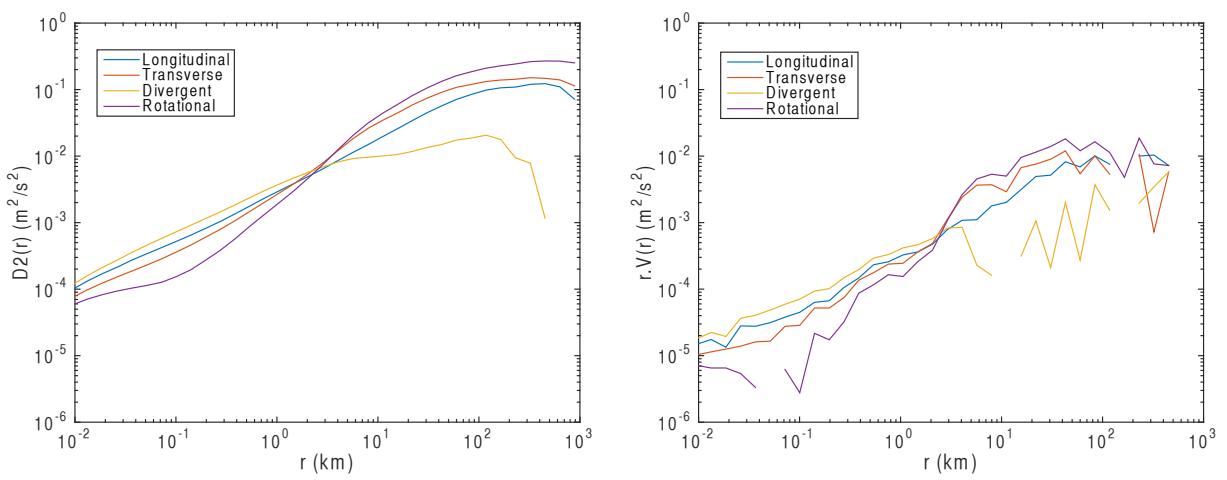
Figure 5.11: [supplementary figure] (Left) Smoothed second order velocity structure functions calculated from the original structure functions (Figure 2, main text). (Right) Signature functions corresponding to the smoothed second order velocity structure functions.

CHAPTER 6

CONCLUSIONS

The ocean exhibits variability over a wide range of length scales and time scales, and the complex interplay of these processes, both as linear super-position and non-linear interactions, manifests itself as chaos or turbulence. It is important to gain a phenomenological understanding of this variability, as it not only influences local flow patterns, that affect the mixing and stirring of tracers, but it also contributes to the large scale mean circulation in the ocean. In this dissertation, we primarily use observations to quantify the effects of these transient processes - eddy processes.

Observing the synoptic ocean is challenging due to the large length scales associated with the variability, and the rapidly changing environment, relative to the capabilities of most in-situ observing platforms. Here we rely primarily on Lagrangian observations, which usually have a high temporal resolution, but their spatial resolution of the flow is limited by their initial deployment and subject to the flow itself. RAFOS floats, deep Lagrangian floats, deployed as part of the Diapycnal and Isopycnal Mixing Experiment in the Southern Ocean (DIMES), are used to quantify the eddy processes in the Southeast Pacific Ocean and Scotia Sea. These floats were able to provide us an unprecedented high resolution sampling (daily and O(3km)) of the mid-depth Southern Ocean, which would not have been possible with satellite, or ship-board and moored observations. We also use an extremely high resolution (15 mins and O(10 m)) surface drifter data set that was collected, as part of the Grand Lagrangian Deployment (GLAD), in the Gulf of Mexico.

The first part of this thesis helps in realizing the primary goal of the DIMES experiment, quantifying the influence of the eddies in the Southern Ocean on the meridional overturning circulation (MOC). In chapter 2, we present the results from a statistical analysis of the float trajectories to quantify the mid-depth mean circulation and the effects of eddy stirring in the framework of eddy diffusivity. The estimates of the mean circulation verify the expectation that the Antarctic Circumpolar Current (ACC) is composed of mean jet like features superimposed on a mean eastward flow, even at a depth of 1500 m. The eddy diffusivity is found to vary greatly between the Southeast Pacific Ocean and Scotia Sea, primarily due to the contrast in bottom bathymetric characteristics

leading to large differences in the eddy kinetic energy of the two regions. The vertical structure of the eddy diffusivity in the Southeast Pacific Ocean is suppressed to values smaller than what would be expected if the ACC was absent, showing agreement with theories of mean flow suppression (Ferrari and Nikurashin (2010)). However, a mid-depth maxima in eddy diffusivity, which was noted by previous studies (Tulloch et al. (2014); Lacasce et al. (2014)), does not result directly from the suppression by the large scale ACC flow, but is instead a result of horizontal inhomogeneities in the eddy diffusivity due to the presence of jets.

In chapter 3, the eddy diffusivities estimated from the DIMES experiment, along with two other diffusivity estimates that quantify the eddy diffusivity for the entire Southern Ocean, are used to quantify the eddy bolus velocity. It is assumed, as has been verified using models (e.g. Abernathey et al. (2013)), that the eddy diffusivity estimates from observations are comparable to the potential vorticity (PV) diffusivity. The eddy bolus velocities are estimated assuming a down gradient diffusion of large scale PV. The eddy driven bolus velocities calculated using this parameterization are on the order of $10^{-4} - 10^{-3}$ m/s, and zonal variations in this eddy driven velocity are shown to be influenced by the interaction of the ACC with bottom topography. The zonal variability of the eddy bolus velocity is a result of the variability of both the large scale PV gradients and eddy diffusivities.

Future work is necessary to improve our understanding of the influence that eddies have on the mean circulation. Firstly, it is important to realize that the downgradient diffusion is usually adopted for its simplicity, rather than its ability to provide a dynamically correct parameterization. More advanced parameterization that rely on stochastic representations have been proposed (Grooms and Majda (2014), also see review in LaCasce (2008)). However, there has not been much emphasis on using observations, or designing observational experiments to constrain the parameters that these parameterizations require. It will be a worthwhile effort to assess the utility of the current oceanographic data sets to constrain these parameters, and also to provide a set of recommendations for future observational studies so that their data sets can be used more broadly for constraining parameterizations.

In chapter 3, we note that isopycnals that are at depths shallower than the sill depth can support mean meridional geostrophic flow, provided that no closed contours of PV are present, or alternatively no closed Montgomery streamfunction contours (or some more appropriate streamfunction)

are present. This effect was also noted in Mazloff et al. (2013), and it was shown that in a zonal average the mean geostrophic flow partially cancelled the eddy driven overturning. However, this idea has not been fully explored. In particular it remains to be understood as to what regions contribute to this mean geostrophic flow, and why. PV sources and sinks, both at the surface and bottom, contribute in maintaining an equilibrium in which the PV contours are not closed. We have done some preliminary work in this regard and noticed that a few key regions, such as the Scotia Sea and Kerguelan Plateau at depth, and the location where the ACC flows over the Pacific Antarctic ridge at the surface, seem to be introducing anomalous PV signals into the ACC. This work is currently under way and will help in elucidating the mechanisms that support the mean geostrophic flow across the ACC.

In the second half of this work, we use Lagrangian observations to quantify the kinetic energy spectrum, which is often the key scaling result of turbulence theories, indirectly using velocity structure functions. We also quantify the relative dispersion observed at length scales smaller than the dominant eddy scales (≤ 100 km). Chapter 4 returns to the DIMES RAFOS floats for characterizing the mesoscale turbulence and associated dispersion in the mid-depth ACC. The observations agree with interior quasi-geostrophic turbulence theory over a short range of scales ($30 - 100$ km), below which the flow has both rotational and divergent components. The observed particle spreading is characterized as local dispersion, i.e., particle separation grows due to the influence of eddies at the size of separation. Analysis of particles released in a numerical model shows that the dispersion in the model is non-local. Additionally the divergent flow in the model is significantly smaller than that seen in the observations. Thus, it seems that the model is unrepresentative at small scales and the divergent flow might be playing an important role in the local dispersion observed by the RAFOS floats.

In Chapter 5 we analyze drifter trajectories from the surface ocean in the Gulf of Mexico. This work was started when we initially realized the utility of velocity structure functions in characterizing the turbulent dynamics, and wanted to test the methods on a high resolution data set. The large drifter density at small scales allowed us to quantify the velocity structure functions down to unprecedented length scales of O(10 m). The results reveal a clear cross-over of divergent and rotational second order velocity structure functions at a scale of 5 km, with divergent flows dominating at smaller length scales. This length scale also happens to be the length scale at which the Rossby

number (Ro) transitions from being less than order one at larger length scales to greater than order one at smaller length scales. The third order structure functions indicated the presence of a possible forward energy cascade associated with the length scales where the divergent component dominates and the Ro is greater than one.

Our work has testified to the power of Lagrangian observations in statistically quantifying ocean turbulence. This is possibly one of the most statistically reliable observational techniques that is currently capable of resolving the flow over a large range of length scales. The next logical step will be to extend this work to the large data set that is available through the global drifter program, to understand the geographical variations of the surface turbulence. It will also by important to test the robustness of these methods, for example understand the influence that the time resolution of the trajectories and inhomogeneities of the flow have on the reliability of the measures. There also issues with relating the structure functions directly to the energy spectrum, as were alluded to in chapter 5. Davidson and Pearson (2005) suggest the use of another measure, referred to as the signature functions. The potential and shortcomings of this measure to better quantify the scale dependent energy distribution remains to be tested.

Even though this work on characterizing turbulence and dispersion reveals important properties of the flow field, we are currently unable to provide a process level understanding. For example, we can not distinguish if the strong divergent flows seen at the surface are a result of inertia-gravity waves or other divergent processes that manifest themselves at the surface ocean. It might be possible to make some progress towards a process level understanding by using surface drifters that are equipped with temperature and salinity sensors, or looking at the results from surface drifters in conjunction with satellite based high resolution sea surface temperature measurements.

The growing dominance of the divergent flow components at small scales calls for us to question the applicability of theories that relate the dispersion to the energy spectrum, which almost always assume the flow field to be non-divergent. It remains to be understood if the dispersion can still be characterized simply as local and non-local dispersion in the presence of divergent flows, or if the effects of divergent clustering strongly influence the kinematics, and we need more sophisticated measures to characterize the flow. Previous studies identify internal waves (Bühler et al. (2013)) or vortical motions (Polzin and Ferrari (2004)) as likely candidates for local dispersion at small scales in the interior. However, it still remains to be tested if the observed divergent flows are consistent

with these proposed dynamics. Also, it is important to study how the dispersion might behave when multiple mechanisms coexist, which is likely the case in the ocean.

BIBLIOGRAPHY

R. Abernathey, J. Marshall, M. Mazloff, and E. Shuckburgh. Enhancement of mesoscale eddy stirring at steering levels in the Southern Ocean. *Journal of Physical Oceanography*, 40(1): 170–184, 2010.

R. Abernathey, D. Ferreira, and A. Klocker. Diagnostics of isopycnal mixing in a circumpolar channel. *Ocean Modelling*, 72:1 – 16, 2013. ISSN 1463-5003.

R. P. Abernathey and J. Marshall. Global surface eddy diffusivities derived from satellite altimetry. *Journal of Geophysical Research*, 2013.

A. Babiano, C. Basdevant, and R. Sadourny. Structure functions and dispersion laws in two-dimensional turbulence. *Journal of the Atmospheric Sciences*, 42(9):941–949, 1985.

D. Balwada, J. H. LaCasce, and K. G. Speer. Scale Dependent Distribution of Kinetic Energy from Surface Drifters in the Gulf of Mexico. *Geophysical Research Letters*, pages n/a–n/a, 2016a. ISSN 1944-8007. 2016GL069405.

D. Balwada, K. G. Speer, J. H. LaCasce, W. B. Owens, J. Marshall, and R. Ferrari. Circulation and Stirring in the Southeast Pacific Ocean and the Scotia Sea Sectors of the Antarctic Circumpolar Current. *Journal of Physical Oceanography*, 46(7):2005–2027, 2016b.

N. Barré, C. Provost, A. Renault, and N. Sennéchael. Fronts, meanders and eddies in Drake Passage during the ANT-XXIII/3 cruise in January–February 2006: A satellite perspective. *Deep Sea Research Part II: Topical Studies in Oceanography*, 58(25):2533–2554, 2011.

G. K. Batchelor. *The theory of homogeneous turbulence.* Cambridge university press, 1953.

M. Bates, R. Tulloch, J. Marshall, and R. Ferrari. Rationalizing the spatial distribution of mesoscale eddy diffusivity in terms of mixing length theory. *Journal of Physical Oceanography*, 44(6): 1523–1540, 2015/05/28 2014.

A. Bennett. Relative dispersion: Local and nonlocal dynamics. *Journal of the atmospheric sciences*, 41(11):1881–1886, 1984.

F. J. Beron-Vera and J. H. LaCasce. Statistics of Simulated and Observed Pair Separations in the Gulf of Mexico. *Journal of Physical Oceanography*, 46(7):2183–2199, 2016.

E. J. D. Boland, E. Shuckburgh, P. H. Haynes, J. R. Ledwell, M.-J. Messias, and A. J. Watson. Estimating a submesoscale diffusivity using a roughness measure applied to a tracer release experiment in the Southern Ocean. *Journal of Physical Oceanography*, 45(6):1610–1631, 2015.

J. A. Brearley, K. L. Sheen, A. C. Naveira Garabato, D. A. Smeed, K. G. Speer, A. M. Thurnherr, M. P. Meredith, and S. Waterman. Deep boundary current disintegration in Drake Passage. *Geophysical Research Letters*, 41(1):121–127, 2014. ISSN 1944-8007. 2013GL058617.

O. Bühler, N. Grisouard, and M. Holmes-Cerfon. Strong particle dispersion by weakly dissipative random internal waves. *Journal of Fluid Mechanics*, 719:R4, 2013.

O. Bühler, J. Callies, and R. Ferrari. Wave–vortex decomposition of one-dimensional ship-track data. *Journal of Fluid Mechanics*, 756:1007–1026, 10 2014. ISSN 1469-7645.

J. Callies and R. Ferrari. Interpreting energy and tracer spectra of upper-ocean turbulence in the submesoscale range (1-200 km). *Journal of Physical Oceanography*, 43(11):2456–2474, 2013.

J. Callies, R. Ferrari, and O. Bühler. Transition from geostrophic turbulence to inertia–gravity waves in the atmospheric energy spectrum. *Proceedings of the National Academy of Sciences of the United States of America*, 2014.

J. Callies, R. Ferrari, J. M. Klymak, and J. Gula. Seasonality in submesoscale turbulence. *Nature communications*, 6, 2015.

J. G. Charney. Geostrophic turbulence. *Journal of the Atmospheric Sciences*, 28(6):1087–1095, 1971.

C. P. Chavanne and P. Klein. Can oceanic submesoscale processes be observed with satellite altimetry? *Geophysical Research Letters*, 37(22), 2010.

D. B. Chelton, R. A. deSzoeke, M. G. Schlax, K. El Naggar, and N. Siwertz. Geographical variability of the first baroclinic rossby radius of deformation. *Journal of Physical Oceanography*, 28(3): 433–460, 1998.

D. B. Chelton, M. G. Schlax, and R. M. Samelson. Global observations of nonlinear mesoscale eddies. *Progress in Oceanography*, 91(2):167–216, 2011.

R. Chen, S. T. Gille, J. L. McClean, G. R. Flierl, and A. Griesel. A multi-wavenumber theory for eddy diffusivities and its application to the southeast Pacific (DIMES) region. *Journal of Physical Oceanography*, 2015.

T. K. Chereskin, L. D. Talley, and B. M. Sloyan. Nonlinear vorticity balance of the subantarctic front in the southeast pacific. *Journal of Geophysical Research: Oceans*, 115(C6), 2010.

J. Y. Cho and E. Lindborg. Horizontal velocity structure functions in the upper troposphere and lower stratosphere. 1. observations. *J. Geophys. Res*, 106(10):223–10, 2001.

S. T. Cole, C. Wortham, E. Kunze, and W. B. Owens. Eddy stirring and horizontal diffusivity from argo float observations: Geographic and depth variability. *Geophysical Research Letters*, 42 (10):3989–3997, 2015. ISSN 1944-8007. 2015GL063827.

P. Davidson and B. Pearson. Identifying turbulent energy distributions in real, rather than fourier, space. *Physical review letters*, 95(21):214501, 2005.

P. A. Davidson. *Turbulence: an introduction for scientists and engineers.* Oxford University Press, 2015.

E. Dewan. Saturated-cascade similitude theory of gravity wave spectra. *Journal of Geophysical Research: Atmospheres*, 102(D25):29799–29817, 1997.

D. G. Dritschel and M. E. McIntyre. Multiple jets as pv staircases: The phillips effect and the resilience of eddy-transport barriers. *Journal of the Atmospheric Sciences*, 65(3):855–874, 2008.

V. Faure and K. Speer. Deep circulation in the Eastern South Pacific Ocean. *Journal of Marine Research*, 70(5):748–778, 2012.

R. Ferrari and M. Nikurashin. Suppression of eddy diffusivity across jets in the Southern Ocean. *Journal of Physical Oceanography*, 40(7):1501–1519, 2010.

R. Ferrari and C. Wunsch. Ocean circulation kinetic energy: Reservoirs, sources, and sinks. *Annual Review of Fluid Mechanics*, 41(1):253, 2008.

R. Ferrari and C. Wunsch. The distribution of eddy kinetic and potential energies in the global ocean. *Tellus A*, 62(2):92–108, 2010.

R. Ferrari, C. Provost, A. Renault, N. Sennéchael, N. Barré, Y.-H. Park, and J. H. Lee. Circulation in Drake Passage revisited using new current time series and satellite altimetry: 1. The Yaghan Basin. *Journal of Geophysical Research: Oceans (1978–2012)*, 117(C12), 2012.

R. Ferrari, C. Provost, N. Sennéchael, and J.-H. Lee. Circulation in Drake Passage revisited using new current time series and satellite altimetry: 2. The Ona Basin. *Journal of Geophysical Research: Oceans*, 2013.

Y. L. Firing, T. K. Chereskin, and M. R. Mazloff. Vertical structure and transport of the Antarctic Circumpolar Current in Drake Passage from direct velocity observations. *Journal of Geophysical Research*, 116(C8):C08015, 2011.

U. Frisch. *Turbulence: the legacy of AN Kolmogorov.* Cambridge university press, 1995.

L.-L. Fu. Pattern and velocity of propagation of the global ocean eddy variability. *Journal of Geophysical Research*, 114(C11017), 2009.

K. S. Gage and G. D. Nastrom. Spectrum of atmospheric vertical displacements and spectrum of conservative scalar passive additives due to quasi-horizontal atmospheric motions. *Journal of Geophysical Research: Atmospheres*, 91(D12):13211–13216, 1986.

A. C. N. Garabato, A. P. Williams, and S. Bacon. The three-dimensional overturning circulation of the Southern Ocean during the WOCE era. *Progress in Oceanography*, 120:41 – 78, 2014.

A. C. N. Garabato, K. L. Polzin, R. Ferrari, J. D. Zika, and A. Forryan. A microscale view of mixing and overturning across the antarctic circumpolar current. *Journal of Physical Oceanography*, 46(1):233–254, 2016.

Z. D. Garraffo, A. J. Mariano, A. Griffa, C. Veneziani, and E. P. Chassignet. Lagrangian data in a high-resolution numerical simulation of the North Atlantic: I. comparison with in situ drifter data. *Journal of Marine Systems*, 29(1):157–176, 2001.

C. Garrett. Turbulent dispersion in the ocean. *Progress in Oceanography*, 70(2):113–125, 2006.

C. Garrett and W. Munk. Space-time scales of internal waves. *Geophysical & Astrophysical Fluid Dynamics*, 3(1):225–264, 1972.

P. R. Gent and J. C. Mcwilliams. Isopycnal mixing in ocean circulation models. *Journal of Physical Oceanography*, 20(1):150–155, 1990.

A. Gnanadesikan, M.-A. Pradal, and R. Abernathey. Isopycnal mixing by mesoscale eddies significantly impacts oceanic anthropogenic carbon uptake. *Geophysical Research Letters*, 42(11): 4249–4255, 2015. ISSN 1944-8007.

L. Graff, S. Guttu, and J. LaCasce. Relative dispersion in the atmosphere from reanalysis winds. *Journal of the Atmospheric Sciences*, 72(7):2769–2785, 2015.

A. Griesel, C. Eden, N. Koopmann, and E. Yulaeva. Comparing isopycnal eddy diffusivities in the southern ocean with predictions from linear theory. *Ocean Modelling*, 94:33 – 45, 2015.

I. Grooms and A. J. Majda. Stochastic superparameterization in quasigeostrophic turbulence. *Journal of Computational Physics*, 271:78–98, 2014.

R. Hallberg and A. Gnanadesikan. The role of eddies in determining the structure and response of the wind-driven southern hemisphere overturning: Results from the modeling eddies in the southern ocean (meso) project. *Journal of Physical Oceanography*, 36(12):2232–2252, 2006.

I. M. Held, R. T. Pierrehumbert, S. T. Garner, and K. L. Swanson. Surface quasi-geostrophic dynamics. *Journal of Fluid Mechanics*, 282:1–20, 1 1995.

C. C. Henning and G. K. Vallis. The effects of mesoscale eddies on the stratification and transport of an ocean with a circumpolar channel. *Journal of Physical Oceanography*, 35(5):880–896, 2005.

B. L. Hua, J. C. McWilliams, and P. Klein. Lagrangian accelerations in geostrophic turbulence. *Journal of Fluid Mechanics*, 366:87–108, 7 1998. ISSN 1469-7645.

C. W. Hughes. Nonlinear vorticity balance of the Antarctic Circumpolar Current. *Journal of Geophysical Research: Oceans*, 110(C11), 2005.

C. W. Hughes and P. D. Killworth. Effects of bottom topography in the large-scale circulation of the Southern Ocean. *Journal of Physical Oceanography*, 25(11):2485–2497, 1995.

D. R. Jackett and T. J. McDougall. A neutral density variable for the world's oceans. *Journal of Physical Oceanography*, 27(2):237–263, 1997.

R. H. Karsten and J. Marshall. Testing theories of the vertical stratification of the ACC against observations. *Dynamics of Atmospheres and Oceans*, 36(1):233–246, 2002.

P. Killworth. An equivalent-barotropic mode in the fine resolution model. *Journal of Physical Oceanography*, 21(1):1379–1387, 1992.

Y. S. Kim and A. H. Orsi. On the variability of Antarctic Circumpolar Current Fronts inferred from 1992–2011 altimetry. *Journal of Physical Oceanography*, 44(12):3054–3071, 2014.

A. Klocker, R. Ferrari, and J. H. LaCasce. Estimating suppression of eddy mixing by mean flows. *Journal of Physical Oceanography*, 42(9):1566–1576, 2012.

A. N. Kolmogorov. The local structure of turbulence in incompressible viscous fluid for very large reynolds numbers. In *Dokl. Akad. Nauk SSSR*, volume 30, pages 301–305. JSTOR, 1941.

I. Koszalka, J. LaCasce, and K. Orvik. Relative dispersion in the nordic seas. *Journal of Marine Research*, 67(4):411–433, 2009.

R. H. Kraichnan. Dispersion of particle pairs in homogeneous turbulence. *Physics of Fluids (1958-1988)*, 9(10):1937–1943, 1966.

R. H. Kraichnan. Inertial ranges in two-dimensional turbulence. Technical report, DTIC Document, 1967.

J. LaCasce. On turbulence and normal modes in a basin. *Journal of Marine Research*, 60(3):431–460, 2002.

J. LaCasce. Statistics from lagrangian observations. *Progress in Oceanography*, 77(1):1–29, 2008.

J. LaCasce. Relative displacement probability distribution functions from balloons and drifters. *Journal of Marine Research*, 68(3-4):433–457, 2010.

J. LaCasce and A. Bower. Relative dispersion in the subsurface north atlantic. *Journal of Marine Research*, 58(6):863–894, 2000.

J. LaCasce and P. Isachsen. The linear models of the ACC. *Progress in Oceanography*, 84(3): 139–157, 2010.

J. LaCasce and C. Ohlmann. Relative dispersion at the surface of the Gulf of Mexico. *Journal of Marine Research*, 61(3):285–312, 2003.

J. H. LaCasce. *Calculating Energy Spectra from Drifters*. MDPI Fluids, submitted.

J. H. Lacasce, R. Ferrari, J. Marshall, R. Tulloch, D. Balwada, and K. G. Speer. Float-Derived Isopycnal Diffusivities in the DIMES Experiment. *Journal of Physical Oceanography*, 44(2): 764–780, Feb. 2014.

P.-Y. Le Traon, P. Klein, B. L. Hua, and G. Dibarboure. Do altimeter wavenumber spectra agree with the interior or surface quasigeostrophic theory? *Journal of Physical Oceanography*, 38 (5):1137–1142, 2008.

J. Ledwell, E. Montgomery, K. Polzin, L. S. Laurent, R. Schmitt, and J. Toole. Evidence for enhanced mixing over rough topography in the abyssal ocean. *Nature*, 403(6766):179–182, 2000.

J. R. Ledwell, A. J. Watson, and C. S. Law. Evidence for slow mixing across the pycnocline from an open-ocean tracer-release experiment. *Nature*, 364(6439):701–703, 1993.

J. R. Ledwell, A. J. Watson, and C. S. Law. Mixing of a tracer in the pycnocline. *Journal of Geophysical Research: Oceans*, 103(C10):21499–21529, 1998.

Y. Lenn, T. Chereskin, J. Sprintall, and E. Firing. Mean jets, mesoscale variability and eddy momentum fluxes in the surface layer of the Antarctic Circumpolar Current in Drake Passage. *Journal of Marine Research*, 65(1):27–58, 2007.

E. Lindborg. Can the atmospheric kinetic energy spectrum be explained by two-dimensional turbulence? *Journal of Fluid Mechanics*, 388:259–288, 1999.

E. Lindborg. The energy cascade in a strongly stratified fluid. *Journal of Fluid Mechanics*, 550: 207–242, 3 2006. ISSN 1469-7645.

E. Lindborg. Horizontal wavenumber spectra of vertical vorticity and horizontal divergence in the upper troposphere and lower stratosphere. *Journal of the atmospheric sciences*, 64(3): 1017–1025, 2007.

E. Lindborg. A helmholtz decomposition of structure functions and spectra calculated from aircraft data. *Journal of Fluid Mechanics*, 762:R4, 2015.

E. Lindborg and J. Y. Cho. Horizontal velocity structure functions in the upper troposphere and lower stratosphere. ii- theoretical considerations. *Journal of Geophysical Research*, 106:10, 2001.

J. Lu and K. G. Speer. Topography, jets, and eddy mixing in the Southern Ocean. *Journal of Marine Research*, 68(3-4):479–502, 2010.

R. Lumpkin and S. Elipot. Surface drifter pair spreading in the north atlantic. *Journal of Geophysical Research: Oceans*, 115(C12), 2010.

R. Lumpkin and K. G. Speer. Global ocean meridional overturning. *Journal of Physical Oceanography*, 37(10):2550–2562, 2007.

R. Lumpkin, A.-M. Treguier, and K. Speer. Lagrangian eddy scales in the Northern Atlantic ocean. *Journal of Physical Oceanography*, 32(9):2425–2440, 2015/07/08 2002.

T. Lundgren. Turbulent pair dispersion and scalar diffusion. *Journal of Fluid Mechanics*, 111(362): 2757, 1981.

J. Marshall and T. Radko. Residual-Mean Solutions for the Antarctic Circumpolar Current and Its Associated Overturning Circulation. *Journal of Physical Oceanography*, 33:2341, 2003.

J. Marshall and K. G. Speer. Closure of the meridional overturning circulation through Southern Ocean upwelling. *Nature Geoscience*, 5(3):171–180, Feb. 2012.

M. R. Mazloff, R. Ferrari, and T. Schneider. The force balance of the Southern Ocean meridional overturning circulation. *Journal of Physical Oceanography*, 43(6):1193–1208, 2013.

J. C. McWilliams. Submesoscale currents in the ocean. In *Proc. R. Soc. A*, volume 472, page 20160117. The Royal Society, 2016.

M. P. Meredith, P. L. Woodworth, T. K. Chereskin, D. P. Marshall, L. C. Allison, G. R. Bigg, K. Donohue, K. J. Heywood, C. W. Hughes, A. Hibbert, et al. Sustained monitoring of the Southern Ocean at Drake Passage: Past achievements and future priorities. *Reviews of Geophysics*, 49(4), 2011.

J. F. Middleton. Drifter spectra and diffusivities. *Journal of Marine Research*, 43(1):37–55, 1985.

P. Morel and M. Larceveque. Relative dispersion of constant-level balloons in the 200-mb general circulation. *Journal of the Atmospheric Sciences*, 31(8):2189–2196, 1974.

J. Moum and W. Smyth. Upper ocean mixing processes. *Encyclopedia of Ocean Sciences*, 6: 3093–3100, 2001.

W. H. Munk. Abyssal recipes. In *Deep Sea Research and Oceanographic Abstracts*, volume 13, pages 707–730. Elsevier, 1966.

L.-P. Nadeau and R. Ferrari. The role of closed gyres in setting the zonal transport of the antarctic circumpolar current. *Journal of Physical Oceanography*, 45(6):1491–1509, 2015.

N. Nakamura. Sensitivity of global mixing and fluxes to isolated transport barriers. *Journal of the Atmospheric Sciences*, 65(12):3800–3818, 2008.

G. Nastrom and K. S. Gage. A climatology of atmospheric wavenumber spectra of wind and temperature observed by commercial aircraft. *Journal of the Atmospheric Sciences*, 42(9): 950–960, 1985.

A. C. Naveira-Garabato, D. P. Stevens, A. J. Watson, and W. Roether. Short-circuiting of the overturning circulation in the Antarctic Circumpolar Current. *Nature*, 447(7141):194–197, 2007.

A. C. Naveira Garabato, R. Ferrari, and K. L. Polzin. Eddy stirring in the Southern Ocean. *Journal of Geophysical Research: Oceans (1978–2012)*, 116(C9), 2011.

M. Nikurashin and G. Vallis. A theory of the interhemispheric meridional overturning circulation and associated stratification. *Journal of Physical Oceanography*, 42(10):1652–1667, 2012.

M. Ollitrault and A. Colin de Verdière. SOFAR floats reveal midlatitude intermediate North Atlantic general circulation. Part II: An eulerian statistical view. *Journal of Physical Oceanography*, 32(7):2034–2053, 2015/02/19 2002.

M. Ollitrault, C. Gabillet, and A. C. De Verdiere. Open ocean regimes of relative dispersion. *Journal of fluid mechanics*, 533:381–407, 2005.

A. H. Orsi, T. Whitworth, and W. D. Nowlin. On the meridional extent and fronts of the Antarctic Circumpolar Current. *Deep Sea Research Part I: Oceanographic Research Papers*, 42(5): 641–673, 1995.

J. Pedlosky. *Geophysical Fluid Dynamics*. Springer-Verlag New York, 1987.

H. E. Phillips and N. L. Bindoff. On the nonequivalent barotropic structure of the Antarctic Circumpolar Current: An observational perspective. *Journal of Geophysical Research: Oceans*, 119(8):5221–5243, 2014. ISSN 2169-9291.

H. E. Phillips and S. R. Rintoul. Eddy variability and energetics from direct current measurements in the Antarctic Circumpolar Current south of Australia. *Journal of Physical Oceanography*, 30(12):3050–3076, 2000.

A. C. Poje, T. M. Özgökmen, B. L. Lipphardt, B. K. Haus, E. H. Ryan, A. C. Haza, G. A. Jacobs, A. Reniers, M. J. Olascoaga, G. Novelli, et al. Submesoscale dispersion in the vicinity of the deepwater horizon spill. *Proceedings of the National Academy of Sciences*, 111(35): 12693–12698, 2014.

K. Polzin and R. Ferrari. Isopycnal dispersion in natre. *Journal of physical oceanography*, 34(1): 247–257, 2004.

L. F. Richardson. Atmospheric diffusion shown on a distance-neighbour graph. *Proceedings of the Royal Society of London. Series A, Containing Papers of a Mathematical and Physical Character*, 110(756):709–737, 1926.

K. Ridgway, J. Dunn, and J. Wilkin. Ocean interpolation by four-dimensional weighted least squares-application to the waters around australasia. *Journal of atmospheric and oceanic technology*, 19(9):1357–1375, 2002.

S. Rintoul and A. N. Garabato. Dynamics of the southern ocean circulation. In J. G. G. Siedler, S. Griffies and J. Church, editors, *Ocean Circulation and Climate: A 21st Century Perspective*, pages 471–492. Academic Press, 2013.

C. J. Roach, D. Balwada, and K. Speer. Horizontal mixing in the southern ocean from argo float trajectories. *Journal of Geophysical Research: Oceans*, pages n/a–n/a, 2016. ISSN 2169-9291.

C. B. Rocha, T. K. Chereskin, S. T. Gille, and D. Menemenlis. Mesoscale to submesoscale wavenumber spectra in drake passage. *Journal of Physical Oceanography*, 2015.

V. Roussenov, R. G. Williams, and J. O'Dwyer. Formation of low potential vorticity over the deep pacific. *Journal of physical oceanography*, 32(6):1811–1823, 2002.

V. Rupolo, V. Artale, B. L. Hua, and A. Provenzale. Lagrangian velocity spectra at 700 m in the western north atlantic. *Journal of Physical Oceanography*, 26(8):1591–1607, 2016/04/29 1996.

J. Sallée, K. Speer, and R. Morrow. Southern ocean fronts and their variability to climate modes. *J. Clim*, 21(12):3020–3039, 2008a.

J. Sallée, K. Speer, R. Morrow, and R. Lumpkin. An estimate of lagrangian eddy statistics and diffusion in the mixed layer of the Southern Ocean. *Journal of Marine Research*, 66(4): 441–463, 2008b.

J.-B. Sallée, K. G. Speer, and S. R. Rintoul. Mean-flow and topographic control on surface eddy-mixing in the Southern Ocean. *Journal of Marine Research*, 69(4-6):753–777, 2011.

R. Salmon. Two-layer quasi-geostrophic turbulence in a simple special case. *Geophysical & Astrophysical Fluid Dynamics*, 10(1):25–52, 1978.

S. Schmidtko, G. C. Johnson, and J. M. Lyman. Mimoc: A global monthly isopycnal upper-ocean climatology with mixed layers. *Journal of Geophysical Research: Oceans*, 118(4):1658–1672, 2013.

F. Sciremammano, R. D. Pillsbury, W. D. Nowlin, and T. Whitworth. Spatial scales of temperature and flow in drake passage. *Journal of Geophysical Research: Oceans*, 85(C7):4015–4028, 1980.

R. B. Scott and F. Wang. Direct evidence of an oceanic inverse kinetic energy cascade from satellite altimetry. *Journal of Physical Oceanography*, 35(9):1650–1666, 2005.

E. Shuckburgh, H. Jones, J. Marshall, and C. Hill. Robustness of an effective diffusivity diagnostic in oceanic flows. *Journal of Physical Oceanography*, 39(9):1993–2009, 2009.

B. M. Sloyan and S. R. Rintoul. The Southern Ocean limb of the global deep overturning circulation. *Journal of Physical Oceanography*, 31(1):143–173, 2001.

K. S. Smith and J. Marshall. Evidence for Enhanced Eddy Mixing at Middepth in the Southern Ocean. *Journal of Physical Oceanography*, 39(1):50–69, Jan. 2009.

K. S. Smith and G. K. Vallis. The scales and equilibration of midocean eddies: Freely evolving flow. *Journal of Physical Oceanography*, 31(2):554–571, 2001.

S. Sokolov and S. R. Rintoul. Circumpolar structure and distribution of the Antarctic Circumpolar Current fronts: 1. Mean circumpolar paths. *Journal of Geophysical Research: Oceans (1978–2012)*, 114(C11), 2009.

K. Speer, S. R. Rintoul, and B. Sloyan. The diabatic deacon cell. *Journal of Physical Oceanography*, 30(12):3212–3222, 2000.

K. Srinivasan and W. Young. Reynolds stress and eddy diffusivity of β-plane shear flows. *Journal of the Atmospheric Sciences*, 71(6):2169–2185, 2014.

D. Stammer. Global characteristics of ocean variability estimated from regional topex/poseidon altimeter measurements. *Journal of Physical Oceanography*, 27(8):1743–1769, 1997.

M. S. Swenson and P. P. Niiler. Statistical analysis of the surface circulation of the California Current. *Journal of Geophysical Research: Oceans*, 101(C10):22631–22645, 1996. ISSN 2156-2202.

L. Talley. Closure of the global overturning circulation through the Indian, Pacific, and Southern oceans: Schematics and transports. *Oceanography*, 26(1):80–97, 2013.

G. Taylor. Diffusion by continuous movements. *Proc. Lond. Math. Soc. Series*, 20:196–212, 1921.

L. N. Thomas, A. Tandon, and A. Mahadevan. Submesoscale processes and dynamics. *Ocean modeling in an Eddying Regime*, pages 17–38, 2008.

A. F. Thompson. The atmospheric ocean: eddies and jets in the antarctic circumpolar current. *Philosophical Transactions of the Royal Society of London A: Mathematical, Physical and Engineering Sciences*, 366(1885):4529–4541, 2008. ISSN 1364-503X.

A. F. Thompson. Jet formation and evolution in baroclinic turbulence with simple topography. *Journal of Physical Oceanography*, 40(2):257–278, 2015/07/08 2010.

A. F. Thompson and A. C. Naveira Garabato. Equilibration of the Antarctic Circumpolar Current by standing meanders. *Journal of Physical Oceanography*, 44(7):1811–1828, 2014.

A. F. Thompson and J.-B. Sallée. Jets and topography: Jet transitions and the impact on transport in the Antarctic Circumpolar Current. *Journal of Physical Oceanography*, 42(6):956–972, 2015/07/08 2012.

A. F. Thompson, P. H. Haynes, C. Wilson, and K. J. Richards. Rapid Southern Ocean front transitions in an eddy-resolving ocean GCM. *Geophysical Research Letters*, 37(23):n/a–n/a, 2010. ISSN 1944-8007. L23602.

A. F. Thompson, A. L. Stewart, and T. Bischoff. A multibasin residual-mean model for the global overturning circulation. *Journal of Physical Oceanography*, 46(9):2583–2604, 2016.

R. Tulloch and K. S. Smith. A theory for the atmospheric energy spectrum: Depth-limited temperature anomalies at the tropopause. *Proceedings of the National Academy of Sciences*, 103 (40):14690–14694, 2006.

R. Tulloch, J. Marshall, C. Hill, and K. S. Smith. Scales, growth rates, and spectral fluxes of baroclinic instability in the ocean. *Journal of Physical Oceanography*, 41(6):1057–1076, 2011.

R. Tulloch, R. Ferrari, O. Jahn, A. Klocker, J. Lacasce, J. Ledwell, J. Marshall, M. Messias, K. Speer, and A. Watson. Direct Estimate of Lateral Eddy Diffusivity Upstream of the Drake Passage. *Journal of Physical Oceanography*, 44:2593–2616, 2014.

G. K. Vallis. *Atmospheric and oceanic fluid dynamics: fundamentals and large-scale circulation*. Cambridge University Press, 2006.

D.-P. Wang, C. N. Flagg, K. Donohue, and H. T. Rossby. Wavenumber spectrum in the gulf stream from shipboard adcp observations and comparison with altimetry measurements. *Journal of Physical Oceanography*, 40(4):840–844, 2016/04/26 2009.

B. A. Warren. Suppression of deep oxygen concentrations by Drake Passage. *Deep Sea Research Part A. Oceanographic Research Papers*, 37(12):1899 – 1907, 1990. ISSN 0198-0149.

Y. Xu and L.-L. Fu. The effects of altimeter instrument noise on the estimation of the wavenumber spectrum of sea surface height. *Journal of Physical Oceanography*, 42(12):2229–2233, 2012.

J. D. Zika, B. M. Sloyan, and T. J. McDougall. Diagnosing the southern ocean overturning from tracer fields. *Journal of Physical Oceanography*, 39(11):2926–2940, 2009.

BIOGRAPHICAL SKETCH

The author was born on 4 January, 1989 in Rajasthan, India. He spent most of his young life in New Delhi, and moved to Goa in 2006 to obtain a B.E. in Chemical Engineering from Birla Institute of Technology and Science in 2010. It was during this time that he did a research project studying ocean models at Center for Mathematical Modeling and Computer Simulations, Bangalore, and developed a keen interest in the study of fluid flows in the natural world. He began his graduate work in Physical Oceanography with Dr. Kevin Speer at Florida State University in 2010, and finished in November 2016 with a M.S. in Applied and Computational Mathematics and a Ph.D. in Geophysical Fluid Dynamics.